Spherical Nanoindentation Stress-Strain Curves

Siddhartha Pathak [1], *Surya R. Kalidindi* [2*]

[1] Center for Integrated Nanotechnologies, Los Alamos National Laboratory, Los Alamos, NM, 87545, USA

[2] George W. Woodruff School of Mechanical Engineering, Georgia Institute of Technology, Atlanta, Georgia, GA, USA

Abstract

Although indentation experiments have long been used to measure the hardness and Young's modulus, the utility of this technique in analyzing the complete elastic-plastic response of materials under contact loading has only been realized in the past few years – mostly due to recent advances in testing equipment and analysis protocols. This paper provides a timely review of the recent progress made in this respect in extracting meaningful indentation stress-strain curves from the raw datasets measured in instrumented spherical nanoindentation experiments. These indentation stress-strain curves have produced highly reliable estimates of the indentation modulus and the indentation yield strength in the sample, as well as certain aspects of their post-yield

[*]Contact author: - George W. Woodruff School of Mechanical Engineering, Georgia Institute of Technology, Atlanta, Georgia, GA, USA, Tel: 404.385.2886

E-mail: surya.kalidindi@me.gatech.edu, Website: http://mined.gatech.edu/

behavior, and have been critically validated through numerical simulations using finite element models as well as direct *in-situ* scanning electron microscopy (SEM) measurements on micro-pillars. Much of this recent progress was made possible through the introduction of a new measure of indentation strain and the development of new protocols to locate the effective zero-point of initial contact between the indenter and the sample in the measured datasets. This has led to an important key advance in this field where it is now possible to reliably identify and analyze the initial loading segment in the indentation experiments.

Major advances have also been made in correlating the local mechanical response measured in nanoindentation with the local measurements of structure at the indentation site using complementary techniques. For example, it has been shown that the combined use of orientation imaging microscopy (OIM) and nanoindentation on polycrystalline metallic samples can yield important information on the orientation dependence of indentation yield stress, which can in turn be used to estimate percentage increase in the local slip resistance in deformed samples. The same methods have been used successfully to probe the intrinsic role of grain boundaries in the overall mechanical deformation of the sample. More recently, these protocols have been extended to characterize local mechanical property changes in the damaged layers in ion-irradiated metals. Similarly, the combined use of Raman spectroscopy and nanoindentation on samples of mouse bone has revealed tissue-level correlations between the mineral content at the indentation site and the associated local mechanical properties. The new protocols have also provided several new insights into the buckling response in dense carbon nanotube (CNT) brushes. These and other recent successful applications of nanoindentation are expected to provide

the critically needed information for the maturation of physics-based multiscale models for the mechanical behavior of most advanced materials. In this paper, we review these latest developments and identify the future challenges that lie ahead.

Keywords

Nanoindentation; Orientation Imaging Microscopy (OIM); Polycrystalline metals; Slip resistance; Grain boundaries; Pop-ins; Raman Spectroscopy

Table of Contents

1. Introduction

For more than a century, the indentation test has been one of the most commonly employed techniques for characterization of the mechanical properties of a vast range of materials [1, 2]. In a typical test, a hard indenter of known geometry is driven into a softer sample by applying a preset load or displacement. The dimensions of the resultant imprint are then measured and correlated to a hardness index number. With the advent of higher resolution testing equipment, it has now become possible to continuously control and monitor the loads and displacements of the indenter as it is driven into and withdrawn from a sample material. Known as nanoindentation (or instrumented indentation testing, or depth sensing indentation), this significantly expands the capabilities of the traditional hardness testing method [3, 4]. Instrumented indentation has significant advantages over conventional indentation testing, since it can potentially produce very reliable measurements of stress-strain curves from fairly small indentation depths (of the order of a few nanometers).

The popularity of indentation tests stems in part from its versatility, ease of use (see Fig. 1), and its potential for high throughput. This is in contrast to most of the other currently used methods for interrogating the local mechanical properties at micron and sub-micron length scales that rely largely on testing miniaturized samples in nominally homogeneous deformation/stress modes [5]. For example the compression testing of micro-pillars produced by removing material around a selected region of interest using a focused-ion beam (FIB) has attracted the recent attention of many researchers [6]. However these techniques typically require tremendous resources in terms of sample preparation, test conditions and operator time, which make their large scale use

uneconomical. On the other hand nanoindentation, when aided with proper analysis methods, is capable of producing the desired information at significantly lower effort and cost. Moreover, reliable and quantitative measurement of mechanical degradation of surface layers (e.g., ion-irradiated materials in nuclear applications) is currently only possible with indentation techniques. This high throughput methodology when used in conjunction with structure information measured locally at the indentation site has the potential to become a key tool in efforts aimed at the maturation of physics-based multiscale materials models.

A common limitation in a majority of the indentation analysis methods used today is that the estimation of material properties, such as Young's modulus and hardness, are typically made from the measured unloading segments of load-displacement curves (after some amount of elastic-plastic loading) under the assumption that the unloading segments are predominantly elastic [7, 8]. In this approach, the plastic deformation induced during the loading segment is likely to influence strongly the values of the mechanical properties (e.g., hardness) extracted from these experiments. This problem has been recognized since the early 1890s and numerous attempts have been made to measure the 'absolute hardness' of a material [9]. However, quantitative estimates of absolute hardness, generally defined as "resistance to permanent deformation" [10] or "the intensity of the maximum pressure which just produces yielding" in indentation [11], have not been feasible before the advent of modern instrumented test methods.

In this review, we focus on a fundamentally different approach to this problem that has enjoyed tremendous success in recent years. This new approach relies heavily on new data analyses procedures for spherical nanoindentation that transform the entire

load-displacement dataset, including both the loading and the unloading segments, into much more meaningful indentation stress-strain curves [12, 13]. The use of these indentation stress-strain curves makes it possible to analyze the initial loading segments of spherical indentation, thereby allowing reliable measures of indentation modulus and indentation yield strength of the material prior to the changes induced by the indentation itself. The ability to produce indentation stress-strain curves has generally been more successful with spherical indenters [14-16], where their relatively smoother stress fields and larger initial elastic segments (compared to sharper indenters) allow one to follow the evolution of the mechanical response in the material, from initial elasticity to the initiation of plasticity to post-yield behavior at finite plastic strains.

This review summarizes the main developments and advances in recent years in the protocols used to generate spherical indentation stress-strain curves. We begin with a description of the recently developed methodology used for extracting indentation stress-strain curves from the corresponding indentation load-displacement data, which include a novel approach for determining the 'zero-point' in spherical nanoindentation experiments and a new definition of indentation strain. These concepts are then critically validated through numerical simulations using finite element models as well as direct *in-situ* scanning electron microscopy (SEM) measurements on micro-pillars. Next, we describe a series of applications covering a wide variety of material systems including metallic materials, thin films of dense carbon nanotube (CNT) brushes, and complex hierarchical biological materials (e.g., bone). These applications illustrate the versatility and utility of the indentation stress-strain curves in extracting mechanical information at the micron to sub-micron level. Another salient feature of the case studies described here is that the

mechanical information obtained from these tests are correlated to the corresponding local structure information (obtained using complementary characterization techniques such as orientation imaging microscopy (OIM), which images the microstructure using electron backscattered diffraction (EBSD) for crystalline samples, and Raman spectroscopy, which is highly sensitive to both mineral and collagen components of biological tissues such as bone) at similar length scales in the samples.

2. Classical Indentation Theories and Analyses Methods

The most widely used indentation theories are all based on Hertz's model [17] for frictionless contact between two isotropic elastic solids. For spherical indentation, this is usually expressed as

$$P = \frac{4}{3} E_{eff} R_{eff}^{1/2} h_e^{3/2}, \qquad a = \sqrt{R_{eff} h_e} \tag{1}$$

where a is the radius of the contact boundary at the indentation load P, and h_e is the elastic indentation depth (see Fig. 2a for definitions of various variables used in Eq. (1)). R_{eff} and E_{eff} denote the effective radius and the effective modulus of the indenter and the specimen system, respectively:

$$\frac{1}{E_{eff}} = \frac{1-\nu_s^2}{E_s} + \frac{1-\nu_i^2}{E_i}, \quad \frac{1}{R_{eff}} = \frac{1}{R_i} + \frac{1}{R_s}. \tag{2}$$

Here, ν and E denote the Poisson's ratio and the Young's modulus, while subscripts s and i refer to the specimen and the indenter, respectively. For consistency, we will always refer to E_s as the Young's modulus of the sample material. E_{eff} will be referred as the effective indentation modulus and the term $\frac{E_s}{1-\nu_s^2}$ will be referred to as the indentation

sample modulus or simply the indentation modulus. For the case of a rigid indenter, the effective indentation modulus and the indentation modulus are the same. Also, for elastic loading of a flat sample, R_s approaches infinity, and therefore, $R_{eff} = R_i$.

In practice, the initial elastic loading segments in experimentally measured spherical nanoindentation datasets are very short (typically only a few tens of nanometers of indentation depth). Moreover, the many uncertainties associated with identifying the start and the end of the purely elastic segments in these measurements pose major hurdles in successfully analyzing these segments in the nanoindentation measurements. Consequently, much of the effort in the literature has focused on applying the Hertz's theory (Eqs. (1) and (2)) to the unloading segment (generally presumed to be purely elastic) in the measured load-displacement data. Although the unloading segment is likely to be purely elastic in many materials (confirmed by finite element models [18]), the main complication in the analyses of the unloading segment stems from lack of knowledge of the residual geometry of the sample surface upon complete unloading since it would have been altered substantially by the inelastic deformation imposed during the loading segment (see Fig. 2b). For the case of sharp indenters, successful analysis of the unloading segment using Hertz's theory has required the use of calibrated area functions and effective indenter shapes [7, 8] to take into account the complex changes in the sample surface geometry caused by the inelastic strains induced during the loading segment.

The analysis of the unloading segment in spherical indentation using Hertz's model leads to the following equations [7, 19]:

$$E_{eff} = \frac{\sqrt{\pi}}{2}\frac{S}{\sqrt{A_c}} = \frac{S}{2a}, \quad A_c = \pi a^2 \tag{3}$$

The value of the contact radius is then generally estimated using the geometry of the spherical indenter as

$$a = \sqrt{2h_c R_i - h_c^{\,2}}, \quad h_c = h_t - \frac{3}{4}\frac{P}{S} \tag{4}$$

where S is the slope of the unloading curve (see Fig. 2b) at the peak indentation load (P), A_c is the projected contact area, h_c is the distance from the circle of contact to the maximum penetration depth, and h_t is the total penetration depth at peak load. Note that the two definitions of the contact radius in Eqs. (1) and (4) may not provide consistent results. We shall revisit this in much more detail later.

Eqs. (2) – (4) have been used extensively to estimate the Young's moduli of the indented material [3, 7, 8, 20, 21]. However indentation, because of its non-destructive nature, is more popular due to its ability to estimate the plastic properties (such as hardness) of the sample. Brinell [22-24] and Vickers [25] tests introduced the basic concepts of hardness measurements using spherical and sharp indenters, respectively. A number of hardness measures were introduced along with these tests that define hardness as the load divided either by the surface area or the projected area of the residual indentation. These hardness measures were found to be extremely valuable in quickly assessing the resistance to plastic deformation in a range of materials, and fine-tuning their thermo-mechanical processing histories to improve their mechanical performance. Furthermore, some of the hardness measures showed a strong correlation to properties measured in standard tension tests such as the ultimate tensile strength. In spite of these advantages, hardness measurements continue to be used mainly as comparative measures

because the hardness numbers themselves are quite sensitive to indenter shape, indenter size, and the imposed load level.

As a natural extension of the hardness measurements, Tabor [1] introduced the concept of indentation stress-strain curves. The indentation stress was defined as the mean contact pressure (load divided by projected area of residual indentation; also called Meyer's hardness [26]). The indentation strain was invoked to be $0.2a/R_i$. It is important to note that in Tabor's approach the contact radius was measured directly from the residual indentation in the sample. Therefore, one indentation would produce only one data point on the indentation stress-strain curve. Consequently, a substantial effort is required for extracting a complete indentation stress-strain curve using Tabor's original approach. Tabor [27] demonstrated an excellent correspondence between indentation stress-strain curves (by accumulating data obtained using different indenter radii) and those obtained from standard simple tension tests on mild steel and annealed copper (see Fig 3a).

There have been several efforts in the literature to automate the extraction of multiple data points on the indentation stress-strain curve from a single indentation experiment [15, 28, 29]. Field and Swain [15, 29, 30] developed novel protocols that utilized multiple partial unloads and estimated the contact radius directly from the measurements of the load and the displacement in each such partial unload (Fig 3b). In their approach, each partial unload is assumed to be purely elastic and is analyzed using Hertz's theory to estimate the contact radius (instead of direct measurement from the residual indentation as performed by Tabor). It should be noted that the estimate of the contact radius based on Hertz's theory corresponds to the value of the contact radius in

the loaded geometry, whereas the direct measurement performed by Tabor [1] corresponds to the contact radius estimated from the unloaded geometry. Consequently, there might be a substantial difference in the values of the contact radius obtained using these two approaches. The approach proposed by Field and Swain [15, 29] is attractive because it can be automated with modern instrumentation. Furthermore, extensions have been proposed in the literature [29] to these protocols to account for the changes in contact geometry that occur due to the pile-ups and sink-ins associated in the indentation measurements.

A characteristic feature in the simulated indentation stress-strain curves reported in the literature (obtained using the methods described above) is the relatively large elastic-plastic transition in these curves [15, 31, 32]. More specifically, the elastic-plastic transition is generally observed to occur over the range of values of indentation stress corresponding to $1.1\sigma_y$ and $3\sigma_y$, where σ_y is the uniaxial plastic yield strength for the sample material. This large elastic-plastic transition misrepresents a fairly large section of the indentation stress-strain curve as exhibiting high levels of strain hardening (i.e. apparent strain hardening), and makes it very difficult to establish direct connections between the indentation stress-strain curves and those obtained from standard tension or compression curves. Possibly, this large elastic-plastic segment in the indentation stress-strain curves is directly attributable to the specific protocols used for the estimation of the contact radius. We will present in subsequent sections our recently developed data analyses protocols for estimation of the contact radius that significantly shrink this undesired transition segment in the indentation stress-strain curves (cf. Fig. 4).

3. Indentation Stress and Strain Measures

Hertz's theory (Eq. (1)) can be recast into a linear relationship between indentation stress and indentation strain defined as [15, 29]

$$\sigma_{ind} = \frac{4E^*}{3\pi}\varepsilon_{ind}, \qquad \sigma_{ind} = \frac{P}{\pi a^2}, \qquad \varepsilon_{ind} = \frac{a}{R_{eff}} \tag{5}$$

Note that the definition of the indentation stress shown is essentially based on the concept of Meyers hardness described earlier. The definition of the elastic indentation strain in Eq. (5) may differ from some of the definitions in the current literature by just a constant that can be easily reconciled by re-arranging the coefficients in the equation. The main limitation of the indentation strain measure shown in Eq. (5) is that it does not lend itself to rational extension to the case of elastic-plastic indentation. This is because the ratio a/R_{eff} lacks reasonable physical interpretation as a strain measure. Strain should be fundamentally defined as the ratio of change in length over the initial length on a selected line segment in a region of interest in the sample. a/R_{eff} cannot be interpreted as a strain in any idealization of the sample being indented. Furthermore, R_{eff} does not even reflect a relevant length scale in characterizing the deformation experienced by the sample (in fact, the contact radius, a, is a better descriptor of the length scale of the indented region; see Fig. 2).

The most common choice of indentation strain measure for elastic-plastic indentations in the current literature is a/R_i. A number of recent studies have utilized this measure of indentation strain to derive some physical insights into the material response [33-38]. Although this definition enjoys some similitude with the definition

shown in Eq. (5) for the initial elastic loading of a flat sample (where $R_{eff} = R_i$), there is really no rational justification for its selection for the subsequent elastic-plastic indentation regime.

The authors of this review have recently proposed that the Hertz's theory for elastic indentation be recast as [12]

$$\sigma_{ind} = E^* \varepsilon_{ind}, \qquad \sigma_{ind} = \frac{P}{\pi a^2}, \qquad \varepsilon_{ind} = \frac{4}{3\pi}\frac{h_e}{a} \approx \frac{h_e}{2.4a} \tag{6}$$

The definition of elastic indentation strain in Eq. (6) can be visualized by idealizing the primary zone of indentation deformation as being equivalent (in an average sense) to compressing by h_e (the elastic indentation depth) a cylindrical region of radius a and height $2.4a$ (see Fig. 2). The cylinder might expand laterally to accommodate this contraction in height. The lateral expansion is, however, not relevant to the definition of the indentation strain. Note that this interpretation allows the visualization of strain in the classical sense as the change in length per unit length. Furthermore, it is easily extendable to elastic-plastic indentations by simply replacing h_e with h_t (the total indentation depth).

This interpretation is much more physical than the definition of indentation strain as a/R_{eff} or a/R_i. The main reason for using a/R_{eff} is its convenient appearance in Eq. (5). In the limit of small spherical indentation depths that are typical of a purely elastic indentation (where $h_t = h_e$) of the sample, it can be seen that $\frac{h_t}{a} \approx \frac{a}{R_{eff}}$. This implies that the definition of the indentation strain adopted here is equivalent to the definition used in the literature for the initial elastic loading segment, except for a multiplicative factor. The inclusion of this factor in the definition of the indentation strain conveniently modifies the slope of the elastic indentation stress-strain curve to be equal to the effective

indentation modulus, E_{eff}. In other words, Eqs. (5) and (6) are mathematically equivalent to each other for purely elastic indentation, except that the terms are grouped differently. However, as discussed later, when applied to data sets collected from samples exhibiting both elastic and inelastic deformations, the two approaches result in very different indentation stress-strain curves.

Another source of considerable confusion in the literature stems from the two definitions of contact radius shown in Eq. (1) and Eq. (4). In the case of a fully elastic spherical indentation on a flat surface, it can be shown (both experimentally and theoretically) that the two definitions in Eq. (1) and Eq. (4) provide equivalent values for the contact radius, a. However, in our experimental investigations, we found that the values estimated by these two definitions deviate from each other significantly as the sample experiences a substantial amount of inelastic strain and the contact radius becomes larger. We critically explore the underlying cause of the disagreement using finite element models in the next section.

4. Finite Element Models for Computing Indentation Stress-Strain Curves

Because of the complex and the highly heterogeneous stress and strain fields experienced in elastic-plastic indentation, finite element models are extremely valuable in critically evaluating several of the concepts presented in the preceding sections and to extract meaningful properties from the measured raw data. A majority of the approaches used in the current literature address the extraction of properties from indentation measurements as an inverse problem; the solutions strategies generally demand the use of

sophisticated optimization algorithms to minimize the discrepancy between the measured load-displacement data and the corresponding predictions from the finite element simulations [39-43]. However, the fact that the elastic-plastic transition occurs over a very short regime in the overall load-displacement curve makes it very difficult to directly extract the measures associated with initial plasticity (e.g., yield strength, initial strain hardening rate) using this approach. In fact, in most measured indentation load-displacement datasets, it is very difficult to distinguish the elastic regime from the elastic-plastic regime because of the very smooth transition between these regimes. Consequently, there is tremendous benefit to first recovering the indentation stress-strain curves from the measured indentation load-displacement datasets. In addition to clearly resolving the elastic-plastic transition, the indentation stress-strain curves often provide very useful insights into the material response and provide an opportunity to compare material behavior between different samples even without recovering mechanical properties.

In a recent paper, Donahue et al. [44] utilized a finite element model to gain new insights into three main issues central to recovering reliable indentation stress-strain curves from spherical nanoindentation measurements: (i) What is the accuracy of the different methods used in the current literature for estimating the contact radius, a? (ii) Which definition of indentation strain produces more meaningful indentation stress-strain curves? (iii) How does one reconcile the differences between the indentation stress-strain curves and the conventional uniaxial stress-strain curves from simple tension or simple compression on bulk samples? The use of finite element models for resolving these issues circumvents many of the difficulties and uncertainties faced in experimental

investigations (e.g., identification of the point of initial contact, precise geometry of the indenter, assumed isotropy of material response, assumed non-hardening behavior of sample in plastic deformation, friction between indenter and sample surfaces), and offers unique opportunities for critical validation of the main concepts.

More specifically, Donohue et al. [44] assessed critically the precise effect of the different definitions of the contact radius and the different definitions of indentation strain on the resulting indentation stress-strain curves for an elastic-perfectly plastic material response. The table in Fig. 4a lists the four possible ways of generating an indentation stress-strain curve, labeled A through D, from the same simulation dataset. Fig. 4b presents the different indentation stress-strain curves generated using the four different protocols listed in the table in Fig. 4a. It is seen that the initial elastic portions from all four curves (labeled A through D) matched quite well with each other. The curves started to deviate from each other after the initial elastic segments. These authors report that the deviations in the indentation stress-strain curves commenced at about an indentation stress of about $1.2\sigma_y$ and correlated with substantial changes in R_{eff}. It was also noted that only the unloading segment corresponding to curve A showed the expected indentation modulus that matched very well with the indentation modulus from the loading segment.

Indentation stress-strain curves labeled B and C (based on the contact radius definition in Eq. (4)) in Fig. 4a are observed to exhibit a significant post-yield hardening behavior for both materials. In fact these curves indicate that indentation flow stress reaches about $3\sigma_y$ in both materials, consistent with several reports in the literature that use the definition of the contact radius in Eq. (4) [14, 15, 29, 38, 45, 46]. Note that the

plastic response of both these materials was defined to be non-hardening (i.e. elastic-perfectly plastic with constant yield strength) in the prescription of the material constitutive behavior. Furthermore, the indentation stress-strain curves labeled A and D (based on contact radius definition used in Hertz's' theory; Eq. (1)) exhibited very little hardening by comparison. These observations suggest that the apparent hardening reported extensively in indentation stress-strain curves in the literature is directly attributable to the definition of the contact radius used in these computations. More importantly, it is seen that the use of the contact radius definition that is consistent with Hertz's' theory provides the best representation of the post-yield behavior in the indentation stress-strain curves.

Donohue et al. [44] also report that the values of the indentation stress and indentation strain computed by protocol A provide the best match with the average stress and strain values in the indentation zone predicted by the finite element model. The predicted indentation strain fields in the finite element model at a depth close to indentation yield are shown in Fig. 5. It is clearly seen that the indentation zone extends approximately to a length of about 2.4a, justifying the new definition of the indentation strain presented in Eq. (6) (see also Fig. 2a). The authors also report strong correlations between the uniaxial mechanical properties and those extracted from the indentation stress-strain curves obtained using protocol A.

There have also been attempts to extract microscale mechanical properties through inverse solution methodologies that match FE predictions of indentations with the corresponding measurements. Zambaldi et al. have extracted values of the critical resolved shear stresses (CRSS) from spherical nanoindentation measurements conducted

on differently oriented grains of alpha-titanium [47]. In their approach, they focused their efforts on matching the FE predictions and the measurements in various aspects of the surface topology at the indentation site (after the indentation was completed). It is not yet clear if a different choice of the parameters selected to quantify the surface topology would significantly affect the extracted values. In a different approach, Patel et al. have recently demonstrated the viability of extracting single crystal elastic stiffness parameters from polycrystalline samples using spherical nanoindentation and orientation measurements combined with finite element simulations [48]. This new approach utilizes compact spectral representations to capture the dependence of the indentation modulus on the crystal lattice orientation at the indentation site as well as the single crystal elastic constants (defined in the crystal reference frame). Once such a function is established (from running a large array of FE simulations) the unknown single crystal elastic constants for a selected phase in a given sample are estimated through a regression technique that provides the best match between spherical nanoindentation measurements obtained on differently oriented grains of that phase in a polycrystalline sample and the function already established in the first step. The accuracy and viability of this approach were demonstrated for polycrystalline Fe-3%Si.

5. Indentation Stress-Strain curves – Experimental Analysis Techniques

5.1 Indentation Stress-Strain Curves using Continuous Stiffness Measurement (CSM) data

Similar to the results of the finite element model described earlier, indentation stress-strain curves extracted from experimental measurements also show significant sensitivity to the specific data analyses protocols used. Fig. 6 highlights some of the main differences between indentation stress-strain curves plotted using two different sets of protocols: (i) default zero-point identified by the machine (MTS XP®) and definitions used in protocol C (see table in Fig. 4a), and (ii) novel protocols for identification of zero-point (discussed later) with definitions used in protocol A (see table in Fig. 4a). Experimentally extracted indentation stress-strain curves using a 13.5 μm radius spherical indenter on individual grains of polycrystalline samples of tungsten and aluminum are shown in this figure. These two metallic samples were chosen due to their low elastic anisotropy (note that Hertz's theory is valid only for isotropic elastic materials) as well as the large variation in their respective mechanical properties (aluminum exhibits a low Young's modulus and a low yield strength while tungsten exhibits a high Young's modulus and a high yield strength).

Two major problems are easily apparent when indentation stress-strain curves are plotted using the protocols used in the current literature, i.e. when using protocol C. First, there is a substantial amount of noise, especially in the initial elastic and yield sections of this curve, and second, indentation strain defined as $a/2.4R_i$ does a very poor job of

capturing the elastic unloading curves. For example, in case of aluminum, the slope of the unloading stress-strain curve, and hence the unloading indentation modulus, calculated using $a/2.4R_i$ as the indentation strain is actually negative (Fig. 6b). This problem of highly unrealistic unloading slopes in the analyses of spherical indentation data has been noted in numerous other materials, including tungsten, aluminum, silver, gold, steel etc. [12]. In the opinion of the authors, these problems have contributed to the large variance in the reported spherical indentation stress-strain curves and in the values of the properties measured therein. It is also noted that the indentation stress-strain curves for both tungsten and aluminum are much more meaningful when plotted using the novel protocols described in this paper in at least the following two aspects: (i) the unloading segments show the same slopes as the loading segments, and (ii) the indentation stress-strain curve for tungsten exhibits much more strain hardening compared to aluminum.

The substantial scatter in the initial loading portion of the indentation stress-strain curve obtained from the conventional approach stems from an incorrect determination of the zero-point or the point of effective initial contact during nanoindentation, while the unphysical values of the indentation moduli in the unloading segments in this approach arise from the incorrect use of a/R_i as an effective measure of indentation strain.

The problem of identifying a zero-point in nanoindentation analysis has been discussed in detail in several papers [49] and various methods have already been explored in the literature. In one approach [50], the displacement sensor is set to zero upon reaching a pre-set contact force. The data in the initial segment is then curve-fitted and extrapolated back to zero force. This method, commonly used in other mechanical testing techniques as well, requires a prior knowledge of the sample properties in order to choose

an appropriate initial force and often results in an underestimation of the contact area and a corresponding overestimation of the hardness and indentation modulus values [51].

The standard protocol for the MTS machine in the non-CSM mode uses the slope of the load-displacement data for surface detection. In the CSM mode, a small, sinusoidally varying signal is imposed on top of the DC signal that drives the motion of the indenter. This allows constant monitoring of various signals such as the harmonic contact stiffness, the harmonic load, the harmonic displacement and the phase angle, all of which could potentially be used for surface detection. The quantity that shows an immediate and significant change upon initial contact is then generally chosen as the criteria for surface detection. The use of the stiffness signal has been most widely advocated in the literature [8, 50, 51] for this purpose. The accuracy for this method has been reported to be anywhere from ±2 nm [8] to ±30 nm [51]. Innovative techniques, such as the use of a video camera for indentation of optically clear materials [52] and photoluminescense of quantum dots due to indentation [53], have also been explored to solve the problem of determining surface contact.

Other than the advancements in instrumentation described above, there has also been multiple efforts on post-processing of the data for zero-point determination. One common approach has been to fit the initial (elastic) response of the indentation data to Hertz theory and back-extrapolate to zero-depth. For example Chudoba et al. [54-57] have proposed fitting the first few nanometers of indentation data to a power-law equation conforming to Hertzian contact: $P = C \cdot (h\text{-}h_0)^{1.5}$, where h_0 is the displacement correction and C is a constant. A similar approach has been used by Ullner [58]and Grau et al. [59] where the fit is to a second-order polynomial. More recently, Kalidindi and

Pathak [12] and Moseson et al. [60] proposed new protocols for establishing the effective zero-point that utilizes the CSM signal (stiffness) in addition to the load and displacement signals. While the use of all three measurement signals (load, displacement, and the stiffness, see Eq. 7 below) has a distinct advantage compared to the previous efforts for extracting the zero-point, the details of the methods proposed by these two groups are substantially different from each other. The approach proposed by Moseson et al. [60] is based on Eq. (4) that includes the geometric relationship between contact radius and the indenter radius, whereas the approach proposed by Kalidindi and Pathak [12] is based on Eq. (1). As discussed earlier, the values of contact radii computed from Eqs. (1) and (4) are substantially different from each other (Fig 4), especially after the sample experiences a significant change in the value R_{eff} (after a certain amount plastic strain has been induced in the sample, shown later in Fig 9b). Also, it was pointed out earlier that only Eq. (1) is consistent with Hertz's theory. The procedure outlined in [12] has been very successful in extracting indentation stress-strain curves, as detailed below.

The new data analyses procedures proposed by Kalidindi and Pathak [12] can be summarized as a two-step process. The first step in this process is an accurate estimation of the point of effective initial contact in the given data set, i.e. a clear identification of a zero-point that makes the measurements in the initial elastic loading segment consistent with the predictions of Hertz's theory [17, 61]. For spherical nanoindentation this relationship can be expressed as

$$S = \frac{3P}{2h_e} = \frac{3\left(\widetilde{P} - P^*\right)}{2\left(\widetilde{h}_e - h^*\right)}, \tag{7}$$

where $\widetilde{P}$, $\widetilde{h}_e$, and S are the measured load signal, the measured displacement signal, and the continuous stiffness measurement (CSM) signal in the initial elastic loading segment

from the machine, respectively, and P^* and h^* denote the values of the load and displacement signals at the point of effective initial contact. A linear regression analysis can then be used to establish the point of effective initial contact (P^* and h^*) in the indentation experiment. Note that these protocols do not require an estimation of the contact radius a or the effective radius R_{eff}.

Utilization of Eq. (7) is made possible by the use of the CSM signal (in the MTS XP® nanoindentation machine and their later generations) which is measured concurrently with the load-displacement values. CSM allows the measurement of the contact stiffness ($S = dP/dh_e$) at every point along the loading curve (and not just at the point of unloading as in the conventional approach). Thus in essence the CSM allows the continuous measurement of S in one single indentation experiment without the need for discrete unloading cycles [62]. A separate procedure for measuring the effective zero point without the use of the CSM signal is described in Section 5.2.

The procedure described above is illustrated in Fig. 7a for a sample of Fe-3%Si steel for a 13.5 μm radius spherical indenter. In this figure, the portion of the initial loading data segment found to be in excellent agreement with Eq. (7) is marked (in blue). The segment before this is probably influenced by various surface artifacts (such as surface roughness, non-ideal indenter shape etc.), while the segment following this segment (not shown in the figure) deviates substantially from the linear relationship shown in the figure, as it is likely influenced by inelastic deformation in the sample. The excellent agreement of this data segment to Hertz's theory is also utilized later in order to calculate the indentation modulus of the sample during loading (using Eq. (1)).

Figure 7b shows the point of initial contact as identified by the default procedure in the MTS software (C_1) and by the procedure described above (C_2). In the default procedure, C_1 is generally determined as the point at which the *S* signal first reaches or exceeds 200 N/m. Note that the value for *S* is generally negative before the indenter is in contact with the specimen. For hard materials such as metals and ceramics, this option almost always underestimates the zero-point. Thus, to arrive at C_2, the load signal in Fig. 7b needed to be moved by about $P^* = 0.12$ mN and the displacement signal by about $h^* = 6.8$ nm with respect to C_1.

A major advantage of Eq. (7) is that this approach identifies an "effective" or virtual point of initial contact, and not necessarily the actual point of initial contact. The concept of an effective point of initial contact allows us to de-emphasize any artifacts created at the actual initial contact due to the unavoidable surface conditions (e.g. surface roughness, presence of an oxide layer etc.) and imperfections in indenter shape. For example, the above procedure was found to work even in the case of mechanically polished bone samples (final polishing step 0.05 μm diamond paste) where larger corrections for the displacement signal were needed (h^* = 10-15 nm [63]) than the corresponding ones in well-prepared (i.e. electro-polished where $h^* \sim 5$ nm) metal samples [12, 64-66]. As mentioned above, the effective point of initial contact is not likely to be the point of the actual initial contact. However, the elastic segment of the initial loading beyond h^* is in excellent agreement with Hertz's theory suggesting that beyond this point, the factors cited above do not appear to have a significant impact on the measurements.

Figure 7c shows the indentation stress-strain curve derived from the load-displacement data in Fig. 7b using the protocol outlined above and compares it to the plot using the machine generated zero point (C_1). Both the initial elastic and yield sections are much better resolved when the zero point is determined using the procedure described above (instead of using the default procedure in the MTS software).

The estimation of the contact radius (a) is the second step in the extraction of indentation stress-strain curves. With the CSM option, the problem is significantly simplified because of Eq. (3) ($a = S/2E_{eff}$). Once the value of E_{eff} is established from the initial loading curve [12] (or if the Young's modulus of the sample material is already known), the contact radius can be easily computed from Eq. (3) assuming that E_{eff} remains constant during the inelastic deformation caused by the indentation. This assumption is quite reasonable for isotropic metals such as tungsten and aluminum. Although plastic deformation in metals does not itself cause any direct change in the elastic properties, it rotates crystal lattices into new orientations [67], and thereby modifies the texture in the sample. Such changes in the underlying texture caused by plastic deformation usually produce a substantial change in the effective elastic properties of the solid [68-70]. The influence of crystal orientation on the indentation modulus is addressed in detail in Section 6.1. However, in metals such as tungsten and aluminum shown in Fig. 6, the elastic anisotropy at the single crystal level is quite small (in fact tungsten crystals exhibit isotropic elastic response), and therefore it is reasonable to assume that E_{eff} remains constant during the inelastic deformation caused by the indentation. Using Eqs. (3) and (6) the complete indentation stress-strain curves can be computed as shown in Figs. 6 and 7.

After the completion of the two-step process described above, indentation stress-strain curves can be computed using the definitions used in Eq. (6) and protocol A (table in Fig. 4a). An important point to note is that the nanoindentation data analysis approach described in these equations is based on Hertz's theory, which assumes isotropic elastic behavior of the sample. Indeed almost all (macro, micro and nano) indentation studies reported in the literature employ the Hertz's theory, even when it is quite clear that the sample material exhibits significant anisotropy in the indentation zone. For example, in most nanoindentation studies of metals and ceramics, the indentation zones are much smaller than the individual grains in the samples, and therefore the sample is expected to exhibit significant anisotropy in the indentation zone. Surprisingly, a vast majority of such indentation measurements continue to exhibit a linear relationship between P and $h^{3/2}$, as predicted by Hertz's theory. Consequently, the Young's modulus estimated using Hertz's theory on anisotropic solids is often interpreted as the equivalent isotropic value in the literature, without explicitly stating this assumption [7, 13, 14, 50, 65, 71, 72].

The main concepts presented so far can be summarized as follows:

1. The new procedures for establishing the effective point of initial contact based on Eq. (7) produces indentation stress-strain curves that exhibit meaningful initial elastic loading segments. This new procedure utilizes the CSM signal provided by modern nanoindentation machines. More specifically, the indentation stress-strain curves generated by this new method do not exhibit the substantial noise and spikes prevalent in the initial loading segments of the indentation stress-strain curves obtained using the zero-point given by the default procedures currently used in the equipment manufacturer's software.

2. A new rational definition of the indentation strain has been formulated (see Eq. (6)). This new definition is highly consistent with Hertz's theory for purely elastic contact. For elastic-plastic contact, it was also found to produce better indentation stress-strain curves that exhibit a clearly identifiable elastic segment, a smooth but relatively short transition to the plastic deformation regime, and an unloading segment where the unloading indentation modulus matched well with the indentation modulus from the loading segment.

5.2 Indentation Stress-Strain Curves without CSM

Both the estimation of the zero-point (Eq. (7)) and the estimation of the contact radius (Eq. (3)) described in Section 5.1 require the use of the continuous stiffness measurement signal (CSM). However the CSM module is an optional accessory on the MTS/Agilent nanoindenter machine, and hence is available only on some machines. Moreover, other nanoindentation machines (manufactured by companies other than MTS/Agilent) may not even offer CSM as an option. In this section, an alternate approach is presented for converting the spherical nanoindentation load-displacement data into indentation stress-strain curves, without the need for CSM.

Extraction of the indentation stress-strain curves without using CSM is described in detail in Ref. [13] and is achieved in a two-step process: (i) establishing the effective zero-point and (ii) estimating the contact radius, a. In [13], the authors have established the zero-load and the zero-displacement point by fitting the recorded initial elastic load ($\widetilde{P}$) and displacement ($\widetilde{h}_e$) signals to the predictions of Hertz's theory. Thus rearranging Eq. (1), the load and displacement during elastic loading in a spherical nanoindentation experiment should be related by

$$\tilde{h}_e - h^* = k\left(\tilde{P} - P^*\right)^{2/3} \qquad k = \left[\frac{3}{4}\frac{1}{E_{eff}}\frac{1}{\sqrt{R_{eff}}}\right]. \tag{8}$$

Note that k in Eq. (8) is a constant for the entire initial elastic loading segment. The values of P^* and h^* that yield the lowest residual error in the least-squares fit of the initial elastic loading segment to Eq. (8) were chosen to correspond to the effective zero-point. This approach ensures that the corrected data set would be highly consistent with Hertz's theory.

Figure 8 shows an example of a comparison between the zero-points for tungsten as determined by the two methods: (i) Eq. (7) using the CSM, and (ii) Eq. (8) without using the CSM signal. As seen from Fig. 8, both the CSM and the non-CSM data analysis methods for tungsten yield nearly identical values of P^* and h^*. Similar matches were also reported in Ref. [13] over a number of datasets for a range of metallic samples.

It is worth reiterating here that it is possible to analyze the relatively small initial elastic loading segments with remarkable accuracy, because the use of Eq. (7) or Eq. (8) to establish the effective zero-point does not require prior knowledge of the values of R_{eff} and E_{eff}. This is especially beneficial in establishing a reliable value of R_i, i.e. the correct radius of the spherical indenter purchased from the manufacturer (note that in the initial elastic loading segment $R_{eff} = R_i$). For example, in Ref [13] using measurements on samples of known Young's moduli (e.g. Si standards), two indenter radii were estimated to be 1.4 and 20 μm respectively, even though the manufacturer had claimed otherwise. Both these estimates were subsequently confirmed by SEM.

The second step in the extraction of indentation stress-strain curves is an accurate estimation of the contact radius a, which evolves continuously during the indentation experiment. As mentioned in the previous sections, the majority of the methods used for

estimation of a in the literature [14, 15, 45, 50] are motivated by the spherical geometry of the indenter, where a is calculated directly from the indentation depth and the radius of the indenter, R_i. However as noted before, although the relationship $R_{eff} = R_i$ holds in the initial elastic loading segment, R_{eff} can no longer be assumed to be equal to R_i after any imposed plastic deformation in the loading segment. As we shall see later, R_{eff} changes quite dramatically with any imposed plastic deformation by the indenter.

Alternatively, one can impose an elastic unloading segment at any point of interest and analyze it using Hertz's theory in order to estimate the contact radius. Indeed, this is exactly what is done in estimating the contact radius using the CSM [7, 8, 62]. Each unloading segment is fit to the expected Hertz's relationship between the total indentation depth, h_t, and indentation load, P, which may be conveniently expressed as (see Fig. 9a)

$$h_e = h_t - h_r = kP^{2/3} \tag{9}$$

Once the value of E_{eff} is established from the initial loading curve (or if the Young's modulus of the sample material is already known), a regression analysis on the unloading segment can determine both h_r and R_{eff}. The value of the contact radius, a, at any point in the unloading segment is then determined from

$$a = \sqrt{R_{eff} h_e} = \sqrt{R_{eff}(h_t - h_r)}. \tag{10}$$

It should be noted that this relationship between R_{eff} and a is implicit in Hertz's theory for the quadratic contacting surfaces. Applying this equation to the data point just before the initiation of the unloading segment provides the value of the contact radius at that point in the original loading segment. This method does however necessitate a large number of loading-unloading segments in order to be able to get a complete description

of the indentation stress-strain curve for a given sample, since each unloading curve will produce only one point on the indentation stress-strain curve.

Figure 9b shows the values of R_{eff} estimated at different indentation depths, using the data analysis procedure described earlier, in the measurements obtained using a 20μm spherical indenter on samples of electropolished aluminum and tungsten. As seen from this figure, the values for R_{eff} change dramatically with imposed plastic deformation by the indenter. In fact, the changes in the effective radius are most dramatic in the initial stages of plastic deformation under the indenter. It is also seen that R_{eff} takes on much higher values for the softer aluminum samples compared to the harder tungsten samples (at the same depth of indentation). Indeed, it was observed that R_{eff} is not just a function of indentation depth (or load) alone, but varies substantially with the details of the elastic and plastic properties of the sample. This observation raises serious questions regarding the validity of the approaches in the literature that establish calibrated area functions and effective indenter shapes from measurements on a standard material [7, 8], and then use the same on other materials without any other corrections. Note that the values of R_{eff} estimated in Fig. 9b are substantially larger than the indenter radius (R_i = 20 μm). These observations are highly consistent with the findings from finite element simulations described earlier in Section 4.

Figures 10a and b show comparisons between the indentation stress-strain curves obtained using both the CSM method described in Section 5.1 and the non-CSM method above on aluminum and tungsten samples for both 1.4 and 20 μm radii indenter sizes. It is seen that the indentation stress-strain curves from the CSM and the non-CSM methods agree well with each other for both indenters. The indentation stress-strain curve

produced using the non-CSM method is able to capture all the major features of the stress-strain curves including the linear elastic regime, the plastic yield point, and the post-yield strain-hardening. As expected, the indentation stress-strain curve for tungsten shows more strain hardening compared to the aluminum sample. These results also demonstrate the feasibility of capturing the details of the pop-in phenomenon (discussed later in Section 5.4) occurring in the smaller 1.4 μm indenter with the non-CSM method. These findings indicate that in spite of the non-continuous nature of the non-CSM calculations, this method can be successfully used to characterize the mechanical response of the material during spherical nanoindentation.

5.3 Effect of Surface Preparation in Indentation Stress-Strain Curves Analysis

Since nanoindentation is essentially a surface probe technique, any disturbance to the surface quality is likely to have an impact on the nanoindentation results. In this respect, the data analyses procedures described in the previous sections, with their ability to analyze the initial loading segments, are highly suited to gauge the quality of surface finish on the indented materials. In this section, we discuss the precise role of surface preparation on the measured nanoindentation data. Here the focus is on three important aspects that commonly affect the initial nanoindentation loading segments of metallic materials, namely i) presence of a highly disturbed surface layer produced by traditional (mechanical) sectioning and polishing methods, (ii) presence of surface irregularities, such as a rough surface finish or a thin oxide film on the surface, and the (iii) occurrence of ‘pop-ins’ or depth excursions at low loads.

One of the most important factors for producing reliable results in nanoindentation experiments is the careful and reproducible preparation of the specimen surfaces to be analyzed. Great care needs to be exercised in sectioning the sample to minimize the disturbed layer produced in the process. Several of the mechanical sectioning methods (e.g. diamond wheels) leave a relatively large disturbed layer. In such situations, it is important to ensure that the disturbed layer is completely removed in the subsequent polishing steps.

The effect of surface finish on nanoindentation results is illustrated in Fig. 11 which shows the indentation stress-strain curves measured on an annealed sample of W prepared with two different surface finishes: (i) a mechanically polished surface (final polishing step 1 μm diamond polish), and (ii) an electro-polished surface; these measurements were obtained using a 13.5 μm radius spherical indenter. It is clearly seen from this figure that the indentation stress-strain curves for the W surface prepared by rough mechanical polishing are consistently higher than that of the electro-polished surfaces (Fig. 11a), whereas those of electro-polished and vibratory-polished (final polishing step 0.02 μm colloidal silica for ~48 hours) surfaces are in excellent agreement with each other (Fig. 11b). Rough mechanical polishing generally leaves a disturbed surface layer with a higher dislocation content than in the original annealed material. Since the indentation modulus of the material is not altered appreciably by the presence of these dislocations, the main effect of this disturbed surface layer is in the form of an increase in the indentation yield strength and the plastic flow stresses in the material. Furthermore, the indentation yield strengths measured on the mechanically polished samples also result in a large scatter in the measured indentation yield strengths because

of the inherent variability in the surface layer produced by this method of surface preparation.

Since the protocols described in this paper aim to isolate and analyze the initial loading segments in the nanoindentation measurements, they place stringent requirements on the preparation of the sample surface. It should be recognized that the indentation zone sizes in the initial loading segment are very small. The contact radius *a* can be used as a guide in deciding if a good sample surface has been obtained for the measurements. The indentation zone size is typically about 2.4*a*, while the location of the highest stress experienced in the indentation zone is about 0.5*a* directly below the indenter. Therefore, it is extremely important to keep the thickness of the disturbed sample surface to be much smaller than the contact radius *a*. For a 13.5 m indenter, the contact radius for most metals at the elastic limit is of the order of 300-500 nm. The corresponding numbers for a 1 m indenter are of the order of 100 nm or less. Consequently, it is substantially more difficult to obtain suitable surfaces and reliable results with smaller indenters compared to the larger indenters.

The above discussion underlines the importance of a high quality surface finish in obtaining reliable data from nanoindentation experiments, especially in the initial elastic loading segments. For metals, having an undisturbed (virgin) sample surface is highly critical in order to get repeatable and reliable results from nanoindentation that correspond to the properties of the original sample and not to the effects of the sample preparation techniques themselves. Both electro-polishing, where a certain thickness of the metal is removed to generate an undisturbed relatively flat surface, and vibratory-polishing using fine-sized colloidal silica for a significant length of time (~ 24-48 hours),

seem to fulfill these requirements (Fig. 11b). However, as discussed in the next section, electro-polishing may also cause a larger propensity of pop-ins in annealed metallic samples with low dislocation densities.

Surface irregularities are common on most sample surfaces. Common examples include the presence of a thin oxide film on the surface (of metallic samples) and sample-surface roughness, especially in materials where techniques such as electropolishing are not an option (e.g., non-metallic samples such as bone). Our results indicate that the influence of these irregularities, provided they are below a critical threshold, is largely reflected in the very early parts of the measured load-displacement data. Thus, for a metal like tungsten with a ~10 nm oxide thickness on the surface, deleting a slightly larger portion of the initial loading segment brings the measured load-displacement data in excellent agreement with the predictions of the Hertz's theory [65]. A similar observation was made earlier for bone samples. This indicates that the method for finding the effective zero-point using Eq. (7) is able to identify the regime in the initial loading segment consistent with Hertz's theory – as long as the thickness of the disturbed layer or irregularities is significantly smaller than the contact radius at the elastic limit of the initial loading segment in the indentation. However, care should be exercised in measurements on surfaces with a larger oxide layer or a very rough polish. In such situations, one needs to either find a way to remove or reduce the surface layer or use an indenter with a bigger tip radius.

5.4 Pop-in Events

Nanoindentation experiments are sometimes affected by the occurrence of the 'pop-in' events – when the indenter suddenly experiences an increase in penetration

depth without any major increase in the applied indentation load (in a load controlled experiment). These pop-ins, which are generally associated with the onset of significant plastic deformation [73] in the indentation experiment, often generate high stresses that have been estimated to be close to the theoretical limit ($G/2\pi$ [74], where G is the shear modulus) of the material [75-82]. These are attributed to the fact that the indentation zone size in these experiments at the point of plastic yield is comparable or smaller than the dislocation-network length scales in the sample (e.g., spacing of dislocations, dislocation cell size, see the schematic in Figs. 12a and 12c). The occurrence of these pop-ins can therefore be correlated to the difficulty of activating a dislocation source (e.g., Frank-Read source [83]) in the primary indentation zone.

Increasing the indenter radius causes a corresponding increase in the indentation zone size. Hence with the larger indenter, there is a much higher likelihood that the conditions for setting up dislocation sources are more easily attained at lower indentation depths and indentation loads. Consequently, the occurrence of pop-ins during indentation with the larger indenter can be expected to be much more stochastic compared to the indentation with the smaller indenter, as shown for Fe-3%Si steel using a larger 13.5 μm indenter in Fig 12b. With an even larger indenter radius, the pop-ins should disappear completely. Indeed, pop-ins have never been reported with very large (with radii of millimeters and above) indenters.

Pop-ins, which appear as displacement bursts in a load vs. displacement plot, manifest as strain bursts in the indentation stress-strain curves produced using the protocols described earlier. Pop-ins events in vibro-polished samples of Fe-3%Si steel using a 13.5 μm indenter are shown in Fig. 12b. As seen from this figure, the indentation

stress-strain curves after the pop-in event seem to approach the indentation stress-strain curves obtained on the sample without the pop-in. This suggests that the pop-ins observed in these tests are caused by delayed activation of sources for plastic deformation, which essentially extends the initial elastic regime. However, as soon as a good number of sources for plastic deformation are activated, the response is no different than the response obtained in the tests without the pop-in event. In other words, further loading after the pop-in event appears to completely wipe out the memory of the pop-in event; there is no effect on the indentation stress-strain curves at larger indentation strains.

If the pop-ins are indeed caused by delayed activation of dislocation sources, then indentation measurements on cold-worked samples should show a lower propensity for the occurrence of pop-ins. This was verified by conducting spherical indentation on samples of vibro-polished as-cast[1] and 30% deformed samples of Fe-3%Si steel using a 13.5 μm spherical indenter (see Figs. 12b and 12c). It is seen that the occurrence of pop-ins is stochastic in the indentations on the as-cast sample (Fig. 12b), but are completely absent in the indentations on the 30% deformed sample (Fig. 12c). Similarly, rough mechanical polishing – which too increases the dislocation density content in the top disturbed surface layer in the sample – was also found to reduce the occurrence of pop-ins significantly (Fig. 12d).

---

[1] The as-cast state represents a low and uniform dislocation density for the Fe-3%Si sample. However, the same is not true for all metallic systems. For example, FCC metals that contract more on solidification often have a high dislocation density and significant in-grain misorientations due to contraction stresses [84] R.D. Doherty, Scripta Materialia 49 (2003) 1219-1222. These samples would then need to be annealed to attain a low and uniform dislocation density.

Figures 12b and 12d also indicate that an indentation stress-strain plot with an initial pop-in often exhibits a large discontinuity. This makes it difficult to accurately estimate the indentation yield strength (Y_{ind}) from such a plot. Particularly, as-cast or annealed samples with very low initial dislocation density prepared using electropolishing are highly susceptible to this problem. Fortunately vibro-polishing has been found to be an ideal compromise – it introduces only a small number of dislocations into the sample surface, which are enough to suppress the pop-ins for the larger indenter sizes (10 and 13.5 μm radii) but do not appear to influence the measured Y_{ind} on the as-cast samples. This is seen in Fig. 12d, which shows an excellent agreement between the back-extrapolated Y_{ind} obtained on the electro-polished surface (with the pop-in) and the Y_{ind} measured on the vibro-polished surface (without the pop-in).

Following the observations above, both electro-polishing and vibro-polishing of metal surfaces should be explored. Vibro-polishing is particularly advantageous in extracting indentation stress-strain curves from as-cast and annealed samples, as it reduces the propensity for pop-ins. In studies involving grain boundaries, vibro-polishing also reduces the possibility of developing a significant groove at the grain boundary that often results from electropolishing [85, 86]. However, if the aim of the nanoindentation measurements is the study of the pop-ins themselves, then electro-polishing is clearly the preferred procedure.

Indentation stress-strain curves can be highly effective in understanding the physical processes occurring underneath the indenter during and immediately after the occurrence of the pop-in. A close look at the indentation stress-strain curve during pop-ins reveals the following salient features (see Fig. 13 for a pop-in in electropolished W):

(i) During the pop-in event, the indentation stress values remain high and stable, while there is a burst in the value of the indentation strain (Fig. 13a). (ii) Subsequent to the pop-in event, the indentation stress decreases only after a finite amount of additional indentation displacement has been applied. (iii) During this additional indentation displacement, the indentation strain actually decreases producing an unloading segment in the indentation stress-strain curve. (iv) The unloading indentation modulus during this additional indentation displacement (subsequent to pop-in) is generally very close to the indentation modulus measured in the initial loading segment (except when the pop-ins are unusually large [65], as in Figs. 10 and 12). Pop-ins observed in a broad range of materials, including Fe-3%Si (Fig. 12), Al (Fig. 10), Ag, Au, and Cu [13, 64-66], have consistently exhibited the same salient features described above. The above observations are perplexing at first glance as one would intuitively expect a sharp drop in stress during the pop-in event itself.

Given that the load remains constant during the pop-in event (the measurements were conducted in load control), the observation that the indentation stress remains high and almost constant during the pop-in event suggests that the contact radius must also remain more or less constant during the pop-in event (see Fig. 13a). This can be inferred directly from the definition of the indentation stress ($\sigma_{ind} = P/\pi a^2$, see Eq. (6)). However, one would intuitively expect a sudden increase in the contact radius associated with the large excursion in the indentation depth that occurs during the pop-in event. It is interesting that although the excursion in the indentation depth does indeed produce a corresponding increment in the indentation strain, this increment occurs at more or less a constant value of the contact radius. Further evidence for the lack of a sudden increase in

the contact radius also comes from a close inspection of the stiffness signal, which showed that the harmonic stiffness remained more or less constant during the pop-in. This is shown in Fig. 13b through the plot of the contact radius. Since the harmonic stiffness (*S*) is directly proportional to the contact radius a ($a = S/2E_{eff}$, see Eq. (3)), we can again infer that contact radius did not change much during the pop-in event itself. Therefore all measured signals during the pop-in are highly consistent with the inference that the contact radius remains more or less constant during the pop-in event.

A second salient feature in the plots shown in Fig. 13b is that there is a short regime of rapid increase in the contact radius *a* (also seen in the CSM signal) with additional indentation depth immediately following the pop-in. Consequently, there is a rapid decrease in the indentation stress, which in turn produces the unloading segment seen in Figs. 10, 12, and 13a immediately after the pop-in event. In this unloading segment, the contact radius is increasing much faster than the indentation depth. Hence the overall indentation strain decreases in spite of the fact that the total indentation depth is continuously increasing (note how indentation strain is defined: $\varepsilon_{ind} \approx h_e/2.4a$, see also Eq. (6)). Since the indentation stress is decreasing in this unloading segment, it is reasonable that the unloading indentation modulus in this segment is very close to the indentation modulus measured in the initial loading segment.

The data point at the end of this regime of rapid increase in the contact radius is marked with gold color in Fig 13. By tracking the location of this particular data point in the different plots, it is clearly seen that this regime ends when the indentation stress has fallen to the levels consistent with ISS curves without pop-ins.

It is emphasized here that the trends and insights obtained above regarding pop-ins would not have been possible with the traditional data analyses protocols. For example, the use of protocol C (see table in Fig. 3a) would have suggested that the contact radius increased substantially during the pop-in event because an excursion in the indentation depth would automatically produce an increase in the indentation contact depth (h_c). Not only would this inference be inconsistent with the stiffness measurement, it would also produce an unloading segment with a negative slope. Unloading segments in stress strain curves with negative slopes are completely unphysical as they would imply that while the stress is reducing (which has to be accompanied by a reduction of elastic strain) the total strain is simultaneously increasing by significant amounts.

Figure 14 presents a conceptual model for what might happen during a pop-in that is consistent with the observations made above. As mentioned earlier, the pop-ins are produced by sudden activation of dislocation sources (upon reaching a certain combination of local stress and size of the indentation zone), which in turn facilitates plastic strain under the indenter by the familiar process of dislocation slip on specific slip systems [76, 80, 87, 88]. The observations described in Fig. 13 suggest that the slip bursts that occur during the pop-in event are actually altering the profile of the sample surface without changing the contact radius significantly. These uncontrolled slip bursts help diffuse the high elastic stresses under the indenter. It is well known from Hertz's model that the stress fields in the indentation zone are such that the highest driving force for plastic deformation occurs at some distance below the indenter tip (not on the sample surface). For an isotropic material, the highest shear stress (needed to initiate plastic strain) is expected to occur at a distance of $0.5a$ below the indenter, where a is the contact

radius. Dislocations should therefore be expected to start well below the indenter tip, and travel (in bursts) on specific crystallographic slip systems (e.g., [110] directions on (111) planes in fcc metals [89]). It is also important to recognize that the sample free surface is likely to play an important role in facilitating these slip bursts. For example, the rigid conformation of the indenter and the sample in the contact region would not allow the formation of the step-like features needed to release the dislocations. The sample free surface on the other hand will allow the easy release of the dislocations.

The schematic in Fig 14a gives a possible explanation of how the dislocation burst of a pop-in might significantly alter the profile of the free surface of the sample just outside the indenter contact region, while not changing the contact radius itself. Such a process is expected to be asymmetric, i.e. the profile change is expected to happen only over a limited area for a single pop-in. However, any additional indentation depth immediately following the pop-in would cause a sharp increase in the contact radius (and a corresponding increase in the stiffness measurement). This expected rapid increase in contact radius and stiffness immediately after the pop-in matches well with the contact radius (CSM) measurements shown in Fig. 13b.

In order to test the above hypothesis the resultant surface profile immediately after a pop-in event (after the load has been taken off) was mapped using an *in-situ* SEM atomic force microscope (AFM). Figure 14b shows the load-displacement curve of the indentation test on a near-(001) surface of aluminum, where the test was stopped after a single large displacement burst of around 180 nm using a 1 μm spherical indenter. As expected, the pop-in produced a large slip burst on one of the potential slip systems – the one that presumably experienced the largest resolved shear stress during the indentation

loading. This leads to the appearance of a step-like feature and an associated pile-up along the [110] direction as shown in Figs. 14b (inset) and 14c. The AFM surface profile map shown in Fig. 14c indicates that there are major differences in the residual surface profile of the indent between the direction of the slip burst ([110])and normal to that direction ($[\bar{1}10]$), and that the major changes in the sample surface profile have occurred outside the contact region. Thus any further loading of the indenter beyond the burst would cause a rapid rise in *a* and a subsequent decrease in the indentation stress.

The AFM profile shown in Fig. 14b and c also demonstrates the significant anisotropy of the residual imprint. It is easily apparent from these figures that any value of contact radius estimated based on the geometry of the spherical indenter (using Eq. 4 and protocols B and C, see Fig. 4) would be in significant error. Moreover if the indentation is allowed to proceed well beyond the initial burst there would be slip bursts along all of the primary (111) slip planes. Due to the crystallography of the indented (001) surface, the primary slip planes $(1\bar{1}1)$ and (111) would intersect the indented plane along the [110] and $[\bar{1}10]$ directions. Thus the activation of the above slip systems would produce an excess material pile-up in these directions resulting in a four-fold pattern of material pile-up around the indent along the [110] directions, as has been noted in the literature [89].

5.5 Effect of the Continuous Stiffness Measurement on Indentation Stress-Strain Curves Analysis

The introduction of continuous stiffness measurement (CSM) has been one of the significant recent improvements in nanoindentation testing techniques. CSM is

implemented by applying a small, sinusoidally varying load on top of the primary load signal and measuring the amplitude and phase of the displacement oscillation at the same frequency by means of a frequency-specific amplifier [7, 8, 62]. The stiffness (given as the ratio of the load amplitude to the displacement amplitude for elastic contact) can then be measured continuously during the indentation test. The CSM, because of its ability to continuously record the contact stiffness, is central to the extraction of indentation stress-strain curves from the measured raw load-displacement datasets using Eqs. (3-7).

A number of recent reports using sharp tip indenters on both metallic [90-96] and visco-elastic [97, 98] material systems have indicated that the use of CSM can impact directly the values of the measured mechanical properties. These researchers have found that some materials, particularly those with a high Young's modulus to hardness E/H ratio such as Ni single crystal ($E/H \approx 170$) [94], Cu single crystal ($E/H \approx 225$) [91], MgO [96], and Ir ($E/H \approx 210$) [95] show significant softening at low (<100 nm) indentation depths, when using the CSM. Figure 15a describes this effect for hardness (H) values measured on (100) Cu single crystal using a Berkovich indenter [91]. These experiments were performed at various displacement oscillation amplitudes nominally in the range 1–12 nm as characterized by the root-mean-square (rms) displacement amplitude, Δh_{rms}. These researchers used two techniques to measure the hardness – the first using the Oliver-Pharr method of analysis on the load-displacement data using the stiffness values measured by the CSM along with the calibrated area function (based on measurements on fused silica [7, 8]), and the second by imaging the residual imprints from tests with the CSM turned off ($\Delta h_{rms} = 0$). The following observations can be made from this image: (i) at large depths and small amplitudes, the hardness values measured using CSM agree

well with those estimated from SEM images, (ii) at large depths and large amplitudes, the CSM-measured hardness values are significantly lower than the ones estimated from SEM images, and (iii) at small depths, the differences are significant even for small amplitudes.

A part of the discrepancy described above stems from the basic assumption in CSM-related analysis that the amplitude of the oscillation applied is very small, i.e. the effects of such an oscillation on the overall load-displacement behavior can be ignored. This assumption was analyzed critically by Pharr et al. [91], and was found to break down for materials with a high Young's modulus to hardness E/H ratio. The authors identified three main sources of error in the data analyses protocols with the CSM. Firstly, the load and the displacement values are underestimated with the use of CSM. This is due to the fact that the machine does not record the peak values of load and displacement when using the CSM, but rather their mean values during the oscillation cycle. However, the material being tested actually experiences the load and displacement corresponding to the maxima of the superimposed oscillations. Pharr et al. suggest the following simple corrections for this error:

$$P_{act} = P_{app} + \frac{\Delta P}{2} \quad \text{or} \quad \mathrm{P_{act}} = P_{app} + \sqrt{2}\Delta P_{rms} \tag{11}$$

$$h_{act} = h_{app} + \frac{\Delta h}{2} \quad \text{or} \quad \mathrm{h_{act}} = h_{app} + \sqrt{2}\Delta h_{rms} \tag{12}$$

where P and h refer to the load and displacement signals, respectively, and the subscripts *act* and *app* refer to the actual values experienced by the sample and the apparent values recorded by the machine, respectively. ΔP and Δh are the peak-to-peak load and displacement ranges, respectively, associated with the superimposed oscillations when

using CSM. The corrections are easy to apply since the machine provides the *rms* values of the oscillating signal.

The second source of error results from an underestimation of the contact stiffness (S). The apparent stiffness ($S_{app} = \Delta P/\Delta h$) reported by the machine is essentially the ratio of the peak-to-peak amplitudes of the load and displacement signal. However, from Hertz theory [17, 31], it is known that the relationship between load and displacement is not linear in the elastic regime (Eq. 1), and therefore this measurement underestimates the stiffness at peak load. By modeling the unloading curve in nanoindentation, the actual stiffness S_{act} can be computed from the apparent stiffness S_{app} as follows:

$$S_{act} = \frac{1}{\sqrt{2\pi}} \frac{P_{\max}}{\Delta h_{rms}} \left(\frac{1}{K}\right)^{1/m} \left[1 - \left(1 - \frac{2\sqrt{2}\Delta h_{rms} S_{app}}{P_{\max}}\right)^{1/m}\right] \tag{13}$$

where S_{act} is the corrected stiffness signal, K and m are constants (K = 0.757 and m=1.38 for Berkovich indenters [91] and K = 0.6524 and m=3/2 for spherical indenters [99]).

The third source of error identified in Ref. [91] arises from the loss of contact between the indenter tip and the sample at low loads during the dynamic oscillations. This is specially true for materials with a high Young's modulus to hardness E/H ratio, where the amount of dynamic unloading during the displacement oscillation may become larger than the total applied force (at small total depths of penetration). When this happens the indenter behaves as the tapping mode operation of an atomic force microscope, where it lifts from the surface and loses contact during part of the oscillation cycle. Note that while this process has been successfully modeled in Ref. [91] including estimations of the depth below which tapping occurs, no corrections were suggested for

this error. The authors of Ref. [91] recommend that the measurements be performed at smaller displacement oscillation amplitudes in order to reduce this error.

The hardness data for Cu (100), with corrections to P, h, and S (Eqs. 11-13), is shown in Fig 15b. It is apparent that as compared to the uncorrected data in Fig. 15a, the corrected CSM-hardness curves are higher. The CSM-hardness values after corrections also match well with the hardness values measured directly in the SEM for large indentation depths. However at small depths, the tapping problems prevail, and the measured hardness values, even after correction, continue to underestimate the true values.

The effects of the CSM corrections (Eqs. 11-13) on the extraction of indentation stress-strain curves from spherical indenters and on the estimations of the contact radius have been studied in detail by Vachhani et al. [99] and is summarized in Figs. 15c-15f. Note that the data shown in these figures have already been corrected for the effective zero-point (using Eq. 7) which also indirectly corrects for the tapping problem mentioned earlier. Figures 15c and 15e show the original harmonic stiffness-displacement (S-h_t) and indentation stress-strain responses for high purity 20% deformed aluminum measured using a 100 μm radius spherical tip over a range of frequencies and Δh_{rms} values, while Figs. 15d and 15f show the same after using the corrections mentioned above in Eqs. 11-13 respectively. The values for the harmonic contact stiffness are seen to be progressively lower for the tests carried out with CSM at 10 Hz–2 nm and 10 Hz–1 nm oscillations respectively particularly at higher indentation depths, compared with the tests carried out at 45 Hz frequency (Figs. 15c, 15d). On the other hand, the 45 Hz–1 nm oscillations showed higher levels of inherent noise in the stiffness signal. The authors also observed

that the corrections from Eqs. 11-13 produced relatively minor changes when applied to the harmonic stiffness data; they failed to bring the curves for the displacement–harmonic stiffness data with the different CSM conditions closer (compare the different plots in both Figs. 15c and 15d).

Similar trends were also seen in the indentation stress-strain data (Figs. 15e, 15f). Thus the data is noisiest for the tests carried out at the 45 Hz–1 nm test condition, and the tests carried out using the 10 Hz–2 nm and 10 Hz–1 nm CSM conditions show pronounced post-elastic hardening, with the effect being most severe for the latter. Since both stress and strain are inversely related to the contact radius and hence inversely related to the stiffness as well (see Eqs. 3-7), these trends can be directly related to the lower stiffness values recorded for these test conditions. The authors in Ref. [99] have hypothesized that the decrease in the stiffness values at higher indentation depths is a likely artifact of the machine dynamic control system, while the higher noise levels for the stiffness signal obtained for the 45 Hz–1 nm CSM condition could be due to the fact that this test condition presents the most difficult case for the feedback control to accurately maintain low-amplitude–high-frequency oscillations.

The corrections in Eqs. 11-13 appear to have a much smaller effect on the spherical indentation stress-strain curves as compared to their effect on the raw data (compare Figs. 15a, 15b to Figs. 15c-15f). The results in Ref. [99] suggest that the corrections to individual signals appear to negate each other to some extent in the indentation stress-strain computations. In some cases the corrections can also be detrimental to the indentation stress-strain calculations; for example most of the initial

elastic segment for the 45 Hz–2 nm CSM condition was lost while correcting for the stiffness signal using Eq. 13 (Fig. 15f).

Thus, for accurate estimation of the indentation stress-strain curves, the authors in Ref. [99] suggest that the CSM corrections (Eqs. 11-13) be skipped altogether; the CSM signal at 45 Hz–2 nm oscillations was also deemed to be the most reasonable choice for indentation stress-strain calculations.

6. Applications: Combined OIM - Indentation Studies on Metallic Samples

Since the length scales in nanoindentation are smaller than the typical crystallite (also called grain) sizes in polycrystalline samples, this technique is an ideal tool for detailed characterization of the microscale heterogeneities present in these materials and their evolution during various metal shaping/working operations. The local mechanical properties measured at these length scales using indentation are expected to be strongly dependent on the local material structure at the indentation site. For example, one should expect the local lattice orientation(s) at the indentation site to influence strongly the elastic-plastic properties extracted from the indentation datasets obtained on polycrystalline samples. However, in most currently used experimental protocols, the differences in properties extracted from different locations on a given polycrystalline sample are often treated as "experimental scatter" and just averaged in reporting the measured properties. It is argued here that these differences arise because of the inherent differences in the local material structure at the indentation site. For example, it is fully expected that the indentation yield strength (Y_{ind}) will vary significantly from one crystal

orientation to another, even in fully annealed samples where there are no major differences in the dislocation content of the differently oriented grains (see the illustration in Fig. 16a). This is because the plastic deformation imposed by the indenter needs to be accommodated locally at the indentation site by slip activity on the available slip systems, whose orientation and activation are strongly dependent on the local crystal lattice orientation with respect to the indentation direction. It is now possible to measure the local lattice orientation in polycrystalline samples using a technique called Orientation Imaging Microscopy (OIM) [100, 101]. This method is based on automated indexing of back-scattered electron diffraction patterns (obtained using a scanning electron microscope) and has a spatial resolution of less than a micron, with certain new enhancements promising to improve the spatial resolution to below 10 nm [102]. Therefore, coupling the structure information obtained from OIM with the mechanical data obtained from nanoindentation should produce vastly enriched datasets that are potentially capable of providing new insights into the local elastic-plastic properties of interest.

Additionally, when subjected to plastic strain (especially when deformed at low homologous temperatures; also called cold-working) metallic samples are known to harden significantly. However, as a result of the grain-scale heterogeneity in their microstructures, the individual grains do not harden equally. This is demonstrated schematically in Fig. 16 for as-cast and 30% deformed polycrystalline samples of Fe-3%Si steel. Fig. 16c shows the indentation stress-strain curves obtained from the raw displacement datasets shown in Fig. 16b respectively. Of main interest here are the differences seen in the elastic indentation moduli, the indentation yield strengths, and the

post-yield characteristics in the measurements at different locations in the as-cast samples and in the deformed samples. Indeed these differences are more easily seen in the indentation stress-strain plots compared to the raw load-displacement plots. We note again that it is only possible to extract reliably the estimates of the indentation moduli and the indentation yield strength from the initial elastic portion of the indentation stress-strain curve, because the indentation itself will alter the local microstructure and its properties once it imposes additional local plastic deformation.

In this section, we illustrate how the data obtained from the initial loading segments of spherical nanoindentation, when combined with the complementary structure information measured locally at the indentation site, can be utilized to provide new physical insights into the local elastic-plastic properties of interest. Using a series of examples, we demonstrate that it is possible to extract information on the local elastic-plastic properties of constituent single crystals in a polycrystalline sample. We also demonstrate the potential of this new approach to interrogating the mechanical response of interfaces (e.g., grain boundaries) in the samples. New physical insights into all of the phenomena mentioned above at these lower length scales are crucial for the further development of physics-based multiscale material models for polycrystalline material systems.

6.1 Quantifying Elastic and Plastic Anisotropy of Single Crystals

As discussed above, the changes in the yield strength of individual grains in a polycrystalline metallic sample are a combination of both the local crystal lattice orientation at the indentation site as well as the macroscale plastic deformation imposed on the sample. Therefore, a rigorous methodology is needed to decouple these two effects

– once we can successfully account for the effect of the crystal lattice orientation on the indentation yield strength it should then be possible to estimate the local increase in the average slip resistance (and hence indirectly estimate the dislocation content) at the indentation site [103].

One major challenge in using indentation stress-strain curves for this task arises from the fact that the mechanical response of individual grains is inherently anisotropic, whereas the nanoindentation data analyses methods shown in Eqs. (6) and (7) are built on Hertz's theory [17] that assumes an isotropic elastic material behavior. The problem of elastic indentation of anisotropic samples has been studied in detail by Vlassak and Nix [104, 105], who propose a modified form of Hertz's analysis designed for cubic materials. These authors demonstrate that Eqs. (2) and (3) can be used for elastic indentation of cubic crystals, provided an anisotropy parameter, β, is appropriately introduced into the definition of the effective indentation modulus. In particular, they show that Eq. (2) can be modified as

$$\frac{1}{E_{eff}} = \frac{1}{\beta}\left(\frac{1-\nu_s^2}{E_s}\right) + \left(\frac{1-\nu_i^2}{E_i}\right) \tag{14}$$

In Eq. (14), E_s and ν_s denote the effective values of Young's modulus and Poisson's ratio, respectively, for a randomly textured polycrystalline aggregate of crystals with the same elastic properties as the single crystal being studied [104, 106]. For cubic crystals, the value of β depends strongly on the crystal lattice orientation and the degree of cubic elastic anisotropy. The elastic anisotropy (A) of a cubic crystal is usually defined by $A = 2C_{44}/(C_{11} - C_{12})$, where C_{11}, C_{12}, and C_{44} denote the cubic elastic constants used to define the crystal elastic stiffness in its own reference frame.

The modified form of Hertz's theory shown in Eq. (14) is highly amenable to the analyses protocols described earlier for obtaining nanoindentation stress-strain curves. This has been demonstrated in Ref. [66] using measurements on as-cast polycrystalline samples of Fe-3%Si steel with very large (~mm) sized grains. The OIM scan of the sample used in Ref. [66] is shown in Fig. 17a. The OIM scans are color-coded to reflect the positions of the orientations in the inverse pole figure map in Fig. 17b using the standard convention (i.e. grains colored red, green, and blue have (001), (101), and (111) crystallographic planes parallel to the sample surface respectively). As seen from Fig. 17a, the selected region of the sample has a range of grain orientations that provide a good coverage of the corners of the fundamental triangle in the inverse pole figure map shown in Fig. 17b. Because of the very large grains in the sample, the indentation measurements in any one grain are also unlikely to be influenced by the neighboring grain orientations or grain boundaries.

For the as-cast sample shown in Fig. 17a, the anisotropic elasticity parameter β, and the back-extrapolated indentation yield strengths Y_{ind}, were calculated [66] for a total of 11 different grain orientations. The values of β were computed using Eq. (14), by assigning the values of E_s and ν_s to be 207.9 GPa and 0.3 following the approach described in [104, 106], while Y_{ind} was calculated using the back-extrapolation method shown in Fig. 16c. The grain orientation, measured by OIM, is in general described by a set of three angles called Bunge-Euler angles [107], usually denoted as $(\varphi_1, \Phi, \varphi_2)$. Since the rotation of the sample about the normal to the indentation surface (i.e. the ND direction) does not influence the measurements presented here, the indentation modulus

and the indentation yield strengths measured using a spherical indenter are functions of only two of the Bunge-Euler angles, namely (Φ, φ_2).

By interpolating the values β and Y_{ind} in the 11 grains studied, contoured surface plots of the dependence of β and Y_{ind} on the grain orientation were obtained, and are shown in Figs. 17c and 17d, respectively. As seen from Fig. 17c, the measured differences in the indentation moduli range from a minimum of $\beta = 0.92$ to a maximum of $\beta = 1.12$. These measurements are highly consistent with the values predicted by Vlassak and Nix [104], who predicted values of 0.90 for (001) oriented grains, 1.04 for (101) oriented grains, and 1.10 for (111) oriented grains based on an anisotropy factor of A=2.84 for Fe-3%Si. Another important observation from Fig. 17d is that the differences in the measured Y_{ind} values of different grain orientations are as high as 30%. Since there are no expected differences in the dislocation content of the differently oriented grains in the as-cast sample studied here, all of the observed differences in the indentation yield strengths are attributable to differences in the activities of the different slip systems in the different grains and their orientation with respect to the indentation direction (see the illustration in Fig. 16). Note also the similarity between the two plots in Figs. 17c and 17d, indicating a high degree of correlation between the measured indentation moduli and the indentation yield strengths for the differently oriented grains. Similar results have also been obtained for fcc metals, attesting to the broad applicability of the protocols described above [108]. For the fcc metal studied, it was shown that the influence of the crystal lattice orientation on the measured indentation yield strength could be as large as 40%, with the lowest values corresponding to the [100] (cube) orientation and highest values corresponding to the [111] orientation. The value of these plots (especially the plot

for Y_{ind}) will become clear as the data analysis methods for deformed samples are discussed in the next section.

6.2 Estimating Local Slip Resistance in Deformed Cubic Crystals

In order to track and estimate the changes in the local slip resistance in deformed samples we first need to account for the effect of the crystal lattice orientation at the indentation site. It is suggested that the plots shown in [66] and in Figs. 17c and 17d capture this effect quite accurately for Fe-3%Si, and could be used in studies on the deformed samples of this material.

As a specific example, one of the as-cast Fe-3%Si samples was subjected to 30% reduction in simple compression, and another as-cast sample to 80% reduction in plane strain compression (see Fig. 18). These reduction levels were selected to produce one moderately deformed sample and one heavily deformed sample. Indentations were performed in selected regions within individual grains in each of the deformed samples. The indentation measurements on the deformed samples are summarized in the table in Fig. 18c. For each of the grains studied in the deformed sample, the indentation yield point was estimated in the fully annealed condition using the grain orientation and the contoured plot presented in Fig. 17d. In other words, this would have been the indentation yield point if the same grain was in the as-cast sample. As discussed in the previous section, it is important to establish this value because it can vary by as much as 30% from the near-(001) "soft" orientations to the near-(111) "hard" orientations. The difference between the measured indentation yield point in the deformed sample and the estimated indentation point in the as-cast condition then provides a reliable estimate of the increment in the indentation yield point at the indentation site in the deformed

sample. This increment can be attributed to the changes in the dislocation content at the indentation site from its initial state in the as-cast sample (see the illustration in Fig. 16).

The simplest relationship one can establish between the increment in the indentation yield point and the local dislocation content is through the increment in the critical resolved shear strength of the slip system. In a highly simplified approach, this relationship has been expressed in [66] as

$$Y_{ind} = M(\Phi, \varphi_2)\tau_{CRSS}, \qquad \Delta\tau_{CRSS} \propto \sqrt{\rho} \tag{15}$$

where M is a Taylor-like factor that depends only on the grain orientation, τ_{CRSS} is the averaged critical resolved shear stress in the crystal, $\Delta\tau_{CRSS}$ is the increment in the local averaged critical resolved shear strength between the as-cast and cold-worked conditions, and ρ is the local dislocation density. Since the factor M is the only orientation dependent variable, it is easy to see that percentage increase in the indentation yield point should be equal to the percentage increase in τ_{CRSS}. These are reported in the table in Fig. 18c for all the measurements obtained on the deformed sample [66]. The percentage increases in τ_{CRSS} provide an indirect measure of the local dislocation content or the local stored energy in the deformed sample. As seen from the table in Fig. 18c, the changes in τ_{CRSS} vary significantly from one deformation step to another and also from one region to another in the same deformed sample resulting in a heterogeneous microstructure in the deformed polycrystalline samples. It is also clear from Fig. 18c that any conclusions drawn regarding the local slip resistance or the local dislocation content directly from the measured indentation yield points without accounting for the effect of the crystal lattice orientation at the indentation site would be erroneous.

The protocols described above have the potential for opening completely new avenues of research by facilitating the measurement of both local structure (using OIM) and its associated mechanical properties (using spherical indentation). For example, numerous studies have been reported in the literature [109-112], where the microstructure evolution during finite plastic strains in polycrystalline samples has been carefully documented using OIM. While the goal of these studies was to derive a better understanding of the microscale deformation mechanisms in these materials, they were significantly limited by the inability to document the corresponding evolution of the local mechanical properties (at the grain-scale). The combined OIM-spherical indentation approach was utilized by Stojakovic [113] in his investigations on the effects of thermo-mechanical processing on polycrystalline Fe-3%Si samples with columnar grains. This is shown in Fig. 19 which illustrates the deformation of the columnar Fe-3%Si sample to a true strain of 1.21 in plane strain compression. In this sample, the compression was interrupted at selected strain levels and the microstructure was documented using OIM and the evolution of the local mechanical (plastic yield) properties were tracked using the spherical nanoindentation protocols described above. Only minor changes are visible in Fig. 19a as the strain is increased first to 0.34 and then to 0.81, apart from a slight increase in grain misorientation and a steady grain elongation in the rolling direction (the horizontal direction in the figure). However at the highest strain of 1.21 the sample develops significant heterogeneity at the grain-scale (both between grains as well as within the original grains) in both structure as well as mechanical properties (see the table in Fig. 19b). It is seen that the B regions of the split grains have rotated away from their initial orientations, and they also show a large difference in indentation yield behavior

from their A counterparts (see grains 5A, 5B, 6A and 6B in particular). It is therefore now possible to acquire a very large amount of information using this approach, which when carefully analyzed will provide new insights into the microscale mechanisms of plastic deformation in polycrystalline metals.

In this a more recent study, the approaches described above have been successfully demonstrated on deformed polycrystalline samples of Al (an fcc metal) [108]. Of particular note was the fact that the a clear positive correlation was observed between the percentage increase in the local slip resistance and the value of the Taylor factor computed for the local crystal orientation at the indentation site subjected to the macroscale imposed deformation (see Fig. 19c). This important observation suggests that orientations with a lower Taylor factor (soft grains) harden at a lower rate compared to grains with a higher Taylor factor (hard grains). In fact, the authors go on to explain the observed linear relationship in Fig. 19c with a highly simplified physical model for the hardening rate in each grain.

The above examples demonstrate a meaningful approach for extracting correlations between local crystal lattice orientation measurements obtained from OIM and the estimates of local elastic and yield properties from nanoindentation measurements.

6.3 Investigations of Grain Boundary Regions

Indentation stress-strain curves – due to their ability for obtaining meaningful mechanical information from indentation depths of as small as a few nanometers – have great potential in interrogating the mechanical role of interfaces (e.g., grain boundaries) in a polycrystalline sample. Since this technique can be applied across individual grain

boundaries in a polycrystalline sample, they can be efficiently used to probe the physical origins of a number of interface-related strengthening mechanisms (e.g., the well-known Hall-Petch effect [114, 115]) in these materials.

As described in the earlier sections, the use of these indentation stress-strain curves makes it possible to analyze the initial loading segments of spherical indentation, thereby allowing us to obtain measures of indentation modulus and indentation yield strength of the material prior to the damage induced by the indentation itself. This approach is fundamentally different to other indentation studies involving grain boundaries reported in the literature which have primarily focused on measuring the resistance offered by grain boundaries (i.e. the hardness) to dislocation transmission across them using sharp (Vickers, Berkovich, cube corner) indenters [85, 86, 116-124]. In these studies, the sharp indenters introduced substantial amount of plastic deformation in the sample before the dislocations were pushed to the grain boundaries and impeded by them. Therefore, the plastic deformation introduced by indentation in those experiments is likely to strongly influence the mechanical property being measured.

The effect of plastic deformation caused by the indentation itself was systematically studied by Eliash *et al.* [85] in their study of indentation hardness across grain boundaries in molybdenum, and is shown in Fig. 20. The grain boundary affected zone in the figure can be seen to become progressively less pronounced with increasing maximum indentation load (and hence increasing plastic deformation due to indentation). For indentation loads exceeding 10 mN (for a Berkovich tip) the indentation induced hardening masks the effect completely and the trend vanishes. Indeed the subtle changes of hardness across the grain boundaries have only been reported for low load indentations

[86, 116, 119, 121-123]; indentations at high loads have been a poor indicator for measuring grain boundary strengthening effects [120, 125]. Moreover, under such high loads, significant indentation strain imposed by the indenter can also cause the local crystal orientation under the indenter to change [66]. These studies point to the importance of calculating the contact stresses at or close to yield in indentation experiments.

The application of spherical nanoindentation stress-strain curves as an effective tool for this purpose was demonstrated in [64] where the authors measured the differences in indentation modulus and yield stresses across grain boundaries both as a function of the grain boundary character (high vs. low angle grain boundary measured using OIM), and imposed cold work on the sample. The main results are presented in Fig. 21. In this figure, the grains are labeled as 'soft' and 'hard' in a relative sense based on their indentation yield strengths. Figure 21a shows the results for the as-cast Fe-3%Si samples. Since the as-cast samples are not expected to have any excess dislocation storage at the grain boundaries, both E_{eff} and Y_{ind} are fairly uniform in each grain and there is almost a step transition at the grain boundary.

However the response changes markedly once the samples are deformed to 30% (Fig. 21b). Here although the values of E_{eff} are fairly uniform in each grain and show a step like transition at the grain boundary (as in the as-cast sample), the variation of Y_{ind} indicates a substantial transition zone on one side of the grain boundary. Further insights are obtained when these values are normalized to account for the orientation dependence of the indentation measurements (following the procedure discussed earlier in Section 6.2). Since the percentage increase in the Y_{ind} can now be interpreted as the percentage

increase in the local slip resistance (and hence as an indicator of the local dislocation density) at the indentation site, it appears that the grain boundary region on the side of Grain D5 accumulated much less dislocation density in the immediate vicinity of the grain boundary than far away from the boundary. Furthermore, the dislocation density very near the grain boundary on the side of Grain D5 is also seen to be somewhat lower than the dislocation density in the grain boundary region on the side of Grain D4. These observations suggest that the nature of the grain boundary or the grain boundary character on both sides of a grain boundary can be substantially different from each other. In other words the grain boundary on the side of Grain D5 is thought to be acting as an efficient dislocation sink by absorbing the dislocations from the grain boundary region on the side of Grain D5. The above example demonstrates how monitoring the changes in Y_{ind} can offer indications about the roles of certain grain boundaries in mechanical deformation. Similar trends were also reported more recently for polycrystalline deformed samples of Al [126].

6.4 Investigations of Surface Modifications

The indentation stress-strain protocols described here in the review paper are particularly attractive for systematic studies of surface modifications (e.g., coatings, irradiated layers, shot-peened surfaces) because of the extremely small indentation volumes (with length scales as small as 50 nms). An example of the versatility of this approach has been shown in the work of Wheeler et al. [127] in their study of electrolytic coatings which are routinely used to modify the surface of a 5052 aluminum alloy (AA5052) up to a depth of 50-100 μm. Figure 22 compares the main results of their work across the cross-sections of two leading electrolytic coating methods – hard anodizing

and plasma electrolytic oxidation (PEO) on AA5052. Note the significant differences in the indentation stress-strain responses of the modified surfaces as compared to the original AA5052 substrate. The PEO coatings also show higher yield stresses and post-yield hardening as compared to the anodized coatings, with the highest values coming from the tests located closest to the substrate-coating interface. These effects have been correlated in [127] to the differences in the microstructure of the modified surfaces (crystalline vs. amorphous for PEO and anodized respectively), as well as changes in porosity and crystallinity with distance from the substrate-coating interface.

Other surface modification techniques, such as the study of mechanical degradation of irradiated materials [128-130], are more challenging because of extremely small thickness of the damaged layer (typically less than a micron, Fig. 23a). Most commonly used nano-mechanical test techniques, such as ones requiring the use of focused ion beams (FIB) to fabricate micro-pillars or any other such small scale test geometries [131-135], are not likely to be able to address this challenge. Nanoindentation, with its high resolution load and depth sensing capabilities, shows the greatest promise due to its non-destructive nature, ease of experimentation (only a polished surface prior to ion irradiation is needed) and versatility [3, 131, 136-138].

One of the main advantages of nanoindentation techniques is that it allows a systematic study of the local mechanical responses at different length scales, accomplished by simply varying the indenter tip radii. As an example the table in Fig 23d shows the approximate indentation depth (h_t) and the corresponding contact radius (a) and the depth of the indentation zone (which scales as $2.4a$, see Eq. 6) at yield in annealed tungsten for 4 different indenter radii. A proper choice of indenter size can thus

match the volume probed by nanoindentation (Figs. 23a and 23b [44]) to the depth of radiation-damaged (or any other surface-modified) region of interest (Fig. 23c). Furthermore, the ability to make a large number of measurements on a given sample surface also has the potential to provide quantitative information on the variance of properties in the irradiated layer.

Figures 24a-24c show spherical nanoindentation measurements reported recently [139] on annealed (not irradiated) and He ion-irradiated samples of electro-polished polycrystalline tungsten using indenters tips of different radii. Only indents located in the center of the grains (of size 20-50 μm), well away from any interfaces, are shown in this figure. All of the measurements reported in these figures were for grains whose surface normals were very close to [100] directions. These grains were purposely selected to avoid the need to correct for the effect of the lattice orientation at the indentation site in comparing the different measurements presented in these plots (see Section 5.1).

The indentation stress-strain curves from the irradiated samples revealed several interesting features. Strikingly, none of the measurements (including the measurement with the smallest indenter tip R_i = 1 μm, Fig 24a) revealed any pop-ins (cf. the measurements on the annealed samples which clearly show pop-ins for the measurements with the smaller indenters). This is consistent with the expectation that the ion-irradiation introduces a large density of defects in top surface of the material (e.g., radiation induced defects such as dislocation loops [140], He bubbles, etc.) that can help set up highly potent dislocation sources without any need for pop-ins [141]. Another obvious consequence of these new defects introduced by irradiation is that the Y_{ind} values in the irradiated samples are higher than the corresponding values in the annealed samples. It is

also observed that in addition to the higher yield values, the irradiated samples are exhibiting higher hardening rates compared to the annealed samples.

As mentioned earlier, upon ion-irradiation the metal surface is modified by a thin radiation-damaged layer (see Fig. 23a), and investigations with different indenter radii can help ascertain the depth and severity of this damage (see the illustration in Fig. 24d). The post-yield measurements on the He-irradiated near (001) grain with the 1 m radius indenter tip (see Fig 24a) indicate a zone of very high strain hardening (within a short range 0.03-0.1 of indentation strains) followed by a regime of near stress saturation [140, 142, 143] with a slight softening in stress from 11.6 to 10.5 GPa. The contact radius in this test was estimated to range from ~32 nm at Y_{ind} to ~200nm at an indentation strain of 0.1 (end of hardening zone) to ~500 nm at the end of the test (indentation strain of 0.2). The indentation stresses at a ~500 nm were still significantly higher (10.5 GPa) in the irradiated sample as compared to the annealed material (6.2 GPa) tested with the same indenter. These observations indicate that the damage layer due to irradiation extends to depths of the order of 500 nm (assuming that the active indentation zone size is at least of the order of the contact radius a, see Figs 23a-c). On the other hand, the corresponding measurements with the R_i = 10 m indenter tip (Fig. 24b) show an initial post-elastic zone of a high strain hardening (from an indentation strain of 0.02 to 0.045) followed by a regime of marked softening. Note that the softening regime brings the indentation stress values in agreement with the values measured with the same indenter on the annealed samples. These measurements suggest that the initial hardening regime for the R_i = 10 m indenter is attributable to the plastic deformation induced by the indenter in the irradiated top layer, while the later softening regime is attributable to the expansion of the plastic

zone to the undamaged annealed region below the irradiated top layer. Support for this hypothesis comes from the estimated values of the contact radius in this measurement (using Eq. 3). The contact radius for the R_i = 10 m indenter after irradiation is estimated to be ~260 nm at Y_{ind}, ~500 nm at the peak indentation stress level, and a~1.5 μm at the end of the test (Fig. 24b). These measurements suggest that the irradiated layer in this sample is of the order of 500 nm.

As expected, in the measurement with the larger R_i =100 m indenter tip (Fig 24c) the differences between the measurements from the annealed and the irradiated samples are very small. This is not surprising since the contact radii at Y_{ind} for both the annealed and irradiated cases are around a~1 μm for the 100 m radius indenter tip, i.e. at yield the indentation zone extends well beyond the radiation damaged region.

The measurements shown in Figs 23-24 demonstrate the viability and tremendous potential of the spherical indentation stress-strain curves in investigating the changes in the mechanical response of nuclear materials with radiation damage. A similar approach can also be used for other materials with modified surfaces – which can form either as a consequence of a graded or layered [144] microstructure, or when such changes are caused unintentionally, such as in wear applications [145], or due to an intentional alteration of the surface such that its physical, chemical or biological characteristics are different that the bulk of the material– all of which are of increasing interest for a variety of applications ranging from enhanced wear and corrosion resistance, superior thermal and biomedical properties, higher fracture toughness, and reduced stress intensity factors etc. [146, 147].

6.5 Comparing with Micro-pillar Compression Experiments

A major advantage of using indentation stress-strain curves in the case studies described above is in their ability to reliably measure the material properties (such as indentation modulus and indentation yield strength) from the initial loading segment of the tests. This is in contrast to traditional hardness measurements which utilize the unloading segments of the indentation experiments and are thus influenced by the imposed additional local plastic deformation which can alter the local microstructure and its properties. Since the properties measured by the indentation stress-strain curves are thus representative of the pristine undamaged material, it should be possible to develop a one-to-one correlation between these values and those measured using traditional uniaxial testing techniques.

Figure 25 displays an example of the comparative stress-strain responses between indentation and compression on as-cast and 30% deformed Fe-3%Si samples. Both the indentation and compression experiments shown in this figure were done inside individual grains of near (100) orientation (grains #1 and #D4, see Fig. 21). The large (~mm) size of the grains in this sample help insure that these results are free from the influence of neighboring grain orientations and/or grain boundaries. For the compression tests, micro-pillars of ~3 μm diameter and ~ 6 μm height were fabricated using a focused-ion beam (FIB), which were then tested using a custom-built instrumented in-situ flat punch indenter inside a Zeiss DSM 962 SEM chamber [148, 149].

It is reassuring to note that both the indentation and micro-compression experiments demonstrate very similar trends. Thus while there is a 46% increase in the indentation yield strength (Y_{ind} see Fig. 18c) of the Fe-3%Si sample after 30%

deformation, a very similar (around 43%) increase is also noted in the yield strength (calculated as the flow stress at 2% offset strain) of the uniaxial micro-compression experiments. Since the orientations of both the grains #1 and #D4 are very close to near-(100) orientations, these increments are directly related to the changes in the dislocation content between the two samples. Figure 25 suggests that stress-strain responses from both indentation and micro-compression experiments are capable of quantifying these differences. Indentation stress-strain curves, with its potential for high throughput, has a distinct advantage in this respect, since it requires far less resources and operator time as compared to FIB-fabricated micro-pillars.

Another important observation from Fig. 25 is the difference in the post-yield behavior between the two test methods. These are of course influenced by the specific strain paths involved in these tests and need to be studied in more detail. In particular, the tests on deformed samples constitute a strain-path change (e.g., from the 30% reduction in plane strain compression to indentation strain modes), and deserve careful consideration in extracting useful post-yield plastic deformation parameters from both these test methods.

7. Applications: Combined Raman Spectroscopy-Indentation Studies on Bone

Beyond structural metals, indentation stress-strain curves have also enjoyed a fair degree of success in elucidating structure-property relationships in other materials systems, including the study of micrometer and sub-micrometer sized domains in biological materials such as bone [21]. Bone has highly complex hierarchical internal

structure that gives it the capability to perform diverse mechanical, biological and chemical functions. The relevant components span several hierarchical length scales from the material level (including its basic building blocks of collagen fibrils and mineral crystals, and their organization and composition), to tissue level organization and distribution, to the size and geometry of whole bone organs and their macroscale internal components [150-152]. Due to the complex details of this internal hierarchical structure [153], bone is a particularly challenging material to characterize mechanically, especially at the micron length scales where the mineral and collagen components are closely intertwined and the available testing methods are limited. Multiple studies involving nanoindentation have tried to correlate tissue level variation in mechanical properties of bone relative to animal age [154], tissue age and composition [155-157], genetic background [158-160] or even to assess the effects of specific diseases [161] or treatment conditions [162]. These studies have shown mixed results, with some showing support for relationships between local properties and variables affecting tissue composition (e.g., [154, 163]), and others not [157]. To a large extent the inability of these studies to elucidate such structure-property relationships in bone can be attributed to the specific data analyses protocols used in these studies. Since most of these studies involve estimations of indentation modulus and hardness from the unloading segments of load-displacement curves (after some amount of elastic-plastic loading), these property estimates often reflect values which have been changed by the experiment itself. Moreover the sharp indenter tip geometries (such as Berkovich and cube corner) used in these studies generally have a very small initial elastic regime, which makes it difficult to follow the elastic-plastic transition in these materials.

On the other hand, the use of spherical nanoindentation stress strain curves allows one to reliably follow the changes in the mechanical response in the biological material. More importantly, the use of these indentation stress-strain curves makes it possible to analyze the initial loading segments of spherical indentation, thereby allowing the indentation modulus and indentation yield strength of the material to be estimated prior to the damage induced by the indentation itself.

The use of indentation stress-strain curves on biomaterials (enamel and dentin) was initially demonstrated by Angker and Swain [16]. Recently, the use of this technique on bone samples has also been validated by Pathak et al. [63]. In their work, Pathak et al. [63] have utilized samples from two different strains of inbred mouse, A/J and C57BL/6J (B6), which are known to significantly differ in their matrix mineralization and whole bone brittleness [164-167]. Because of the pre-existing detailed knowledge of the growth patterns in the selected mouse strains [166], these samples form the ideal validation tool to demonstrate correlations between the mechanical properties measured using nanoindentation to the corresponding structural information measured using Raman spectroscopy at similar micron (lamellar) length scales.

Figure 26 shows the experimental procedure for generating spherical indentation and Raman spectroscopy maps on the dehydrated and embedded ‘dry’ mouse femora followed in [63]. Detailed investigations were carried out on the endosteal surface of the antero-medial (AM) cortex of the mouse femora. This region was chosen due to the particular pattern of cortical drift in these mice at 16 weeks of age [166, 168] in which they tend to add new bone endosteally along their AM cortex (as illustrated in Fig. 26). Owing to this growth pattern, the chemical composition, and hence the mechanical

properties, are expected to differ between regions of newly formed bone at the surface relative to the older bone matrix intracortically in this region. Thus, in the right panel of Fig. 26 the newest bone is present closest to the endosteal edge, while the bone is more mature as we proceed away from this surface.

However bone in its 'dry' dehydrated/embedded state is far removed from its naturally hydrated *in-vivo* environment, and the preservation and processing steps involved in Ref. [63] can adversely affect the physical and mechanical properties of mineralized tissues. In order to avoid these sample preparation issues a (different) set of mouse femur samples of the same two strains were also tested in their 'wet' hydrated state by the same authors [169]. For the wet samples the femora were kept moist with phosphate-buffered saline (PBS) solution (pH 7.4) mixed with $CaCl_2$ (210 mg of $CaCl_2$ per liter of PBS) at all times during their preparation and testing. The viscoelastic properties of the wet samples were investigated using nanoindentation following a very similar test pattern as shown in Fig. 26 (with the exception of the spectroscopy study which is applicable only on dry samples). While providing complimentary information about the dynamic mechanical behavior of the hydrated bone samples, these tests also serve as a validation tool for the tests on the dry samples.

Representative results on both the 'dry' [63] and 'wet' [169] bone samples are shown in Fig. 27. Figure 27a shows the representative backscattered electron microscopy (BSEM) images of the A/J and B6 femur sections at 14 weeks of age. Figure 27b shows the 2D surface maps of the mineral-to-matrix ratio close to the AM cortex of the dry mouse femora. These maps were generated using Raman spectroscopy in which the different mineral and collagen components in bone can be correlated to different Raman

peaks in the measured spectra [170]. The mineral-to-matrix ratio, which relates to bone mineralization [171], was determined using the phosphate to CH_2 wag peak intensity ratio. Similarly Fig. 27c illustrates the variations in the viscoelastic response (on a different sample set) of the femora in their 'wet' condition across a 2D surface area close to the endosteal edge of the AM cortex. Here the viscoelastic response is measured in terms of the $\tan\delta$ values at a representative frequency of 101 Hz using the nano-DMA® (Dynamic Mechanical Analysis) software in the Hysitron Triboscope, where the linear viscoelastic frequency dependent dynamic response of the material can be ascertained as

$$\tan\delta = \frac{E''}{E'} = \frac{\omega C_S}{k_S} \quad , \qquad (16)$$

Here E' and E'' denote the storage and loss moduli, ω is the frequency of the applied force and k_S and C_S are the sample stiffness and damping coefficients, respectively. The 2D surface maps in Figs. 27b and c are color coded to reflect the values of the mineral-to-matrix ratio and the $\tan\delta$ values, respectively, where a deeper shade represents a higher response.

Figures 27b and c show that the trends from both the dry and wet sample sets are highly complementary to each other. For example, both mouse strains in Fig. 27b show smaller values of the mineral-to-matrix ratio close to the endosteal edge, with the values increasing progressively away from the edge. Correspondingly in Fig. 27c, the highest $\tan\delta$ values across both strains are also found close to the endosteal surface, with the values decreasing as the indenter moves away from the endosteal edge. Since hydrated bone owes its remarkable viscoelasticity to the collagen fibrils in the bone matrix [165, 172], the above trend supports a direct relationship between larger viscoelastic response and lower mineral-to-matrix ratio (a higher collagen content). Thus the decrease in the

values of $\tan\delta$ away from the endosteal edge is indicative of the higher degree of maturity of the bone in this region.

Figure 27 also highlights some important differences in the degree of mineralization between the two mouse strains: not only do the A/J mice appear to reach a higher mineral-to-matrix ratio (and correspondingly lower values of $\tan\delta$) than B6, this increase happens over a much shorter distance from the endosteal edge in A/J than it does in B6. This trend suggests a larger degree of mineralization in the A/J femur than in the B6 at a similar distance into the cortex.

The above results indicate that the differences in the growth patterns between the two mouse strains have not been substantially altered by the dehydration/embedding procedures employed in [63], and thus these structural differences are ideally suited for correlation studies with their local mechanical properties using indentation stress-strain curves. Spherical indents were conducted on the same regions as the Raman spectroscopy measurements on the 'dry' samples as shown schematically in Fig. 27b. The results from the indentation stress-strain curves, namely the Young's modulus from the initial loading segment (E_s) and the indentation yield strength, Y_{ind} (calculated as the indentation stress at 0.2% offset strain) are shown along with their associated Raman measurements in Fig. 28. Note the strong, approximately linear, correlations of both E_s and Y_{ind} with the mineral-to-matrix ratios in Figs. 28a and c. These data suggest that both the local chemical composition (in terms of the mineral-to-matrix ratio) and the local mechanical behavior (E_s and Y_{ind}) of bone follow a similar pattern in the AM cortices of these mouse femora. Thus a lower mineral-to-matrix ratio close to the edge results in a lower Young's modulus and yield behavior at similar locations, and the higher mineralization of the A/J

samples are reflected as higher values of both E_s and Y_{ind} in Figs. 28a and c. The authors also note that these correlations are much weaker when the Young's modulus and hardness values are calculated from the unloading segments of the curve using the calibrated area functions [7, 8] (Figs. 28b and d).

The combined indentation-Raman spectroscopy study also helps us to understand the inter-strain differences between the two mouse strains. It is known that while the A/J femora have a smaller diameter and correspondingly a smaller moment of inertia compared to B6 (see the BSEM images in Fig. 27a), they do not differ in their cortical areas [164, 165]. However, instead of a less structurally efficient structure as one would expect (if the bone compositions were identical across the two mouse strains), the A/J femora are found to possess similar overall stiffness and strength values [165]. This would indicate that the A/J bones have biologically coupled a change in bone quality in order to satisfy the imposed mechanical demands [164].

The results from the indentation and Raman spectroscopy studies described above help validate this hypothesis. These results indicate that the A/J mice appear to have obtained a higher degree of mineralization in their femora as compared to B6, since they consistently show the highest local values of the mineral-to-matrix ratios in the intracortical regions, and correspondingly the highest local values of E_s and Y_{ind}, and lower values of $\tan\delta$. Thus by biologically coupling a change in their bone quality, in terms of a higher mineral-to-matrix ratio, the A/J mouse strain appears to have satisfied the increased mechanical demands imposed by their particular bone morphology. Interestingly, this trade-off between the reduced diameter and an increased mineral content in the A/J mice is not without consequences – at the whole bone level the A/J

femora were also found to have reduced toughness and they fracture in a more brittle manner than the B6 in whole bone bending tests [164, 165]. So while the increased mineral content in A/J femura makes them mechanically robust in terms of stiffness (in that they are similar to B6), they are still weaker with regard to their post-yield behavior.

8. Applications to Vertically Aligned Carbon Nanotube (VACNT) Brushes

Other than bone, indentation stress-strain curves have also been successfully applied to other hierarchical structures. In this section, we discuss the use of these new protocols on a novel hierarchical material system consisting of dense layers of vertically aligned carbon nanotube (VACNT) brushes.

Considerable efforts have been dedicated to exploring the deformation mechanisms of VACNT brushes, in part motivated by their wide range of potential applications in areas such as energy dissipation devices, electrical interconnects, thermal interface materials, micro-electro-mechanical-systems (MEMS) and microelectronics [173-175]. While individual CNTs have been announced as the strongest material known [176] and have shown extremely high strength and Young's modulus in tensile tests on individual tubes [177], much less is known about the VACNT brushes in terms of their mechanical behavior. The hierarchical architecture of the VACNT brushes renders their mechanical response as a complex phenomena occurring across multiple length scales. The collective behavior of these materials thus relies heavily on the properties of the individual CNTs, as well as on the variations in the collective inter-tube interactions and

inherent property gradients of the microstructure, which in turn are dictated by their synthesis techniques [178-180].

Instrumented indentation, although being a common method for studying mechanical properties of films and coatings, has not been used widely for VACNT brushes [181, 182]. This is primarily due to the extremely low density of VACNT brushes (>90% porosity) produced so far, which often result in the CNTs bending away from the indenter under contact loading, making analysis difficult [183]. Additionally while VACNT brushes/films may have micrometer-to-millimeter-sized lateral and vertical dimensions, they are comprised of individual nanotubes with diameters in the nanometer range, which drives their mechanical response to be distinct from monolithic materials. Hence, the accurate estimation of the contact area between the VACNT film and the commonly used sharp pyramidal indenter tip geometries [181, 184, 185], necessary for indentation data analysis, poses a significant challenge. Similarly maintaining parallel contact between the indenter and the sample is a major concern when using flat punch indenters on VANCTs, which tends to obscure their initial buckling response [181, 186-188]. Another complicating factor is the extremely high aspect ratio of the CNTs, which makes them highly susceptible to buckling at very low compressive loads under the indenter tip [189].

In order to mitigate some of these problems, highly dense VACNT brushes made of small-diameter (1-3 nm outer diameter, 1-4 walled) CNTs, produced by high temperature vacuum decomposition of SiC single crystals [190], have been used for analysis using indentation stress-strain curves in [191]. These novel carbide-derived carbon (CDC) VACNT brushes have been shown to have a density close to 0.95 g/cm^3

[190], which is significantly (10 times or more) higher than in catalytic growth of any kind of nanotubes [173, 174, 192] – making them highly amenable to contact loading experiments.

Figure 29a shows a SEM micrograph of the 200nm thick VACNT brush and the VACNT brush – graphite interface. The higher density of these brushes, which makes them ideal for indentation testing, is evident in this image where no apparent porosity is visible. Figures 29b and c show the indentation load-displacement and stress-strain responses respectively for a 1 μm spherical indenter into this VACNT brush. Note in particular how the indentation stress-strain curves enable one to follow the entire evolution of the mechanical response in the VACNT array, from initial elasticity to the initiation of buckling to post-buckling behavior at finite plastic strains. This is visible as three distinct stages during indentation of these VACNT brushes in Fig. 29c: there is an initial linear portion where the indenter elastically compresses the CNT array (see the schematic in the figure), followed by the initiation of buckling at a critical load, and finally a sharp increase in the slope of the curve signaling the influence of the SiC substrate. In addition, the indentation stress-strain curves also allow one to estimate the Young's modulus and the stress at buckling in the indentation experiment. From this figure, the Young's modulus of these 200 nm thick VACNT brushes can be estimated to be ~17 GPa and the critical buckling stress was estimated as ~0.3 GPa at a load of 0.02 mN.

The authors in Ref. [191] also describe how indentation stress-strain curves from different indenter radii can be used on these VACNT brushes to explore the effects of indentation zone sizes and the material defect density on the VACNT buckling stress.

This is shown in Fig. 30 where the indentation response on a much thicker VACNT brush (thickness 1.2-1.4 μm, see Fig. 30a inset) is shown as a function of 3 different indenter radii. In general all three indenter sizes show a similar trend in the VACNT response: an initial elastic behavior (Young's modulus ~18 GPa), followed by a sharp drop at a critical stress corresponding to CNT buckling. Note however that the values of buckling stresses vary significantly between the three different indenters, where indentation with the smaller 1 μm indenter shows the highest buckling stress, followed by the 5 μm indenter, while buckling with the largest 13.5 μm indenter occurs at a significantly lower indentation stress. This point is further illustrated in the table in Fig. 30b, where the average and standard deviation values (of ≥5 tests) of the indentation buckling stress, and the average values of contact radius (a) and indentation zone size (~2.4a; see Eq. (6)) at buckling from these tests for the 3 different indenters are presented.

As seen from the above table, the indentation zone sizes at buckling for the larger 13.5 μm indenter (~3.58 μm) extends well beyond the VACNT brush thickness (1.2-1.4 μm), while only a limited thickness of the VACNT brush (~ 0.39 μm) is exposed to indentation stress for the smaller 1 μm indenter (see schematic in Fig. 29c inset). The corresponding differences in buckling stress are thus largely a consequence of the effective buckling length available in each case; with smaller indenters there is only a smaller buckling length and the material is able to withstand higher buckling stresses.

The table in Fig. 30b also shows larger variations in the values of the buckling stress for the small 1 μm radii indenter compared to the larger indenters. These values seem to indicate that defect density varies from one location to another in one VACNT brush. As seen from the above table, the smaller volume sampled by the 1 μm indenter is

more sensitive to the variation in defect density when different regions of the sample are probed, as indicated by the large spread of the buckling stress values when using this indenter. The larger indenters, on the other hand, encounter a bigger volume, and hence they mostly register a combined VACNT-defect response leading to a lower buckling stress and a smaller spread in the buckling stress.

The above results have been validated by conducting compression tests on VACNT micro-pillars machined using a focused ion bean (FIB) on the same sample. This is shown in Fig. 31 which shows the uniaxial compression data for a ~600 nm diameter VACNT pillar. As seen from this figure, the values measured from indentation and compression tests are complementary to one another. The increase in the Young's modulus values in the micro-pillar compression tests (~30 GPa as compared to ~17-18 GPa in indentation) is due to ion-beam irradiation during the micro-machining process using FIB. This modifies the structure of the outer rim of CNTs in the VACNT pillar, which potentially results in intertube bridging between the densely packed CNTs and hence an increase in their Young's modulus [193].

These numbers suggest that these CDC-VACNT brushes perform significantly better and exhibit considerably higher mechanical properties compared to CVD VACNT turfs; CDC-VACNTs have values of Young's modulus 1-2 orders of magnitude higher [194], and buckling strengths several orders of magnitude higher [181, 189] compared to a CVD VACNT turf – a difference which is explained by the much higher density of the tubes per unit area in the CDC-VACNT resulting in considerably higher mechanical properties. These higher properties are of extreme importance for making selective CNT

membranes for gas or liquid filtration/separation or CNT coatings for tribological applications.

9. Summary and Future Trends

The new protocols described in this review for producing meaningful indentation stress-strain curves have demonstrated tremendous potential for reliably extracting microscale structure-property correlations in a broad range of material systems, especially when combined with appropriate structure characterization techniques (e.g., orientation image mapping (OIM, Raman spectroscopy). It is also seen that these methods can be applied to study mechanical responses of local constituents as well as interfaces. These new experimental tools open up numerous avenues of potential future research. In particular, it is expected that the new protocols and tools described in this review are critical to identifying and understanding the physical origin of the superior properties of certain high-performance composites that exhibit effective properties that exceed by orders of magnitude the properties of their constituents [195]. It is generally believed that the 'mechanical property amplification' is intricately linked to the multi-level hierarchical composite structure present in these material systems [196, 197]. As a specific example, α–β Ti alloys exhibit a very rich class of microstructures (and superior properties compared to either pure α or pure β titanium), although the level of hierarchy in the microstructure and the mechanical property amplification is significantly lower compared to that in the biological polymer-ceramic composites mentioned earlier. But even for these simpler α–β Ti alloys, the establishment of robust physics-based composite theories is at a primitive and premature stage. One of the main hurdles has

been the lack of validated fundamental data on the anisotropic elastic-plastic behavior (including strain hardening) of the α and β phases at the lower length scales (single crystal level and below), and more importantly on the role of the α–β interfaces. The novel protocols described in this review are expected to play a critical role in gaining a better understanding of the local mechanical behavior of the individual microscale constituents and interfaces (both phase boundaries and grain boundaries) present in the material, and in developing high fidelity, multi-scale, physics-based models for new material systems of interest in emerging advanced technologies.

Similarly in biomaterials such as bone, the use of indentation stress-strain curves also have the potential to build a new rigorous framework for study of structure-property linkages, and lead to development of new methods for diagnosis and treatment of a number of bone-related health conditions. In osteoporosis, for example**,** there is reduced mechanical strength and an increased susceptibility to fracture, particularly in anatomical areas such as the spine and the hip. With over 10 million Americans affected by osteoporosis, there are heavy costs associated with this disease in terms of medical expenditures, reduced quality of life and increased mortality risk [198]. Existing techniques for screening patients for fracture risk, such as Dual-Energy X-Ray Absorptiometry (DXA) measures of bone mineral density (BMD), largely reflect bone quantity and are only able to account for 60-70% of the variation in bone strength [199]. Clearly there are additional details of bone quality (tissue and matrix level composition) and geometry (tissue quantity and distribution) that contribute significantly to bone's mechanical competency [151, 200] that BMD cannot measure. New techniques using indentation are currently being developed that can test the mechanical properties of living

tissue like cartilage [201-204], bone and surgical implants [205] with and without [206] arthroscopic surgical control. Similarly, a range of novel techniques also exist for measuring the structural information of bone in its *in-vivo* state such as transcutaneous Raman spectroscopy [207, 208], high-resolution peripheral quantitative computed tomography (HR-pQCT [209]), and micro-magnetic resonance imaging (microMRI [210, 211]). The utility of such methodologies in a clinical environment will be limited unless the precise linkages between the details of bone's internal structure and its effective mechanical response are known. Thus the physical insights into the structure-property relationships in bone obtained using indentation stress-strain curves shown in this review can be very useful, since it would allow us to appropriately interpret the results on a set of controlled samples before venturing into the more complex *in vivo* body environment. Future studies of this nature are expected to help formulate robust metrics of bone quality that can be used by medical practitioners to more effectively assess bone health in their patients and recommend appropriate treatment.

The biggest potential of the indentation techniques described here might actually be in the reliable assessment of the mechanical behavior of modified surfaces (e.g., coatings, irradiated, shot-peened, oxidized, and corroded). Instrumented indentation offers the most practical and cost-effective approach available today for these investigations. Furthermore, as demonstrated in this review, indentation with different indenter sizes can allow estimation of the thickness of the surface modified layers without actually sectioning the samples and studying them in electron microscopes. Future studies are expected to further develop this methodology and demonstrate a much broader range of applications.

It should also be recognized that the methods described here need significant further development and validation. Extending the methods to rigorously account for anisotropic behavior of the sample material (at the indentation length scales) is particularly important for future studies. In a similar vein, it is also important to extend the data analyses protocols to take into account rate effects of deformation (e.g., visco-elasticity, visco-plasticity). It is expected that finite element models of spherical indentation will play an important role in developing these enhancements and modifications to the data analyses procedures described in this work. Additionally, there have been several new developments in the indenters themselves to allow for testing at different temperatures, which can pave the way to extending the protocols described here to study thermo-mechanical response of local constituents and interfaces. Finally, extension of these methods to other indenter shapes can greatly enhance the space of stress fields experienced in the indentation zone, and provide additional insights into the local anisotropy of mechanical response.

The development and utilization of the finite element models of indentation are also key to the successful estimates of properties of constituents and interfaces from the indentation stress-strain curves described in this review. This was evident from the brief discussion presented in this review based on Ref. [44], where a simple isotropic elastic-plastic material constitutive description was employed. However, keeping in mind, the length scales involved in the indentation measurements, it is imperative to develop and validate finite element models of indentation that employ more physics-based constitutive descriptions. It is very likely that the more sophisticated constitutive descriptions will require three-dimensional (3-D) finite element models of the indentation experiment.

However, these are critically needed to successfully estimate reliable and meaningful properties from the indentation stress-strain curves. In a very recent paper [212], this problem was posed as an inverse problem, and a specific strategy was outlined that made extensive use of Fourier representations. This new approach was demonstrated for estimating the single crystal elastic properties from a multitude of indentation and OIM measurements on a polycrystalline sample. Future studies are expected to extend this approach to a number of elastic-plastic properties of interest in the microscale constituents and interfaces prevalent in most advanced hierarchical material systems.

Acknowledgements

Authors acknowledge funding from ARO grant W911NF-10-1-0409. SP gratefully acknowledges funding from the Los Alamos National Laboratory Director's Postdoctoral Fellowship for part of this work and during the writing of this manuscript. This work was performed, in part, at the Center for Integrated Nanotechnologies, an Office of Science User Facility operated for the U.S. Department of Energy (DOE) Office of Science. Los Alamos National Laboratory, an affirmative action equal opportunity employer, is operated by Los Alamos National Security, LLC, for the National Nuclear Security Administration of the U.S. Department of Energy under contract DE-AC52-06NA25396.

References

[1] D. Tabor, The Hardness of Metals, Oxford University Press, 1951.
[2] S.M. Walley, Materials Science and Technology (2012) DOI 10.1179/1743284711Y.0000000127.
[3] A.C. Fischer-Cripps, Nanoindentation, Springer, 2004.

[4] R.W. Armstrong, W.L. Elban, Materials Science and Technology (2012 - focused issue).
[5] K.J. Hemker, W.N. Sharpe Jr, K.H.J. Buschow, W.C. Robert, C.F. Merton, I. Bernard, J.K. Edward, M. Subhash, V. Patrick, Mechanical Testing of Very Small Samples, Encyclopedia of Materials: Science and Technology, Elsevier, Oxford, 2006, pp. 1-6.
[6] J.R. Greer, J.T.M. De Hosson, Progress in Materials Science 56 (2011) 654-724.
[7] W.C. Oliver, G.M. Pharr, Journal of Materials Research 7 (1992) 1564-1580.
[8] W.C. Oliver, G.M. Pharr, Journal of Materials Research 19 (2004) 3-20.
[9] E.G. Mahin, J.G.J. Foss, American Society for Metals -- Transactions 27 (1939) 337-354.
[10] Z. Jeffries, R.S. Archer, The Science of Metals, McGraw-Hill, 1924.
[11] K. Honda, Science Reports of the Tohoku Imperial University 6 (1917) 95-99.
[12] S.R. Kalidindi, S. Pathak, Acta Materialia 56 (2008) 3523-3532.
[13] S. Pathak, J. Shaffer, S.R. Kalidindi, Scripta Materialia 60 (2009) 439-442.
[14] S. Basu, A. Moseson, M.W. Barsoum, Journal of Materials Research 21 (2006) 2628-2637.
[15] J.S. Field, M.V. Swain, Journal of Materials Research 8 (1993) 297-306.
[16] L. Angker, M.V. Swain, Journal of Materials Research 21 (2006) 1893-1905.
[17] H. Hertz, Miscellaneous Papers, MacMillan and Co. Ltd., New York, 1896.
[18] G.M. Pharr, A. Bolshakov, Journal of Materials Research 17 (Oct 2002) 2260-2671.
[19] M.F. Doerner, W.D. Nix, Journal of Materials Research 1 (1986) 601-609.
[20] A.C. Fischer-Cripps, Vacuum 58 (2000) 569-585.
[21] D.M. Ebenstein, L.A. Pruitt, Nano Today 1 (2006) 26-33.
[22] J.A. Brinell, Teknisk Tidskrift 5 (1900) 69.
[23] A. Wahlberg, Iron and Coal Trades Review (1901).
[24] J.A. Brinell, Baumaterialienkunde 5 (1900) 276–280, 294–297, 317–320, 364–367, 392–394, 412–416.
[25] R.L. Smith, G.E. Sandland, Institution of Mechanical Engineers -- Proceedings 1 (1922) 623-641.
[26] E. Meyer, Zeitschrift des Vereines Deutscher Ingenieure 52 (1908) 645-654.
[27] D. Tabor, Proceedings of the Royal Society of London. Series A, Mathematical and Physical Sciences 192 (1948) 247-274.
[28] B.L. Hammond, R.W. Armstrong, Philosophical Magazine Letters 57 (1988) 41-47.
[29] J.S. Field, M.V. Swain, Journal of Materials Research 10 (1995) 101-112.
[30] J.S. Field, M.V. Swain, Carbon 34 (1996) 1357-1366.
[31] K.L. Johnson, Contact Mechanics, Cambridge University Press, Cambridge, 1987.
[32] H.A. Francis, Transactions of the ASME. Series H, Journal of Engineering Materials and Technology 98 (1976) 272-281.
[33] S. Basu, M.W. Barsoum, S.R. Kalidindi, Journal of Applied Physics 99 (2006).
[34] A.G. Zhou, M.W. Barsoum, S. Basu, S.R. Kalidindi, T. El-Raghy, Acta Materialia 54 (2006) 1631-1639.
[35] M.W. Barsoum, A. Murugaiah, S.R. Kalidindi, T. Zhen, Physical Review Letters 92 (2004).
[36] A. Murugaiah, M.W. Barsoum, S.R. Kalidindi, T. Zhen, Journal of Materials Research 19 (2004) 1139-1148.

[37] M.W. Barsoum, A. Murugaiah, S.R. Kalidindi, T. Zhen, Y. Gogotsi, Carbon 42 (2004) 1435-1445.
[38] M.V. Swain, Materials Science & Engineering A: Structural Materials: Properties, Microstructure and Processing 253 (1998) 160-166.
[39] S. Stauss, P. Schwaller, J.L. Bucaille, R. Rabe, L. Rohr, J. Michler, E. Blank, Determining the stress-strain behaviour of small devices by nanoindentation in combination with inverse methods, Proceedings of the 28th International Conference on MNE, vol 67-68, Elsevier, Lugano, Switzerland, 2003, pp. 818-825.
[40] J. Michler, S. Stauss, P. Schwaller, J.-L. Bucaille, E. Felder, EMPA (Swiss Federal Laboratories for Materials Testing and Research) Publication (2002) 6-7.
[41] B. Taljat, T. Zacharia, F. Kosel, International Journal of Solids and Structures 35 (1998) 4411-4426.
[42] M. Beghini, L. Bertini, V. Fontanari, International Journal of Solids and Structures 43 (2006) 2441-2459.
[43] H. Pelletier, Tribology International 39 (2006) 593-606.
[44] B.R. Donohue, A. Ambrus, S.R. Kalidindi, Acta Materialia 60 (2012) 3943-3952.
[45] E.G. Herbert, G.M. Pharr, W.C. Oliver, B.N. Lucas, J.L. Hay, Thin Solid Films 398-399 (2001) 331-335.
[46] A.C. Fischer-Cripps, B.R. Lawn, Acta Materialia 44 (1996) 519-527.
[47] C. Zambaldi, Y. Yang, T.R. Bieler, D. Raabe, Journal of Materials Research 27 (2012) 356-367.
[48] D.K. Patel, H.F. Al-Harbi, S.R. Kalidindi, Acta Materialia 79 (2014) 108-116.
[49] J. Mencik, M.V. Swain, Journal of Materials Research 10 (1995) 1491-1501.
[50] A.C. Fischer-Cripps, Surface and Coatings Technology 200 (2006) 4153-4165.
[51] J. Deuschle, S. Enders, E. Arzt, Journal of Materials Research 22 (2007) 3107-3119.
[52] Y.Y. Lim, M.M. Chaudhri, Mechanics of Materials 38 (2006) 1213-1228.
[53] Y. Arai, Y.H. Liang, K. Ozasa, M. Ohashi, E. Tsuchida, Physica E 36 (2007) 1-11.
[54] T. Chudoba, M. Griepentrog, A. Duck, D. Schneider, F. Richter, Journal of Materials Research 19 (2004) 301-314.
[55] T. Chudoba, N. Schwarzer, F. Richter, Surface and Coatings Technology 127 (2000) 9-17.
[56] V. Linss, N. Schwarzer, T. Chudoba, M. Karniychuk, F. Richter, Surface and Coatings Technology 195 (2004) 287-297.
[57] F. Richter, M. Herrmann, F. Molnar, T. Chudoba, N. Schwarzer, M. Keunecke, K. Bewilogua, X.W. Zhang, H.-G. Boyen, P. Ziemann, Surface and Coatings Technology 201 (2006) 3577-3587.
[58] C. Ullner, Measurement 27 (2000) 43-51.
[59] P. Grau, G. Berg, W. Fraenzel, H. Meinhard, Physica Status Solidi (A) Applied Research 146 (1994) 537-548.
[60] A.J. Moseson, S. Basu, M.W. Barsoum, Journal of Materials Research 23 (2008) 204-209.
[61] A.E.H. Love, J. Math 10 (1939) 161-175.
[62] X. Li, B. Bhushan, Materials Characterization 48 (2002) 11-36.
[63] S. Pathak, S.J. Vachhani, K.J. Jepsen, H.M. Goldman, S.R. Kalidindi, Journal of the Mechanical Behavior of Biomedical Materials (2012) DOI: 10.1016/j.jmbbm.2012.1003.1018.

[64] S. Pathak, J. Michler, K. Wasmer, S.R. Kalidindi, Journal of Materials Science 47 (2012) 815-823.
[65] S. Pathak, D. Stojakovic, R. Doherty, S.R. Kalidindi, Journal of Materials Research - Focus Issue on Indentation Methods in Advanced Materials Research 24 (2009) 1142-1155.
[66] S. Pathak, D. Stojakovic, S.R. Kalidindi, Acta Materialia 57 (2009) 3020-3028.
[67] S.R. Kalidindi, C.A. Bronkhorst, L. Anand, Journal of the Mechanics and Physics of Solids 40 (1992) 537-569.
[68] M. Knezevic, S.R. Kalidindi, Computational Materials Science 39 (2007) 643-648.
[69] D.T. Fullwood, S.R. Niezgoda, B.L. Adams, S.R. Kalidindi, Progress in Materials Science 55 (2010) 477-562.
[70] G. Proust, S.R. Kalidindi, Journal of the Mechanics and Physics of Solids 54 (2006) 1744-1762.
[71] S. Enders, N. Barbakadse, S.N. Gorb, E. Arzt, Journal of Materials Research 19 (2004) 880-887.
[72] J.Y. Rho, P. Zioupos, J.D. Currey, G.M. Pharr, Journal of Biomechanics 35 (2002) 189-198.
[73] C.A. Schuh, Materials Today 9 (2006) 32-40.
[74] T.H. Courtney, Mechanical Behavior of Materials McGraw-Hill Science/Engineering/Math, 1999.
[75] N. Gane, F.P. Bowden, Journal of Applied Physics 39 (1968) 1432-1435.
[76] W.W. Gerberich, J.C. Nelson, E.T. Lilleodden, P. Anderson, J.T. Wyrobek, Acta Materialia 44 (1996) 3585-3598.
[77] W.W. Gerberich, S. Venkataraman, J. Nelson, H. Huang, E. Lilleodden, W. Bonin, Yield point phenomena and dislocation velocities underneath indentations into BCC crystals, Mater. Res. Soc, Boston, MA, USA, 1995, pp. 629-644.
[78] W.W. Gerberich, S.K. Venkataraman, H. Huang, S.E. Harvey, D.L. Kohlstedt, Acta Metallurgica et Materialia 43 (1995) 1569.
[79] A.E. Giannakopoulos, S. Suresh, Scripta Materialia 40 (1999) 1191-1198.
[80] A. Gouldstone, H.J. Koh, K.Y. Zeng, A.E. Giannakopoulos, S. Suresh, Acta Materialia 48 (2000) 2277-2295.
[81] S. Suresh, T.G. Nieh, B.W. Choi, Scripta Materialia 41 (1999) 951-957.
[82] R.C. Thomas, J.E. Houston, T.A. Michalske, R.M. Crooks, Science 259 (1993) 1883.
[83] S.A. Syed Asif, J.B. Pethica, Philosophical Magazine A (Physics of Condensed Matter: Structure, Defects and Mechanical Properties) 76 (1997) 1105-1118.
[84] R.D. Doherty, Scripta Materialia 49 (2003) 1219-1222.
[85] T. Eliash, M. Kazakevich, V.N. Semenov, E. Rabkin, Acta Materialia 56 (2008) 5640-5652.
[86] T. Ohmura, K. Tsuzaki, Journal of Physics D: Applied Physics 41 (2008) 074015 (074016 pp.).
[87] N. Gane, F.P. Bowden, Journal of Applied Physics 39 (1968) 432-435.
[88] A. Gouldstone, K.J. Van Vliet, S. Suresh, Nature 411 (2001) 656-656.
[89] Y. Wang, D. Raabe, C. Kluber, F. Roters, Acta Materialia 52 (2004) 2229-2238.
[90] M.J. Cordill, N.R. Moody, W.W. Gerberich, Journal of Materials Research 23 (2008) 1604-1613.

[91] G.M. Pharr, J.H. Strader, W.C. Oliver, Journal of Materials Research 24 (2009) 653-666.
[92] M.J. Cordill, M.S. Lund, J. Parker, C. Leighton, A.K. Nair, D. Farkas, N.R. Moody, W.W. Gerberich, International Journal of Plasticity 25 (2009) 2045-2058.
[93] M.J. Cordill, N.R. Moody, W.W. Gerberich, International Journal of Plasticity 25 (2009) 281-301.
[94] K. Durst, O. Franke, A. Boehner, M. Goeken, Acta Materialia 55 (2007) 6825-6833.
[95] J.G. Swadener, E.P. George, G.M. Pharr, Journal of the Mechanics and Physics of Solids 50 (2002) 681-694.
[96] G. Feng, W.D. Nix, Scripta Materialia 51 (2004) 599-603.
[97] M.R. VanLandingham, N.K. Chang, P.L. Drzal, C.C. White, S.H. Chang, Journal of Polymer Science Part B-Polymer Physics 43 (2005) 1794-1811.
[98] J. Mencik, G. Rauchs, J. Bardon, A. Riche, Journal of Materials Research 20 (2005) 2660-2669.
[99] S.J. Vachhani, R.D. Doherty, S.R. Kalidindi, Acta Materialia 61 (2013) 3744-3751.
[100] B.L. Adams, Ultramicroscopy 67 (1997) 11-17.
[101] B.L. Adams, S.I. Wright, K. Kunze, Metallurgical Transactions A 24A (1993) 819-831.
[102] D. Dingley, Journal of Microscopy 213 (2004) 214-224.
[103] G. Proust, S.R. Kalidindi, TMS Letters (The Minerals, Metals and Materials Society) 7 (2004) 151.
[104] J.J. Vlassak, W.D. Nix, Philosophical Magazine A (Physics of Condensed Matter, Defects and Mechanical Properties) 67 (1993) 1045-1056.
[105] J.J. Vlassak, W.D. Nix, Journal of the Mechanics and Physics of Solids 42 (1994) 1223-1245.
[106] Z. Hashin, S. Shtrikman, Journal of the Mechanics and Physics of Solids 10 (1962) 343-352.
[107] H. Bunge, Texture Analysis in Materials Science, London, 1982.
[108] S.J. Vachhani, S.R. Kalidindi, In review (2015).
[109] S. Panchanadeeswaran, R.D. Doherty, R. Becker, Acta Materialia 44 (1996) 1233-1262.
[110] S.R. Kalidindi, A. Bhattacharya, R. Doherty, Proceedings of the Royal Society of London: Mathematical, Physical and Engineering Sciences. 460 (2004) 1935 - 1956
[111] A. Bhattacharyya, E. El-Danaf, S.R. Kalidindi, R.D. Doherty, International Journal of Plasticity 17 (2001) 861-883.
[112] S.R. Kalidindi, A. Bhattacharyya, R.D. Doherty, Advanced Materials 15 (2003) 1345-+.
[113] D. Stojakovic, Microstructure Evolution in Deformed and Recrystallized Electrical Steel, Department of Materials Science and Engineering, Doctor of Philosophy, Drexel University, Philadelphia, PA, 2008.
[114] E.O. Hall, Proceedings of the Physical Society. Section B 64 (1951) 747-753.
[115] N.J. Petch, Iron and Steel Institute -- Journal 174 (1953) 25-28.
[116] M. Goken, M. Kempf, M. Bordenet, H. Vehoff, Surface and Interface Analysis 27 (1999) 302-306.
[117] Y.-H. Lee, D. Kwon, Scripta Materialia 49 (2003) 459-465.

[118] T. Ohmura, A.M. Minor, E.A. Stach, J.W. Morris, Jr., Journal of Materials Research 19 (2004) 3626-3632.
[119] T. Ohmura, K. Tsuzaki, Journal of Materials Science 42 (2007) 1728-1732.
[120] T. Ohmura, K. Tsuzaki, Y. Fuxing, Materials Transactions 46 (2005) 2026-2029.
[121] W.A. Soer, K.E. Aifantis, J.T.M. De Hosson, Acta Materialia 53 (2005) 4665-4676.
[122] W.A. Soer, J.T.M. De Hosson, Materials Letters 59 (2005) 3192-3195.
[123] Y.M. Soifer, A. Verdyan, M. Kazakevich, E. Rabkin, Scripta Materialia 47 (2002) 799-804.
[124] P.C. Wo, A.H.W. Ngan, Journal of Materials Research 19 (2004) 189-201.
[125] M.G. Wang, A.H.W. Ngan, Journal of Materials Research 19 (2004) 2478-2486.
[126] S.R. Kalidindi, S.J. Vachhani, Current Opinion in Solid State and Materials Science 18 (2014) 196-204.
[127] J. Wheeler, J. Curran, S. Shrestha, Surface and Coatings Technology 207 (2012) 480-488.
[128] R.S. Nelson, D.J. Mazey, J.A. Hudson, Journal of Nuclear Materials 37 (1970) 1-12.
[129] G.S. Was, J.T. Busby, T. Allen, E.A. Kenik, A. Jensson, S.M. Bruemmer, J. Gan, A.D. Edwards, P.M. Scott, P.L. Andreson, Journal of Nuclear Materials 300 (2002) 198-216.
[130] S.J. Zinkle, A. Möslang, Fusion Engineering and Design 88 (2013) 472-482.
[131] P. Hosemann, J.G. Swadener, D. Kiener, G.S. Was, S.A. Maloy, N. Li, Journal of Nuclear Materials 375 (2008) 135-143.
[132] D. Kiener, P. Hosemann, S.A. Maloy, A.M. Minor, Nature Materials 10 (2011) 608-613.
[133] P. Landau, Q. Guo, K. Hattar, J.R. Greer, Advanced Functional Materials 23 (2013) 1281-1288.
[134] N. Li, N.A. Mara, Y.Q. Wang, M. Nastasi, A. Misra, Scripta Materialia 64 (2011) 974-977.
[135] Q.M. Wei, N. Li, N. Mara, M. Nastasi, A. Misra, Acta Materialia 59 (2011) 6331-6340.
[136] P. Hosemann, D. Kiener, Y. Wang, S.A. Maloy, Journal of Nuclear Materials 425 (2012) 136-139.
[137] P. Hosemann, C. Vieh, R.R. Greco, S. Kabra, J.A. Valdez, M.J. Cappiello, S.A. Maloy, Journal of Nuclear Materials 389 (2009) 239-247.
[138] J.T. Busby, M.C. Hash, G.S. Was, Journal of Nuclear Materials 336 (2005) 267-278.
[139] S. Pathak, S.R. Kalidindi, Y. Wang, R. Doerner, N. Mara, submitted (2014).
[140] M. Victoria, N. Baluc, C. Bailat, Y. Dai, M.I. Luppo, R. Schaublin, B.N. Singh, Journal of Nuclear Materials 276 (2000) 114-122.
[141] M. Miyamoto, D. Nishijima, M.J. Baldwin, R.P. Doerner, Y. Ueda, K. Yasunaga, N. Yoshida, K. Ono, Journal of Nuclear Materials 415 (2011) S657-S660.
[142] B.N. Singh, A.J.E. Foreman, H. Trinkaus, Journal of Nuclear Materials 249 (1997) 103-115.
[143] A. Patra, D.L. McDowell, Journal of the Mechanics and Physics of Solids (2014 (in review)).

[144] X.Y. Liu, R.G. Hoagland, M.J. Demkowicz, J. Wang, M. Nastasi, A. Misra, J.P. Hirth, Understanding of Interface Structures, Defects, and Mechanical Properties at General FCC-BCC Interfaces using "Tunable" Potentials, 2011, p. 326-327.
[145] D.A. Rigney, X.Y. Fu, J.E. Hammerberg, B.L. Holian, M.L. Falk, Scripta Materialia 49 (2003) 977-983.
[146] S. Suresh, Science 292 (2001) 2447-2451.
[147] A.J. Markworth, K.S. Ramesh, W.P. Parks, Journal of Materials Science 30 (1995) 2183-2193.
[148] R. Rabe, J.M. Breguet, P. Schwaller, S. Stauss, F.J. Haug, J. Patscheider, J. Michler, Thin Solid Films 469–470 (2004) 206–213
[149] S. Pathak, S.R. Kalidindi, B. Moser, C. Klemenz, N. Orlovskaya, Journal of the European Ceramic Society 28 (2008) 2039-2047.
[150] C.J. Hernandez, T.M. Keaveny, Bone (2006).
[151] C.H. Turner, J Musculoskelet Neuronal Interact 2 (2002) 527-528.
[152] S. Weiner, W. Traub, Faseb J 6 (1992) 879-885.
[153] J.D. Currey, Journal of Biomechanics 36 (2003) 1487-1495.
[154] J. Burket, S. Gourion-Arsiquaud, L.M. Havill, S.P. Baker, A.L. Boskey, M.C.H. van der Meulen, J Biomech 44 (2011) 277-284.
[155] E. Donnelly, A.L. Boskey, S.P. Baker, M.C.H. van der Meulen, Journal of Biomedical Materials Research - Part A 92 (2010) 1048-1056.
[156] P. Roschger, E.P. Paschalis, P. Fratzl, K. Klaushofer, Bone 42 (2008) 456-466.
[157] R.M.D. Zebaze, A.C. Jones, M.G. Pandy, M.A. Knackstedt, E. Seeman, Bone 48 (2011) 1246-1251.
[158] X. Bi, C.A. Patil, C.C. Lynch, G.M. Pharr, A. Mahadevan-Jansen, J.S. Nyman, J Biomech 44 (2011) 297-303.
[159] Y. Jiao, H. Chiu, Z. Fan, F. Jiao, E.C. Eckstein, W.G. Beamer, W. Gu, Calcif Tissue Int 80 (2007) 383-390.
[160] L.M. Miller, W. Little, A. Schirmer, F. Sheik, B. Busa, S. Judex, J Bone Miner Res 22 (2007) 1037-1045.
[161] Z. Fan, P.A. Smith, G.F. Harris, F. Rauch, R. Bajorunaite, Connect Tissue Res 48 (2007) 70-75.
[162] Y. Bala, B. Depalle, D. Farlay, T. Douillard, S. Meille, H. Follet, R. Chapurlat, J. Chevalier, G. Boivin, J Bone Miner Res (2011) doi: 10.1002/jbmr.1501.
[163] S. Gourion-Arsiquaud, J.C. Burket, L.M. Havill, E. DiCarlo, S.B. Doty, R. Mendelsohn, M.C.H. van der Meulen, A.L. Boskey, J Bone Miner Res 24 (2009) 1271-1281.
[164] K.J. Jepsen, O.J. Akkus, R.J. Majeska, J.H. Nadeau, Mamm Genome 14 (2003) 97-104.
[165] K.J. Jepsen, D.E. Pennington, Y.L. Lee, M. Warman, J. Nadeau, Journal of bone and mineral research 16 (2001) 1854-1862.
[166] C. Price, B.C. Herman, T. Lufkin, H.M. Goldman, K.J. Jepsen, J Bone Miner Res 20 (2005) 1983-1991.
[167] S.M. Tommasini, T.G. Morgan, M. van der Meulen, K.J. Jepsen, J Bone Miner Res 20 (2005) 817-827.
[168] W.G. Beamer, L.R. Donahue, C.J. Rosen, D.J. Baylink, Bone 18 (1996) 397-403.

[169] S. Pathak, J. Gregory Swadener, S.R. Kalidindi, H.-W. Courtland, K.J. Jepsen, H.M. Goldman, Journal of the Mechanical Behavior of Biomedical Materials 4 (2011) 34-43.
[170] J.A. Timlin, A. Carden, M.D. Morris, Applied Spectroscopy 53 (1999) 1429-1435.
[171] A.L. Boskey, N. Pleshko, S.B. Doty, R. Mendelsohn, Cells and Materials 2 (1992) 209-220.
[172] M. Fois, A. Lamure, M.J. Fauran, C. Lacabanne, Journal of Applied Polymer Science 79 (2001) 2527-2533.
[173] A.Y. Cao, P.L. Dickrell, W.G. Sawyer, M.N. Ghasemi-Nejhad, P.M. Ajayan, Science 310 (2005) 1307-1310.
[174] S. Pathak, E.J. Lim, P. Pour Shahid Saeed Abadi, S. Graham, B.A. Cola, J.R. Greer, ACS Nano 6 (2012) 2189-2197.
[175] J. Suhr, L. Ci, P. Victor, P.M. Ajayan, Fatigue characteristics of carbon nanotube blocks under compression, Behavior and Mechanics of Multifunctional and Composite Materials 2008, March 10, 2008 - March 13, 2008, vol 6929, SPIE, San Diego, CA, United states, 2008, p. The International Society for Optical Engineering (SPIE); American Society of Mechanical Engineers.
[176] M.M.J. Treacy, T.W. Ebbesen, J.M. Gibson, Nature 381 (1996) 678-680.
[177] Y. Min-Feng, O. Lourie, M.J. Dyer, K. Moloni, T.F. Kelly, R.S. Ruoff, Science 287 (2000) 637-640.
[178] M. Kumar, Y. Ando, Journal of Nanoscience and Nanotechnology 10 (2010) 3739-3758.
[179] S.B. Hutchens, L.J. Hall, J.R. Greer, Advanced Functional Materials 20 (2010) 2338-2346.
[180] S.B. Hutchens, A. Needleman, J.R. Greer, Journal of the Mechanics and Physics of Solids 59 (2011) 2227-2237.
[181] J.F. Waters, P.R. Guduru, M. Jouzi, J.M. Xu, T. Hanlon, S. Suresh, Appl. Phys. Lett. 87 (2005) 103109-103101-103103.
[182] C.P. Deck, J. Flowers, G.S.B. McKee, K. Vecchio, Journal of Applied Physics 101 (2007) 23512-23511-23519.
[183] H.J. Qi, K.B.K. Teo, K.K.S. Lau, M.C. Boyce, W.I. Milne, J. Robertson, K.K. Gleason, Journal of the Mechanics and Physics of Solids 51 (2003) 2213-2237.
[184] A. Qiu, D.F. Bahr, A.A. Zbib, A. Bellou, S.D. Mesarovic, D. McClain, W. Hudson, J. Jiao, D. Kiener, M.J. Cordill, Carbon 49 (2011) 1430-1438.
[185] S.D. Mesarovic, C.M. McCarter, D.F. Bahr, H. Radhakrishnan, R.F. Richards, C.D. Richards, D. McClain, J. Jiao, Scripta Materialia 56 (2007) 157-160.
[186] M.R. Maschmann, Z. Qiuhong, D. Feng, D. Liming, J. Baur, Carbon 49 (2011) 386-397.
[187] P.D. Bradford, X. Wang, H. Zhao, Y.T. Zhu, Carbon 49 (2011) 2834-2841.
[188] P. Pour Shahid Saeed Abadi, S. Hutchens, J.H. Taphouse, J.R. Greer, B.A. Cola, S. Graham, Nanoscale (2012) (accepted).
[189] J.F. Waters, L. Riester, M. Jouzi, P.R. Guduru, J.M. Xu, Appl. Phys. Lett. 85 (2004) 1787-1789.
[190] Z.G. Cambaz, G. Yushin, S. Osswald, V. Mochalin, Y. Gogotsi, Carbon 46 (2008) 841-849.

[191] S. Pathak, Z.G. Cambaz, S.R. Kalidindi, J.G. Swadener, Y. Gogotsi, Carbon 47 (2009) 1969-1976.
[192] J. Suhr, P. Victor, L.C.S. Sreekala, X. Zhang, O. Nalamasu, P.M. Ajayan, Nature Nanotechnology 2 (2007) 417-421.
[193] A. Kis, G. Csanyi, J.P. Salvetat, T.-N. Lee, E. Couteau, A.J. Kulik, W. Benoit, J. Brugger, L. Forro, Nature Materials 3 (2004) 153-157.
[194] S.D. Mesarovic, C.M. McCarter, D.F. Bahr, H. Radhakrishnan, R.F. Richards, S.D. Richards, D. McClain, J. Jiao, Scripta Materialia 56 (2007) 157-160.
[195] U.G.K. Wegst, M.F. Ashby, Philosophical Magazine 84 (2004) 2167-2181.
[196] H.M. Yao, H.J. Gao, Int. J. Solids Struct. 44 (2007) 8177-8193.
[197] C. Ortiz, M.C. Boyce, Science 319 (2008) 1053-1054.
[198] America's bone health: The state of osteoporosis and low bone mass in our nation, National Osteoporosis Foundation, Washington (DC), 2002.
[199] P. Ammann, R. Rizzoli, Osteoporos Int 14 Suppl 3 (2003) S13-18.
[200] D.B. Burr, J Musculoskelet Neuronal Interact 2 (2002) 525-526.
[201] T. Lyyra, J. Jurvelin, P. Pitkanen, U. Vaatainen, I. Kiviranta, Med Eng Phys 17 (1995) 395-399.
[202] J. Toyras, T. Lyyra-Laitinen, M. Niinimaki, R. Lindgren, M.T. Nieminen, I. Kiviranta, J.S. Jurvelin, J Biomech 34 (2001) 251-256.
[203] P.A. Brama, A. Barneveld, D. Karssenberg, G.P. Van Kampen, P.R. van Weeren, J Vet Med A Physiol Pathol Clin Med 48 (2001) 213-221.
[204] A.I. Vasara, J.S. Jurvelin, L. Peterson, I. Kiviranta, Am J Sports Med 33 (2005) 408-414.
[205] I. Hvid, F. Linde, Penetration testing of bone using an osteopenetrometer, in: Y.H. An, R.A. Draughn (Eds.), Mechanical Testing of Bone and Bone-Implant Interface, 1999.
[206] P.K. Hansma, P.J. Turner, G.E. Fantner, Review of Scientific Instruments 77 (2006) 075105-075106.
[207] P. Matousek, E.R. Draper, A.E. Goodship, I.P. Clark, K.L. Ronayne, A.W. Parker, Appl Spectrosc 60 (2006) 758-763.
[208] E.R. Draper, M.D. Morris, N.P. Camacho, P. Matousek, M. Towrie, A.W. Parker, A.E. Goodship, J Bone Miner Res 20 (2005) 1968-1972.
[209] S. Boutroy, M.L. Bouxsein, F. Munoz, P.D. Delmas, J Clin Endocrinol Metab 90 (2005) 6508-6515.
[210] F.W. Wehrli, L. Hilaire, M. Fernandez-Seara, B.R. Gomberg, H.K. Song, B. Zemel, L. Loh, P.J. Snyder, J Bone Miner Res 17 (2002) 2265-2273.
[211] F.W. Wehrli, P.K. Saha, B.R. Gomberg, H.K. Song, P.J. Snyder, M. Benito, A. Wright, R. Weening, Top Magn Reson Imaging 13 (2002) 335-355.
[212] D.K. Patel, H.F. Al-Harbi, S.R. Kalidindi, Acta Materialia 79 (2014) 108-116.
[213] L.H. He, N. Fujisawa, M.V. Swain, Biomaterials 27 (2006) 4388-4398.
[214] S. Pathak, J. Riesterer, S.R. Kalidindi, J. Michler, submitted (2014).

Figure captions

Figure 1. Various mechanical testing methods for micron to sub-micron length samples.

Figure 2. (a) Schematic of the indentation zone in spherical indentation. **(b)** Schematic of a typical measured spherical indentation load-displacement curve with the initial and final contact geometries.

Figure 3. History of indentation stress-strain curves. **(a)** The concept of indentation stress-strain curves was first introduced by Tabor [1]. His models provided a direct correlation between hardness measurements and uniaxial tests, as shown here for ball indentation of mild steel and annealed copper compared with uniaxial compression (solid curves). Here indentation strain is measured as a/R_i, or d/D where a, d and R_i, D are the radii and diameters of the residual imprint and the ball indenters respectively [27]. **(b)** This process was automated by Field and Swain using multiple partial unloads and the indenter geometry to estimate a [30], and further extended in the work from **(c)** Barsoum's research group [14]. Most research groups have used a/Ri as a measure of indentation strain or some variations of the same such as **(d)** the use of $\tan\theta$ as indentation strain where $\sin\theta = a/Ri$ [213].

Figure 4. (a) Strain and contact radius definitions used to label curves in Figs. 4b, 5, and 6. **(b)** Indentation stress-strain curves based on different definitions of contact radius and indentation strain, generated from load-displacement data predicted by finite element models [44].

Figure 5. Map of the logarithmic strain component along the indentation direction (LE22) in the indentation zone close to the indentation yield. The model axis of symmetry is the left edge of the figure [44].

Figure 6. A comparison of the extracted indentation stress-strain curves for **(a)** tungsten and **(b)** aluminum, using the two different definitions of indentation strain. The definition of the indentation strain (= h_t */2.4a,* Protocol A in Fig. 4) produces significantly better indentation stress-strain curves with correct values of indentation modulus during both loading and unloading.

Figure 7. (a) The identification of the effective zero-point in the dataset measured on a vibro-polished Fe-3%Si steel sample indented with a 13.5 μm radius spherical indenter [12]. The measured **(b)** load-displacement curve and the extracted **(c)** indentation stress-strain curves for Fe-3%Si steel using two different estimates of the zero-point. The inset in (b) shows the two different estimates of the zero-point: C_1 - zero point given by the machine and C_2 - effective zero point determined using [12].

Figure 8. Comparison between the effective zero-points identified by the CSM technique (Eq. 7) and the non-CSM technique (Eq. 8) for tungsten using a 1.4 μm spherical indenter. The residual error is obtained from regression analyses as measure of the degree of fit to Eq. 8.

Figure 9. (a) Schematic of the procedure involved in establishing the contact radius, a, at different load levels. The unloading segment at each of these load levels is fitted to Eq. 9 to estimate h_r and k. R_{eff} and a can then be calculated using Eqs. 8 and 10. **(b)** Values of R_{eff} computed at different indentation depths which differ significantly between the softer aluminum and the harder tungsten sample. The values for R_{eff} are also

significantly larger than R_i (= 20μm) for both samples. Inset: Expanded view for the tungsten sample.

Figure 10. Comparison between the indentation stress-strain curves obtained using the CSM method (Section 5.1) and the non-CSM method (Section 5.2) on **(a)** aluminum and **(b)** tungsten samples with the 1.4 and 20 μm radii indenters. The insets show expanded views of the indentation stress-strain curves for the larger 20 μm indenter.

Figure 11. Comparison between the indentation stress-strain responses in **(a)** mechanically polished and electro-polished surfaces and **(b)** electro-polished and vibro-polished surfaces of annealed W. These tests were carried out using a 13.5 μm spherical indenter [65].

Figure 12. (a) Pop-ins in nanoindentation are generally revealed as sudden excursions in depth and strain (in a load controlled experiment) and occur most readily in indentation experiments on annealed samples with very small indenter tip radii, such as during indentation on annealed W with a 1 μm radius indenter [65]. **(b)** Their occurrence is more stochastic when using a larger indenter (such as during indentation on as-cast Fe-3%Si with a 13.5 μm radius indenter [65]) and **(c)** pop-ins are almost always absent in tests on cold-worked samples with high dislocation densities. Thus tests on 30% deformed Fe-3%Si steel do not show any pop-in even with a small sized indenter of 1 μm radius [65]. **(d)** Rough mechanical polishing can cause the near-surface dislocation density to increase, thus reducing pop-ins but artificially increasing the yield stress (Y_{ind}) in annealed W [65]. Vibro-polished samples show the ideal combination for measuring

Y_{ind}: suppressing pop-ins in as-cast Fe-3%Si but not adversely affecting the Y_{ind} value [64].

Figure 13. (a) Indentation stress-strain response of a pop-in event in an electropolished tungsten sample using a spherical indenter of 1 μm radius. The pop-in is manifested as a strain burst at constant stress, which is immediately followed by an unloading segment after the pop-in. **(b)** Corresponding measurements of the indentation load, displacement and contact radius (CSM signal) show that the contact radius remains constant during the pop-in but increases rapidly immediately afterwards. Note that the filled-in symbols correspond exactly between (a) and (b), i.e., the same range of data is shown by the filled-in symbols in the two figures. Note also data point marked in gold color, which signifies the end of the regime of rapid increase in the contact radius, and its corresponding location in the indentation stress-strain curve.

Figure 14. (a) Schematic of the sequence of events immediately following a pop-in in spherical nanoindentation. Before pop-in (the curve in gray) both the indenter and the sample surface are highly conforming up to a contact radius of *a*. Upon pop-in, there is a sudden increase in the indentation depth, but no immediate increase in *a*. Rather dislocations traveling (in bursts) along specific crystallographic planes get released along the free surface adjacent to the indenter. This brings the sample surface in closer proximity to the indenter. Thus any further loading causes a large increase in *a*.

(b) Load-displacement response on a near-(001) aluminum surface using a 1 μm indenter showing a test stopped after a single large pop-in event. **(b inset)** 3D and **(c)** surface profiles of the above indent measured using a hybrid AFM-SEM system showing a large step formation along the [110] direction of the indent surface. Note the significant

anisotropy of the residual indent imprint, no such pile-up is visible in the perpendicular $[\bar{1}10]$ direction [214].

Figure 15. (a) Influence of the displacement oscillation on hardness, *H*, measured on Cu (100) using a Berkovich tip. **(b)** Hardnesses derived from corrected *P–h–S* data. Reprinted with permission from [91].

(c) Influence of CSM on the indentation stiffness-displacement response: Raw stiffness-displacement data corresponding to measurements conducted using a 100 μm spherical tip on 20% deformed ultra-high purity aluminum; **(d)** No noticeable changes are seen upon correcting the data using Eqs. 11-13 [99].

(e) Influence of CSM on the Indentation stress-strain curves for tests on 20% deformed ultra-high purity aluminum using a 100 μm spherical tip; **(f)** the corresponding corrected data (using Eqs. 11-13) again shows no discernable change from the original. (Note that for tests with 45Hz – 2nm oscillations, most of the initial elastic segment is lost while correcting for the stiffness signal, and hence the indentation stress-strain curve could not be extracted) [99].

Figure 16. (a) Causes for the change in Y_{ind}. In an as-cast sample of Fe-3%Si steel, the dislocation content is fairly uniform across all the grains. Here Y_{ind} varies from one grain to another mainly due to the differences in the activities of the different slip systems in the different grains and their orientation with the indentation direction. When the metal is 30% deformed, its dislocation content increases and varies both within individual grains and between grains. The Y_{ind} in deformed samples therefore depends on both the grain orientation and the dislocation content at the indentation site.

(b) and **(c)** show the typical load-displacement and their corresponding indentation stress-strain responses respectively for spherical indentations performed on near (111) grains in as-cast and 30% deformed Fe-3%Si steel. The E_{eff}, Y_{ind} and the post-yield characteristics are much better discerned in (c). Only the loading sections are shown for the indentation stress-strain plots. A 13.5 μm radius spherical indenter was used for the tests.

Figure 17. (a) OIM scan and **(b)** inverse pole figure map obtained on a sample of as-cast and polished Fe-3%Si showing a wide range of grain orientations. Surface contour plots for **(c)** β and **(d)** Y_{ind}. The full circles indicate values extracted directly from the measurements [66].

Figure 18. (a) and **(b)** show the inverse pole figure maps and the OIM scans for 30% and 80% deformed Fe-3%Si samples respectively. Indentations were performed in the regions marked by the dotted circles in each of these samples [66]. The table in **(c)** summarizes the values from indentations on the 30% and 80% deformed Fe-3%Si samples. The estimated Y_{ind} values in the annealed condition were calculated from the surface contour plot in Fig. 17d. The measured values of E_{eff} and Y_{ind} in the deformed condition were calculated from the indentation stress-strain curves, as shown in Fig. 16. The values for β were calculated from Eq. (14).

Figure 19. (a) OIM scans of the top surface showing the as-cast microstructure of the columnar Fe-3%Si sample, and microstructure after plane strain compression to true strains of 0.34, 0.81 and 1.21. **(b)** Extracted values of indentation yield strength and changes in critical resolved shear stress after the third deformation stage [113]. **(c)** For high purity polycrystalline Al deformed to 20% by plane strain compression (PSC), a

positive correlation is observed between the Taylor factor of the individual grain orientations and the percentage increase in local slip resistance ($\%\Delta\tau_{CRSS}$) measured from the indentation yield strength values [108].

Figure 20. Indentation-induced deformation in Mo showing the dependence of hardness on the distance from grain boundary for different maximum indentation loads. At loads >10 mN the hardened zone near the grain boundary is masked by the additional local plastic deformation caused by indentation itself. Reprinted with permission from [85].

Figure 21. Measure of E_{eff} and Y_{ind} across a high angle grain boundary between **(a)** Grains 1 and 2 in as-cast Fe-3%Si steel and **(b)** Grains D4 and D5 in 30% deformed Fe-3%Si steel [64].

Figure 22. Comparing the indentation stress-strain responses across the cross-sections of two common electrolytic coating methods - hard anodizing and plasma electrolytic oxidation (PEO) – on a 5052 aluminum alloy at various distances from the substrate interface and within the aluminum substrate [127].

Figure 23. (a) Upon ion-irradiation, the metal surface is modified by a damaged layer, which causes a change in its mechanical response as compared to the bulk of the sample. **(b)** Map of the logarithmic strain component along the indentation direction (LE22) for a spherical indenter in the indentation zone (~2.4*a*, where *a* is the contact radius) close to the indentation yield [44]. Both the contact radius *a*, and hence the volume probed by indentation, can be controlled with a proper choice of indenter radii. This approach is thus ideally suited for measuring any mechanical changes in the material surface layers, such as probing the **(c)** damage caused by He irradiation on a tungsten

sample. **(d)** Table showing indentation depth (*ht*), contact radius (*a*) and indentation zone size (~2.4*a*) at yield for W using 4 different indenter radii.

* For the 1000 μm radius indenter, the response was all elastic up to h~200nm (instrument limit).

Figure 24. Comparing the indentation stress-strain responses between annealed (orange curve) and irradiated (black curve) W grains of near (001) orientation for three different indenter tip radii **(a)** 1 μm, **(b)** 10 μm and **(c)** 100 μm. **(d)** Illustration showing how changes in the indenter size (and the corresponding indentation zone) can be used to systematically probe different length scale effects in radiation damaged samples.

Figure 25. Comparison of (a) indentation vs. (b) compression stress-strain curves between as-cast and 30% deformed Fe-3%Si samples. Both grains #1 and #D4 have a near (100) orientation as shown in Fig. 21. SEM images of the pillars were taken at 70 deg tilt angle after a nominal strain of around 20%.

Figure 26. For indentation testing both the 'dry' and 'wet' mouse femora were sectioned transversely, distal to the third trochanter. During post-natal growth, bone is deposited (double arrows) and resorbed (single arrows) at different sites around these regions of the femoral cortex resulting in a net cortical drift (large arrow). Spherical nanoindents (shown as blue dots in the SEM image) at the antero-medial (AM) cortex thus probe newer bone closer to the endosteal edge (double arrows) while the bone is more mature away from this surface. Three rows of indentations were performed on each sample. For the 'dry' bone samples the region surrounding the indents was then mapped by Raman Spectroscopy (shown by the red grid around the indented region) [63].

Figure 27. (a) Representative BSEM images of A/J and B6 mouse femora. **(b)** 'Dry' samples: representative 2D surface maps of the mineral-to-matrix ratios (defined as the phosphate to CH2 wag peak intensity ratio from Raman spectroscopy measurements) in the 'dry' dehydrated/embedded bone samples across a 40 μm x 70 μm region close to the endosteal edge of the AM cortex. The white circles denote the approximate size and location of the indentation tests in relation to the Raman maps [63]. **(c)** 'Wet' samples: 2D surface maps of tan δ values at a representative mid-range frequency of 101 Hz across a 20 × 70 μm region close to the endosteal edge of the AM cortex in two A/J and B6 samples in the 'wet' hydrated condition [169].

Figure 28. Scatter plots of **(a)** the Young's modulus *Es* estimated from the initial loading segment of the indentation stress-strain curves, **(b)** *Es* estimated from the unloading portion of the load-displacement data, **(c)** indentation yield strength (Y_{ind}) and **(d)** indentation hardness at max load, all as functions of the mineral-to-matrix ratio measured by Raman spectroscopy across two A/J and three B6 samples [63].

Figure 29. (a) SEM micrograph showing the VACNT brush – graphite interface [191]. **(b)** Indentation load-displacement and **(c)** indentation stress-strain response of a 1 μm spherical indenter on the ~200 nm thick CNT brush showing three distinct stages of VACNT indentation. **(c inset)** Schematic illustration of buckling of the CNTs in a dense CNT brush in the indentation zone.

Figure 30. (a) Indentation stress-strain response on 1.3 μm thick VACNT brush as a function of indenter size (radius) showing an initial elastic behavior followed by the buckling instability. The table in **(b)** shows summarized average and standard deviation

(of ≥5 tests) values of indentation buckling stress, contact radius and indentation zone size at buckling for the 3 different indenters used [191].

Figure 31. Uniaxial compression of a CDC-VACNT micro-pillar of diameter ~ 600 nm. Both the loading Young's modulus and buckling strength in compression show good agreement with the indentation results showed earlier. The inset images show the VACNT micro-pillar before and after compression.

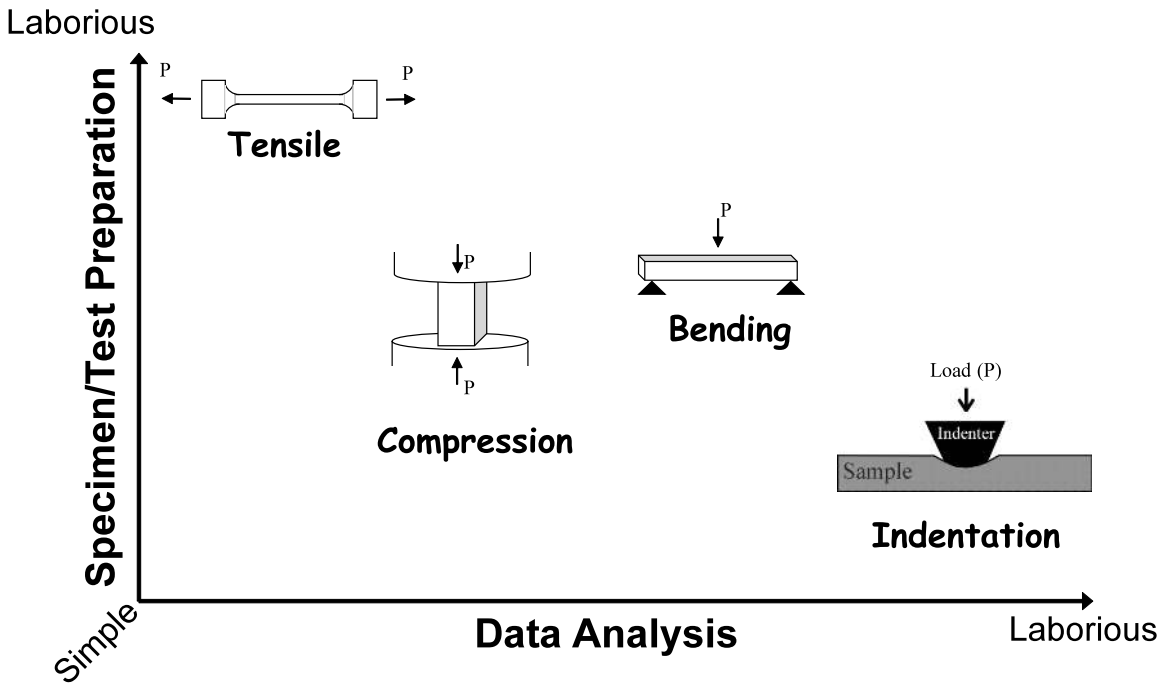

Figure 1. Various mechanical testing methods for micron to sub-micron length samples

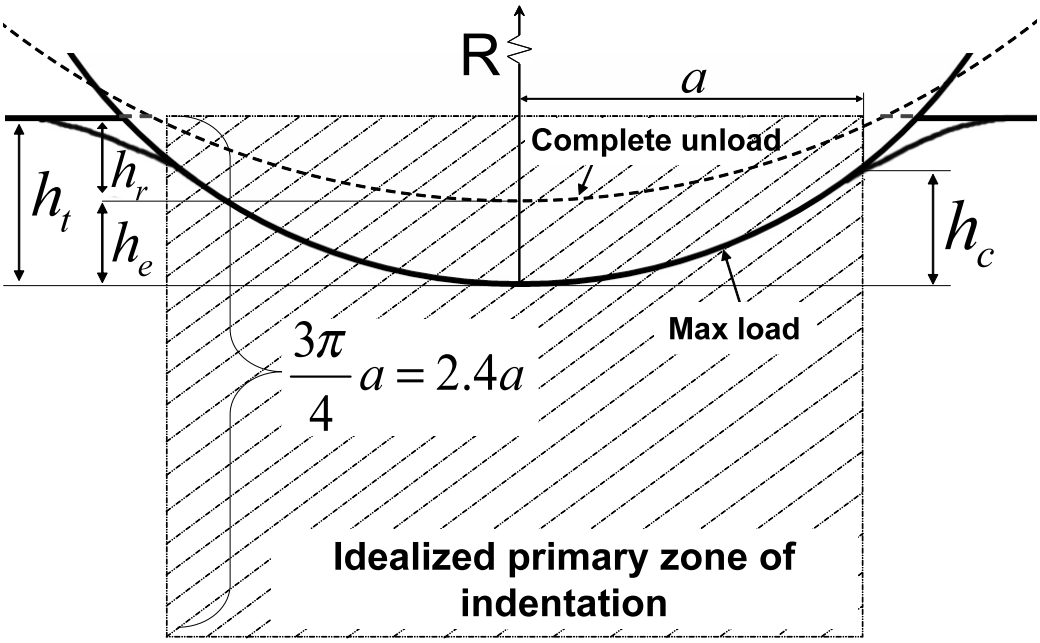

(a)

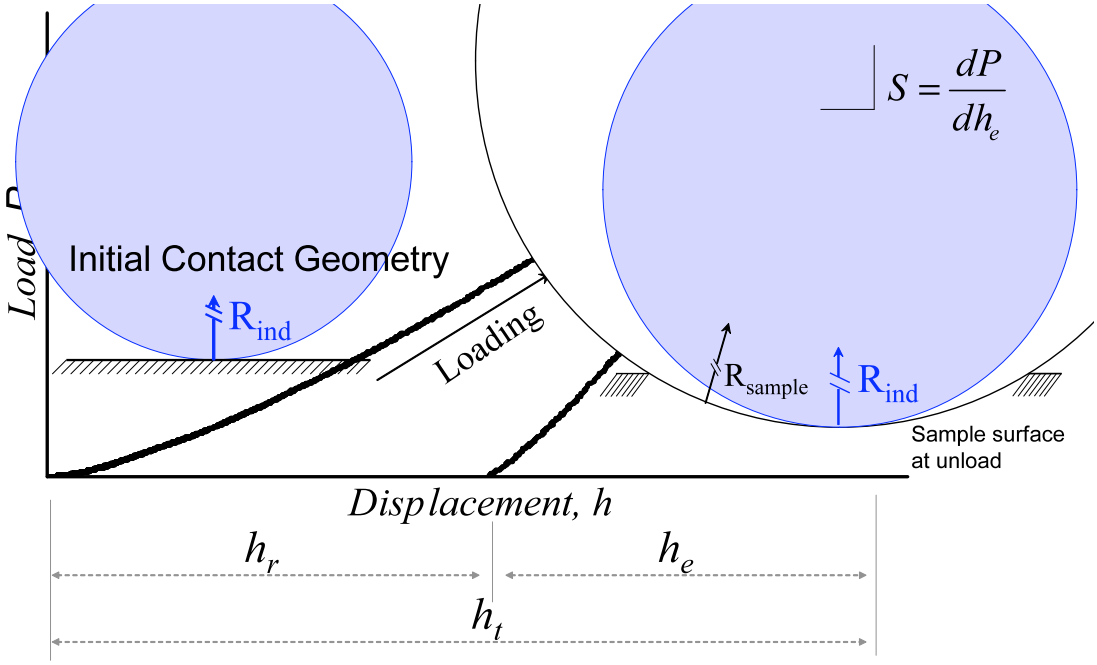

(b)

Figure 2. (a) Schematic of the indentation zone in spherical indentation. **(b)** Schematic of a typical measured spherical indentation load-displacement curve with the initial and final contact geometries.

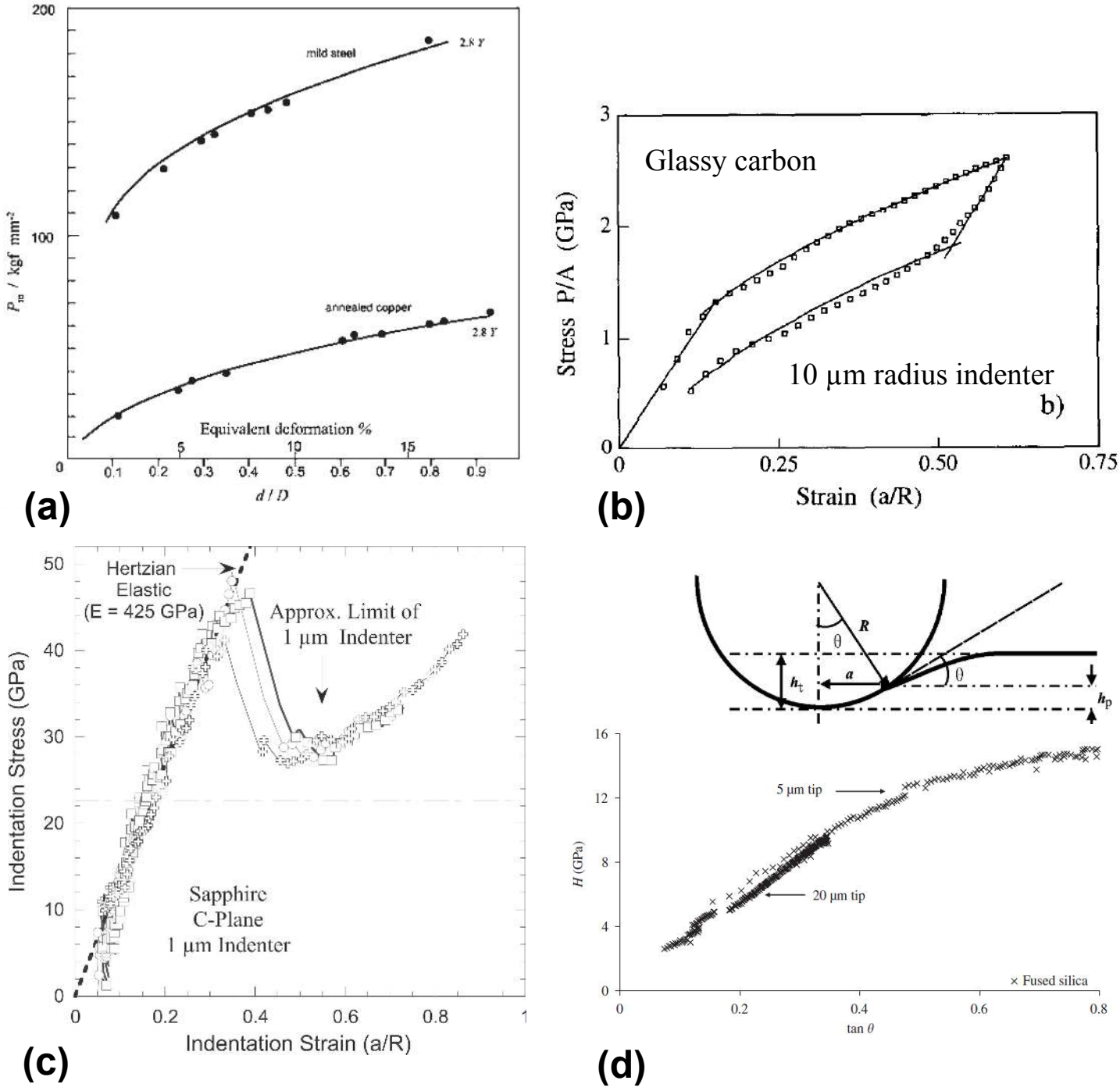

Figure 3. History of indentation stress-strain curves. **(a)** The concept of indentation stress-strain curves was first introduced by Tabor [1]. His models provided a direct correlation between hardness measurements and uniaxial tests, as shown here for ball indentation of mild steel and annealed copper compared with uniaxial compression (solid curves). Here indentation strain is measured as a/R_i, or d/D where a, d and R_i, D are the radii and diameters of the residual imprint and the ball indenters respectively [27]. **(b)** This process was automated by Field and Swain using multiple partial unloads and the indenter geometry to estimate a [30], and further extended in the work from **(c)** Barsoum's research group [14]. Most research groups have used a/R_i as a measure of indentation strain or some variations of the same such as **(d)** the use of $tan\ \theta$ as indentation strain where $sin\ \theta = a/R_i$ [213].

(a)

ε \ a	$\left(\frac{3PR^*}{4E^*}\right)^{1/3}$	$\sqrt{2h_cR_i - h_c^2}$
$4h_t/3\pi a$	A	B
$4a/3\pi R_i$	D	C

(b)

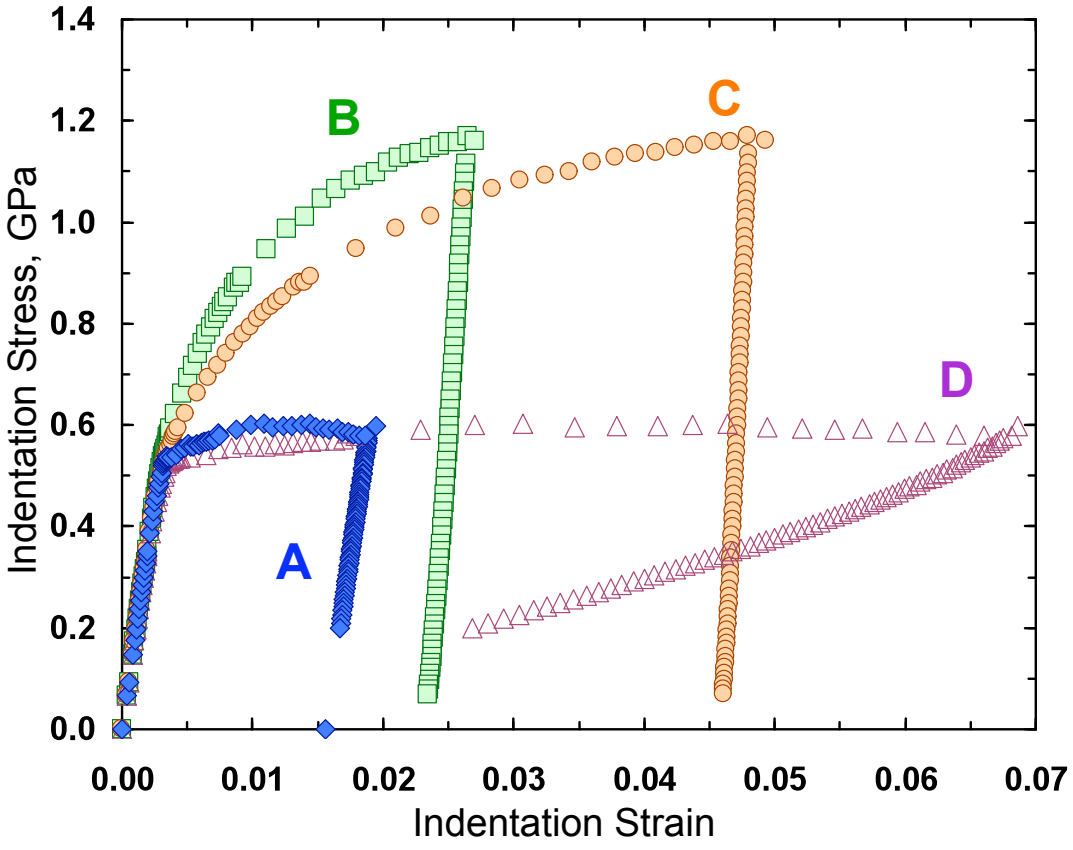

Figure 4. (a) Strain and contact radius definitions used to label curves in Figs. 4b, 5, and 6.
(b) Indentation stress-strain curves based on different definitions of contact radius and indentation strain, generated from load-displacement data predicted by finite element models [44].

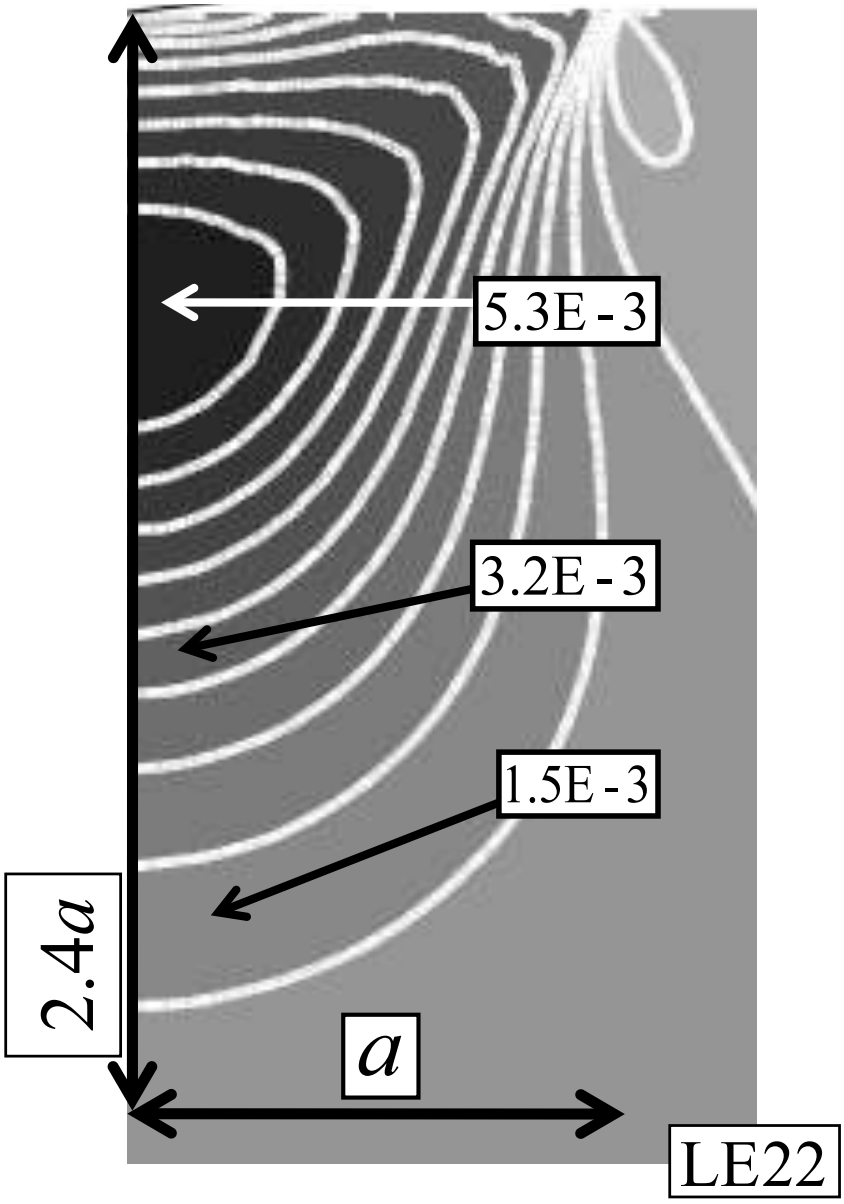

Figure 5. Map of the logarithmic strain component along the indentation direction (LE22) in the indentation zone close to the indentation yield. The model axis of symmetry is the left edge of the figure [44].

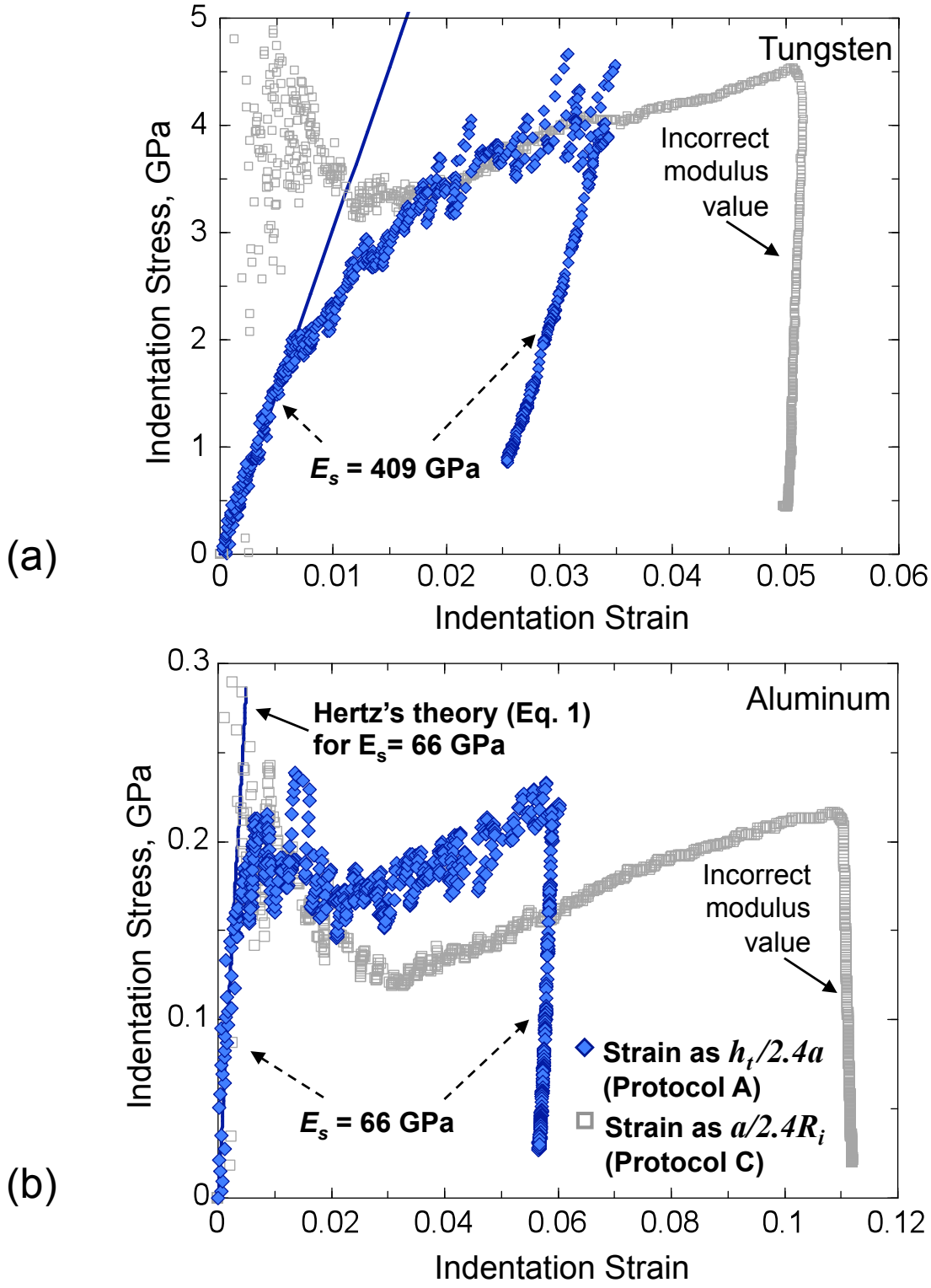

Figure 6. A comparison of the extracted indentation stress-strain curves for **(a)** tungsten and **(b)** aluminum, using the two different definitions of indentation strain. The definition of the indentation strain (= h_t /2.4*a,* Protocol A in Fig. 4) produces significantly better indentation stress-strain curves with correct values of indentation modulus during both loading and unloading.

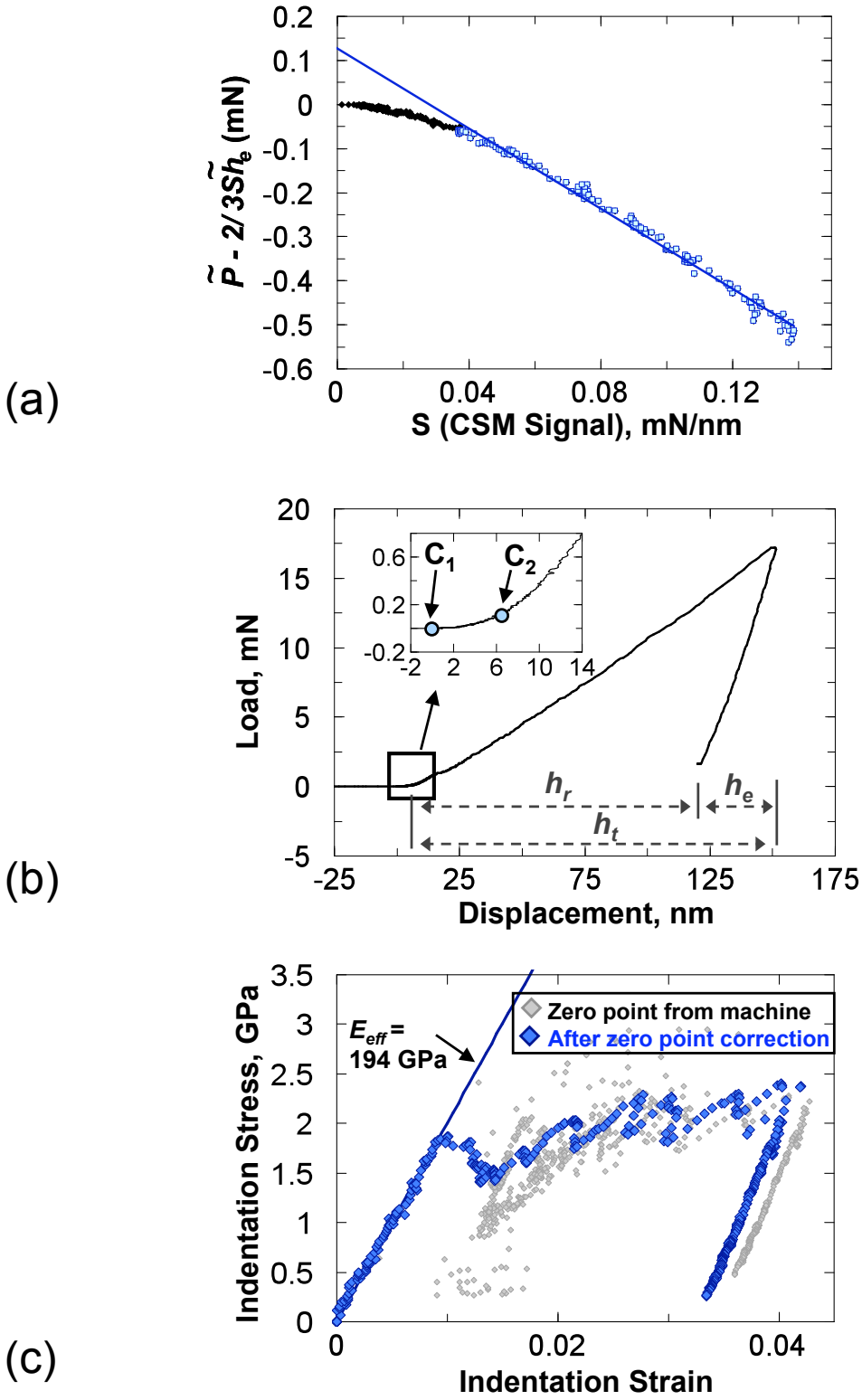

Figure 7. (a) The identification of the effective zero-point in the dataset measured on a vibro-polished Fe-3%Si steel sample indented with a 13.5 μm radius spherical indenter [12]. The measured **(b)** load-displacement curve and the extracted **(c)** indentation stress-strain curves for Fe-3%Si steel using two different estimates of the zero-point. The inset in (b) shows the two different estimates of the zero-point: C_1 - zero point given by the machine and C_2 - effective zero point determined using [12].

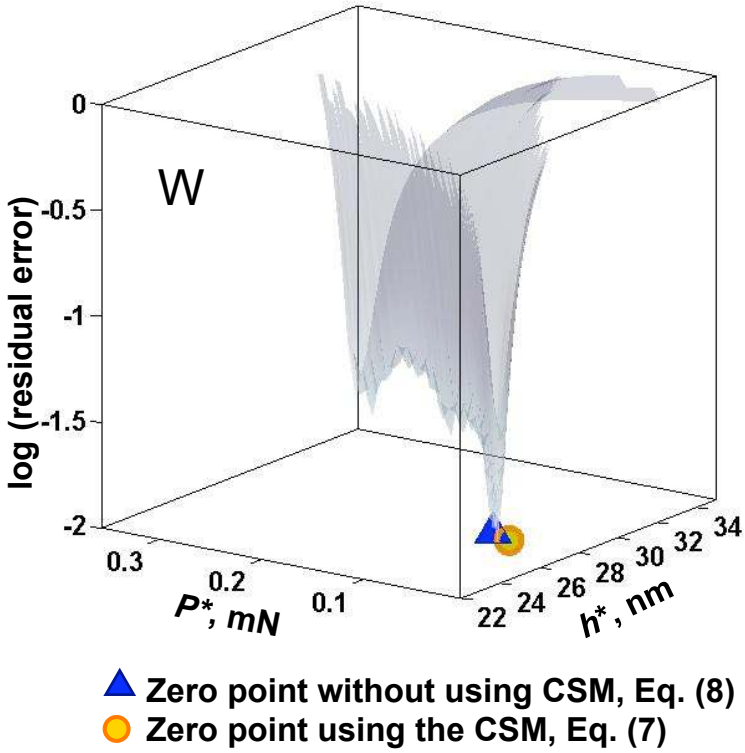

Figure 8. Comparison between the effective zero-points identified by the CSM technique (Eq. 7) and the non-CSM technique (Eq. 8) for tungsten using a 1.4 μm spherical indenter. The residual error is obtained from regression analyses as measure of the degree of fit to Eq. 8.

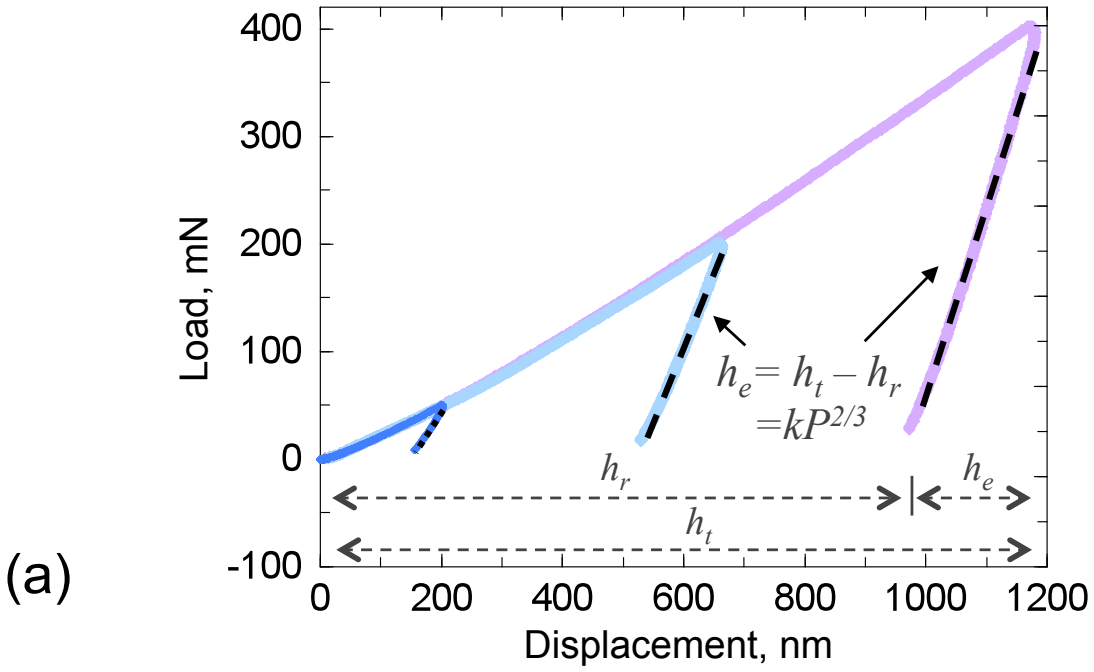

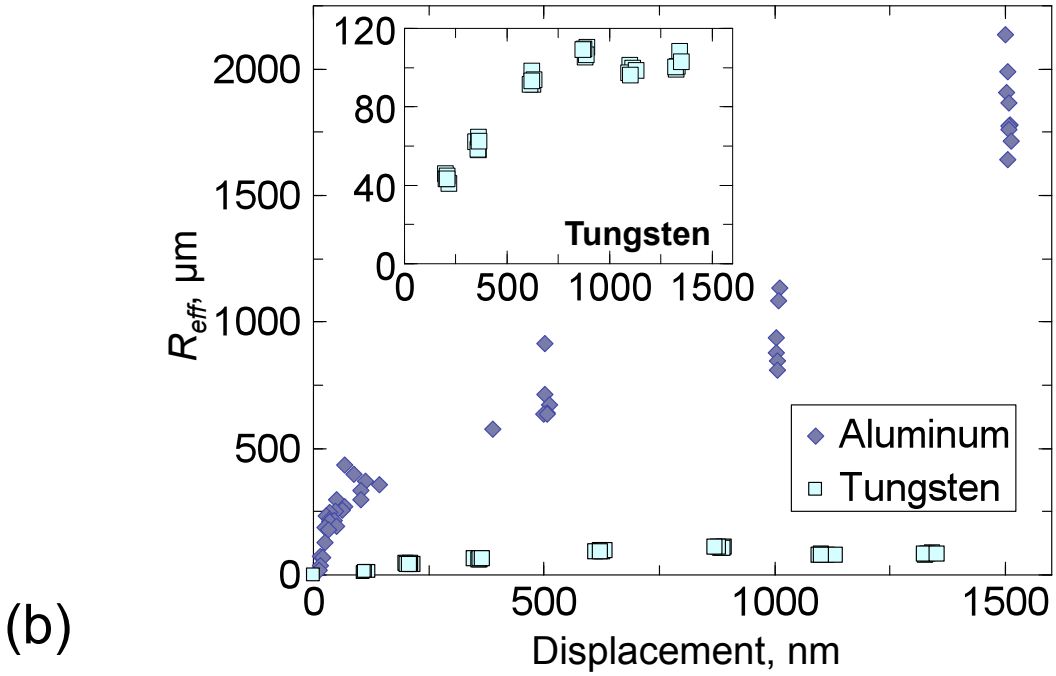

Figure 9.

(a) Schematic of the procedure involved in establishing the contact radius, a, at different load levels. The unloading segment at each of these load levels is fitted to Eq. 9 to estimate h_r and k. R_{eff} and a can then be calculated using Eqs. 8 and 10.

(b) Values of R_{eff} computed at different indentation depths which differ significantly between the softer aluminum and the harder tungsten sample. The values for R_{eff} are also significantly larger than R_i (= 20μm) for both samples. Inset: Expanded view for the tungsten sample.

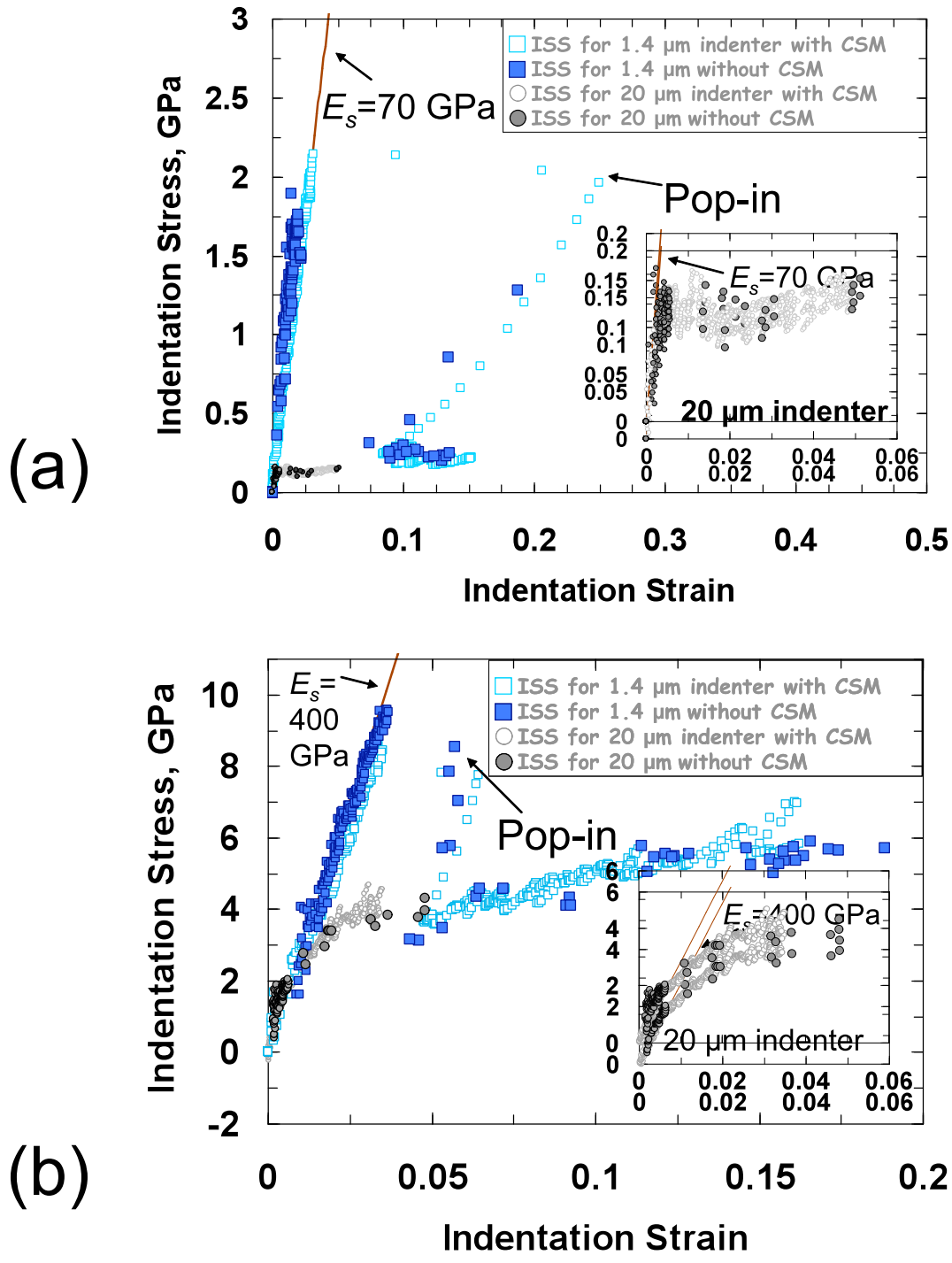

Figure 10. Comparison between the indentation stress-strain curves obtained using the CSM method (Section 5.1) and the non-CSM method (Section 5.2) on **(a)** aluminum and **(b)** tungsten samples with the 1.4 and 20 μm radii indenters. The insets show expanded views of the indentation stress-strain curves for the larger 20 μm indenter.

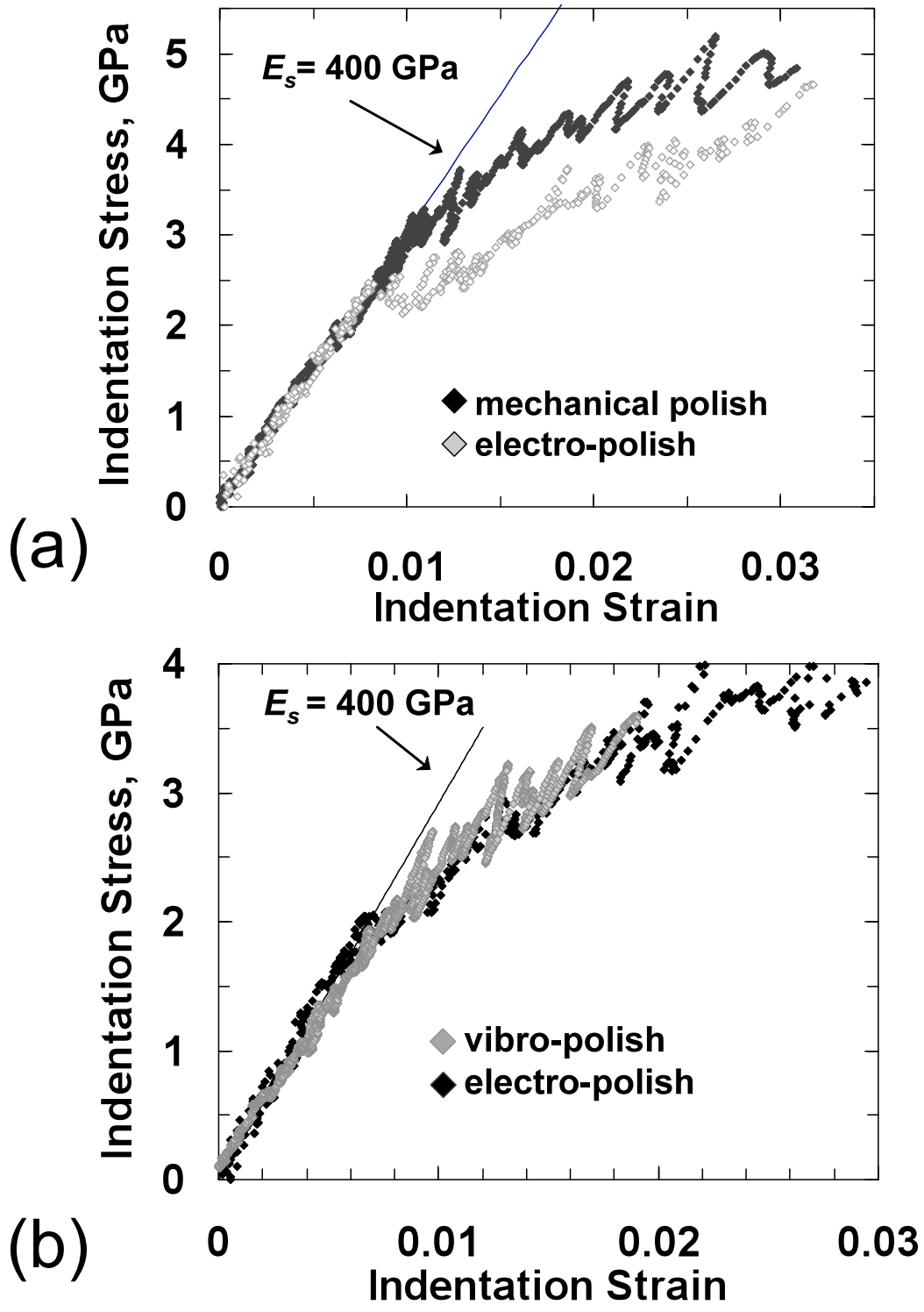

Figure 11. Comparison between the indentation stress-strain responses in **(a)** mechanically polished and electro-polished surfaces and **(b)** electro-polished and vibro-polished surfaces of annealed W. These tests were carried out using a 13.5 μm spherical indenter [65].

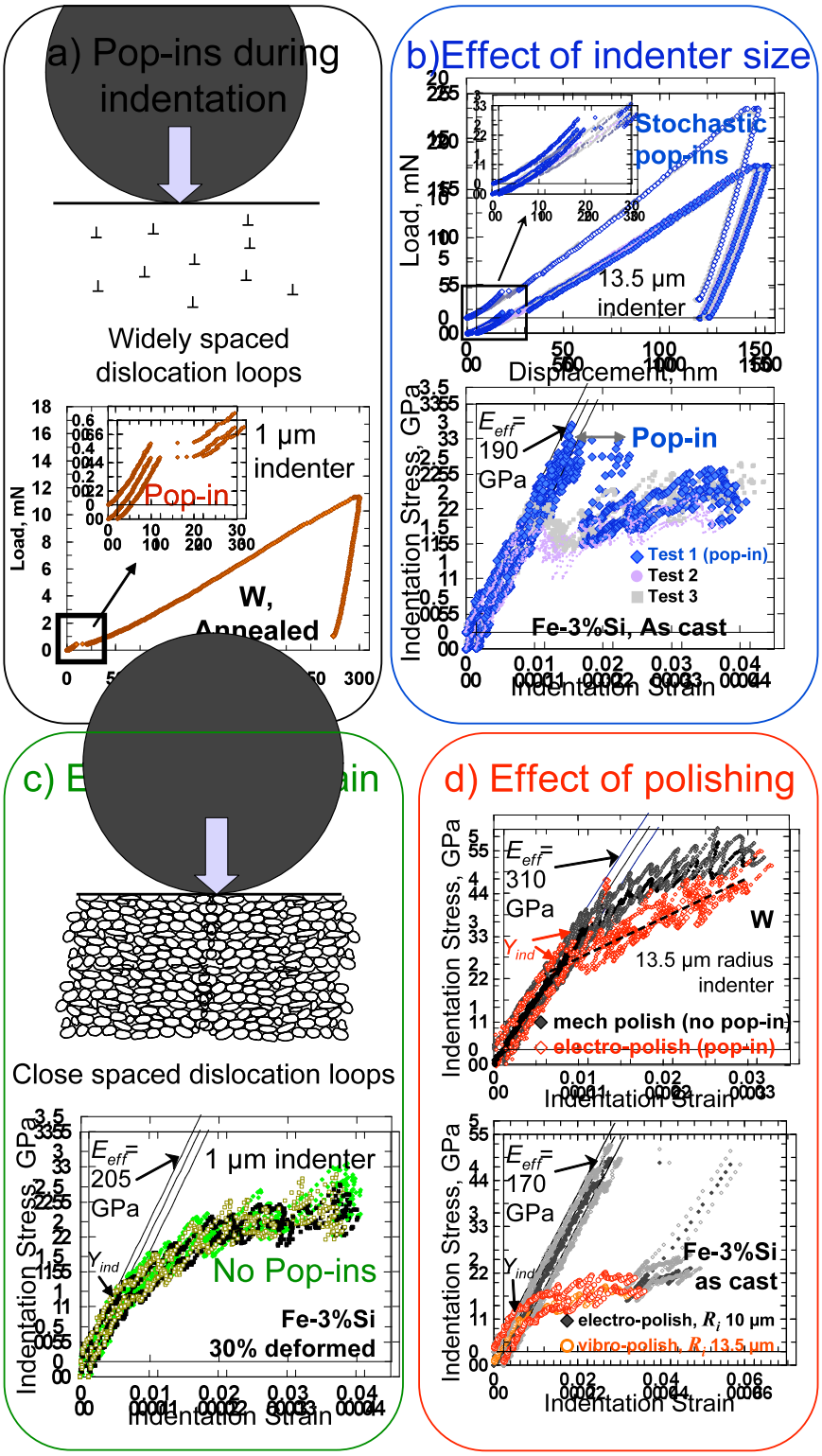

Figure 12. (a) Pop-ins in nanoindentation are generally revealed as sudden excursions in depth and strain (in a load controlled experiment) and occur most readily in indentation experiments on annealed samples with very small indenter tip radii, such as during indentation on annealed W with a 1 μm radius indenter [65]. **(b)** Their occurrence is more stochastic when using a larger indenter (such as during indentation on as-cast Fe-3%Si with a 13.5 μm radius indenter [65]) and **(c)** pop-ins are almost always absent in tests on cold-worked samples with high dislocation densities. Thus tests on 30% deformed Fe-3%Si steel do not show any pop-in even with a small sized indenter of 1 μm radius [65]. **(d)** Rough mechanical polishing can cause the near-surface dislocation density to increase, thus reducing pop-ins but artificially increasing the yield stress (Y_{ind}) in annealed W [65]. Vibro-polished samples show the ideal combination for measuring Y_{ind}: suppressing pop-ins in as-cast Fe-3%Si but not adversely affecting the Y_{ind} value [64].

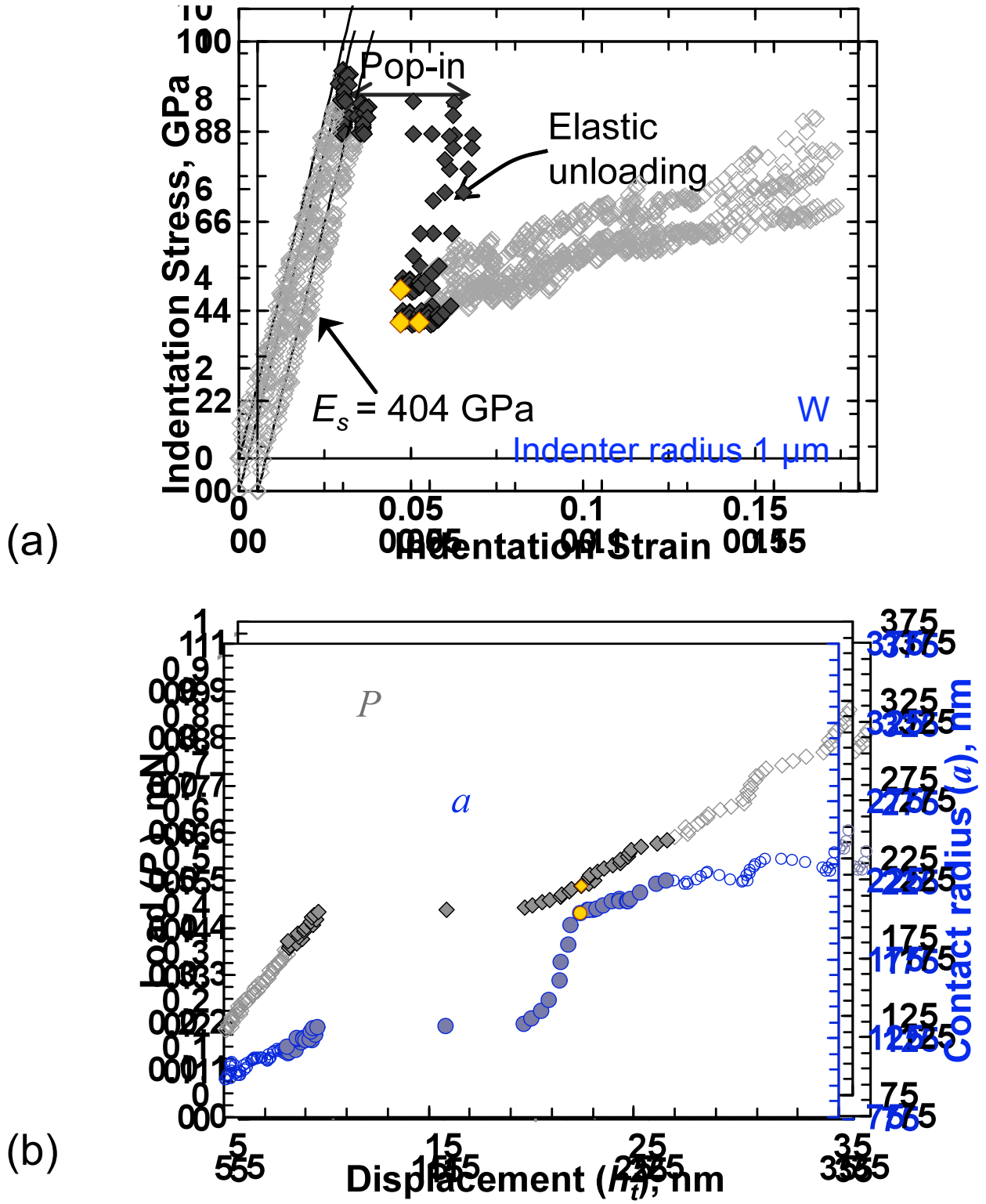

Figure 13. (a) Indentation stress-strain response of a pop-in event in an electropolished tungsten sample using a spherical indenter of 1 μm radius. The pop-in is manifested as a strain burst at constant stress, which is immediately followed by an unloading segment after the pop-in. **(b)** Corresponding measurements of the indentation load, displacement and contact radius (CSM signal) show that the contact radius remains constant during the pop-in but increases rapidly immediately afterwards. Note that the filled-in symbols correspond exactly between (a) and (b), i.e., the same range of data is shown by the filled-in symbols in the two figures. Note also the data point marked in gold color, which signifies the end of the regime of rapid increase in the contact radius in (b), and its corresponding location in the indentation stress-strain curve (a).

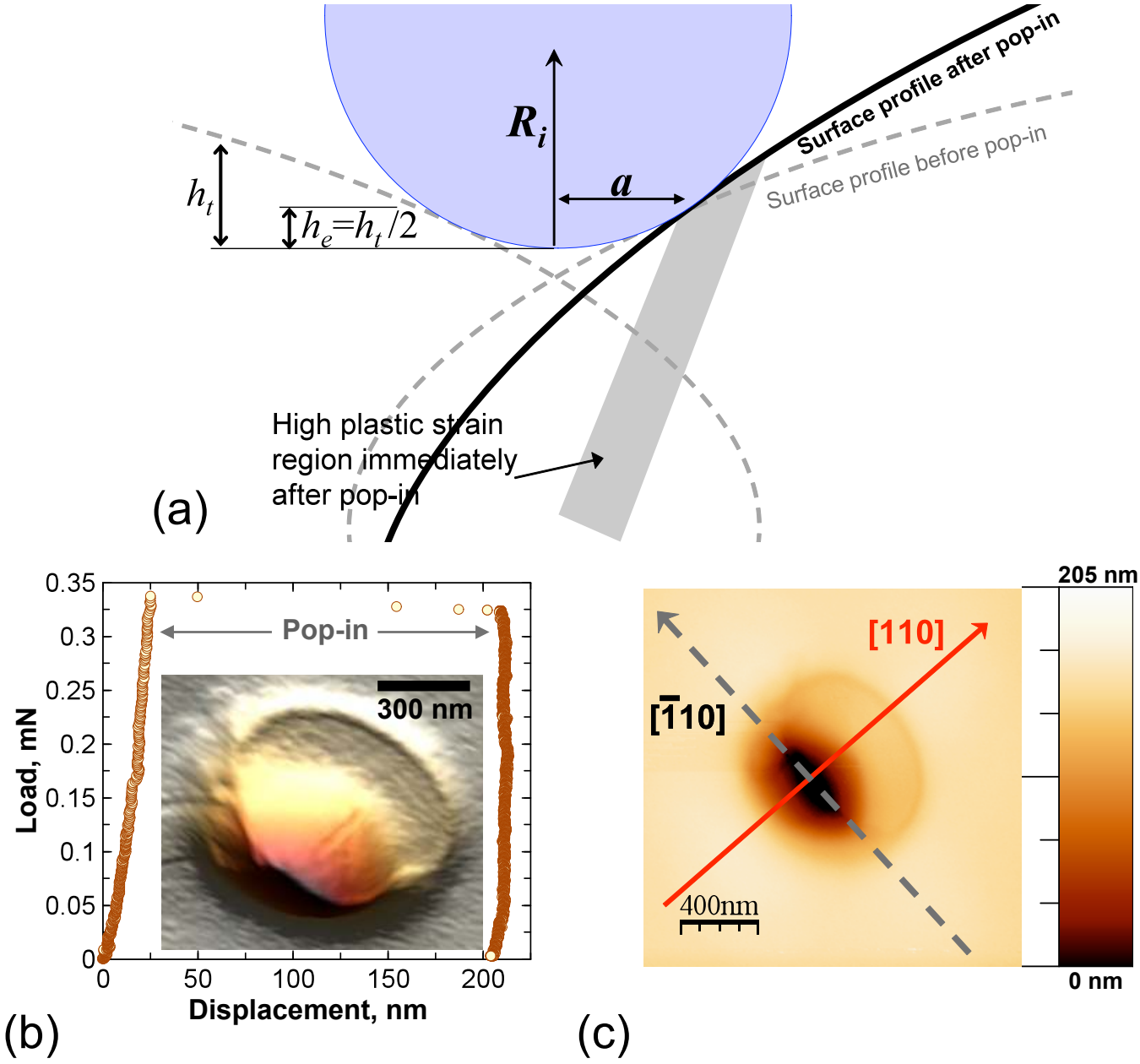

Figure 14. (a) Schematic of the sequence of events immediately following a pop-in in spherical nanoindentation. Before pop-in (the curve in gray) both the indenter and the sample surface are highly conforming up to a contact radius of a. Upon pop-in, there is a sudden increase in the indentation depth, but no immediate increase in a. Rather dislocations traveling (in bursts) along specific crystallographic planes get released along the free surface adjacent to the indenter. This brings the sample surface in closer proximity to the indenter. Thus any further loading causes a large increase in a.

(b) Load-displacement response on a near-(001) aluminum surface using a 1 μm indenter showing a test stopped after a single large pop-in event. **(b inset)** 3D and **(c)** surface profiles of the above indent measured using a hybrid AFM-SEM system showing a large step formation along the [110] direction of the indent surface. Note the significant anisotropy of the residual indent imprint, no such pile-up is visible in the perpendicular $[\bar{1}10]$ direction [214].

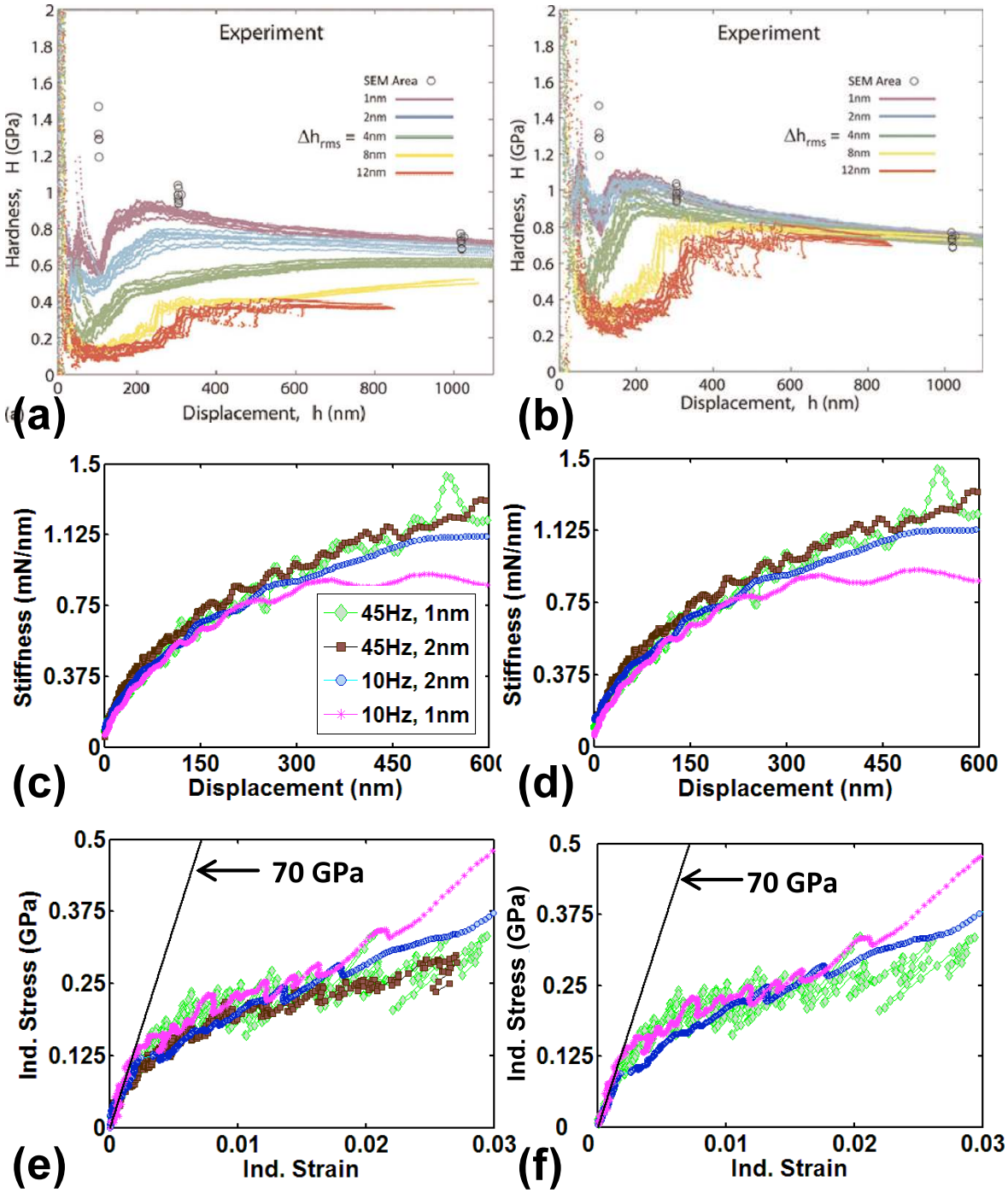

Figure 15. (a) Influence of the displacement oscillation on hardness, *H*, measured on Cu (100) using a Berkovich tip. **(b)** Hardnesses derived from corrected *P*–*h*–*S* data. Reprinted with permission from [91].

(c) Influence of CSM on the indentation stiffness-displacement response: Raw stiffness-displacement data corresponding to measurements conducted using a 100 μm spherical tip on 20% deformed ultra-high purity aluminum; **(d)** No noticeable changes are seen upon correcting the data using Eqs. 11-13 [99].

(e) Influence of CSM on the indentation stress-strain curves for tests on 20% deformed ultra-high purity aluminum using a 100 μm spherical tip; **(f)** the corresponding corrected data (using Eqs. 11-13) again shows no discernable change from the original. (Note that for tests with 45Hz – 2nm oscillations, most of the initial elastic segment is lost while correcting for the stiffness signal, and hence the indentation stress-strain curve could not be extracted) [99].

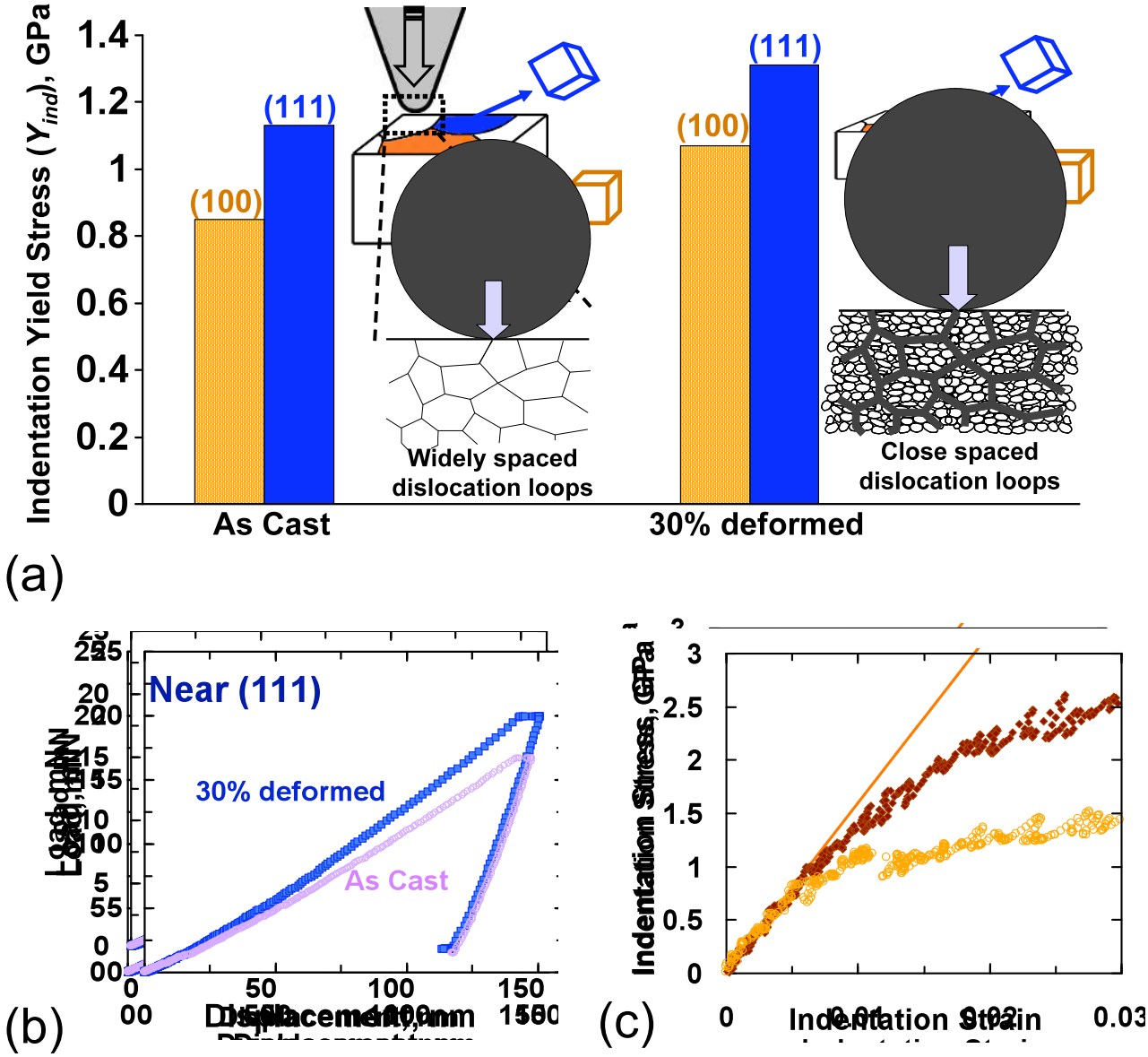

Figure 16. (a) Causes for the change in Y_{ind}. In an as-cast sample of Fe-3%Si steel, the dislocation content is fairly uniform across all the grains. Here Y_{ind} varies from one grain to another mainly due to the differences in the activities of the different slip systems in the different grains and their orientation with the indentation direction. When the metal is 30% deformed, its dislocation content increases and varies both within individual grains and between grains. The Y_{ind} in deformed samples therefore depends on both the grain orientation and the dislocation content at the indentation site.

(b) and **(c)** show the typical load-displacement and their corresponding indentation stress-strain responses respectively for spherical indentations performed on near (111) grains in as-cast and 30% deformed Fe-3%Si steel. The E_{eff}, Y_{ind} and the post-yield characteristics are much better discerned in (c). Only the loading sections are shown for the indentation stress-strain plots. A 13.5 μm radius spherical indenter was used for the tests.

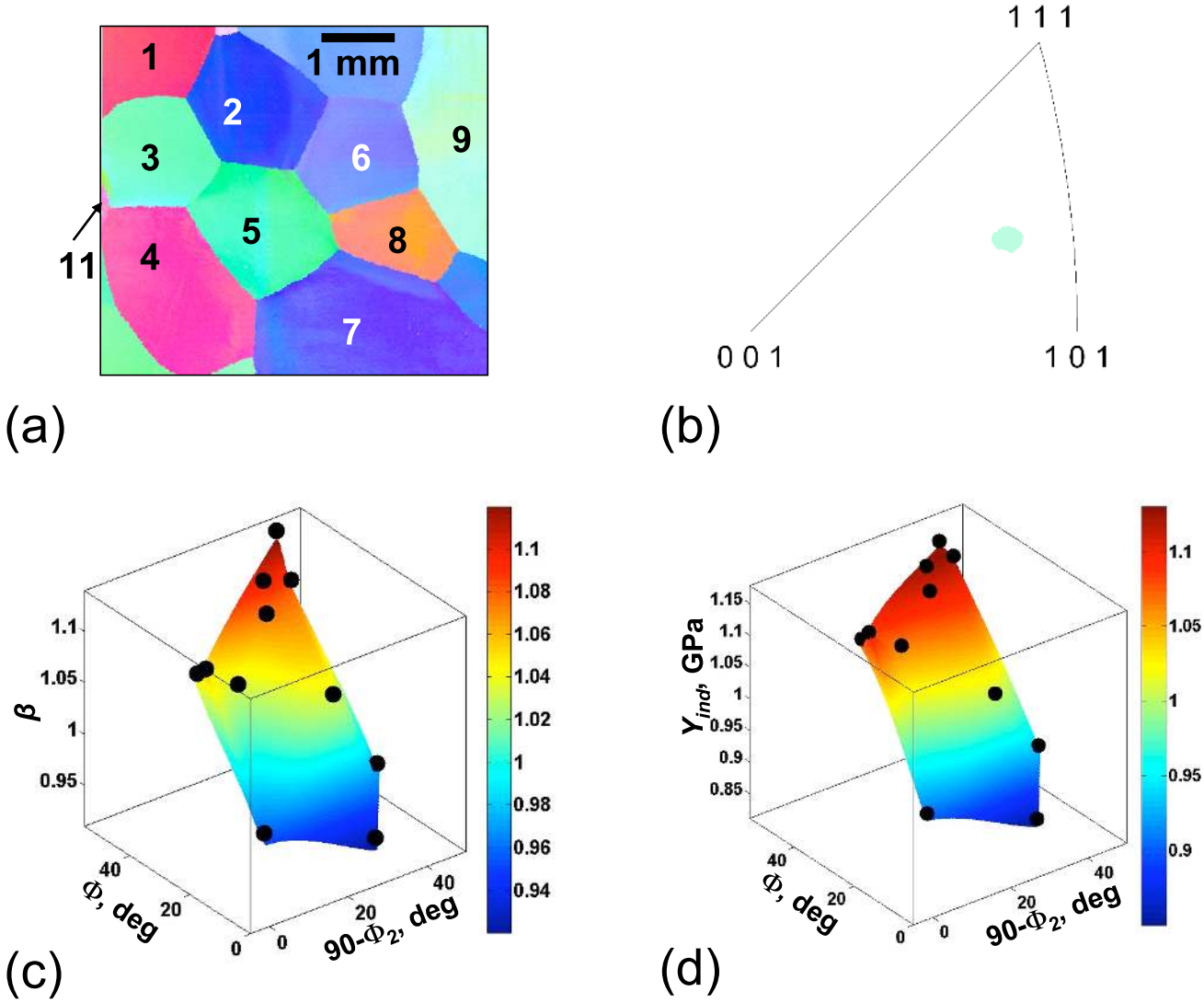

Figure 17. (a) OIM scan and **(b)** inverse pole figure map obtained on a sample of as-cast and polished Fe-3%Si showing a wide range of grain orientations. Surface contour plots for **(c)** β and **(d)** Y_{ind} . The full circles indicate values extracted directly from the measurements [66].

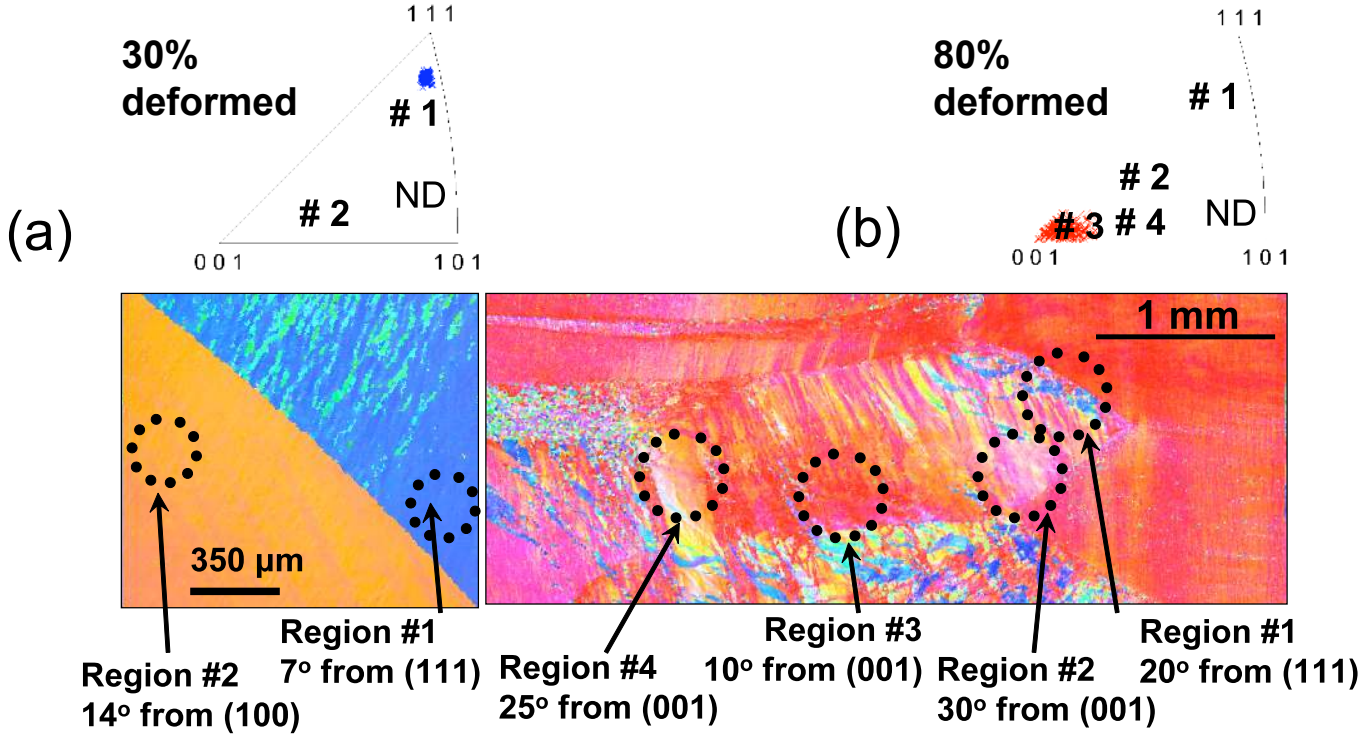

30% deformed Fe-3%Si							
Region #	**Orientation $(\varphi_1, \Phi, \varphi_2)$**	**Misorientation**	**E_{eff}, GPa**	**β**	**Measured Y_{ind} in the deformed condition, GPa**	**Estimated Y_{ind} in the annealed condition, GPa**	**% change in τ_{CRSS}**
1	148.3, 49.8, 50.7	7° from (111)	198.0±3.9	1.09	1.31±0.13	1.12	16.9%
2	294.2, 13.5, 83.8	14° from (001)	174.2±1.59	0.93	1.07±0.05	0.90	18.9%
80% deformed Fe-3%Si							
Region #	**Orientation $(\varphi_1, \Phi, \varphi_2)$**	**Misorientation**	**E_{eff}, GPa**	**β**	**Measured Y_{ind} in the deformed condition, GPa**	**Estimated Y_{ind} in the annealed condition, GPa**	**% change in τ_{CRSS}**
1	111.6, 49.4, 54.2	20° from (111)	198.1±1.26	1.09	1.69±0.06	1.12	50.9%
2	326.3, 23.2, 58	30° from (001)	191.1±1.42	1.04	1.46±0.07	1.00	46.0%
4	263, 16.2, 73.7	25° from (001)	185.9±0.75	1.00	1.37±0.07	0.92	48.9%
3	259, 3.9, 84.4	10° from (001)	174.3±0.19	0.93	1.27±0.08	0.85	49.4%

(c)

Figure 18. (a) and **(b)** show the inverse pole figure maps and the OIM scans for 30% and 80% deformed Fe-3%Si samples respectively. Indentations were performed in the regions marked by the dotted circles in each of these samples [66].

The table in **(c)** summarizes the values from indentations on the 30% and 80% deformed Fe-3%Si samples. The estimated Y_{ind} values in the annealed condition were calculated from the surface contour plot in Fig. 17d. The measured values of E_{eff} and Y_{ind} in the deformed condition were calculated from the indentation stress-strain curves, as shown in Fig. 16. The values for β were calculated from Eq. (14).

(a)

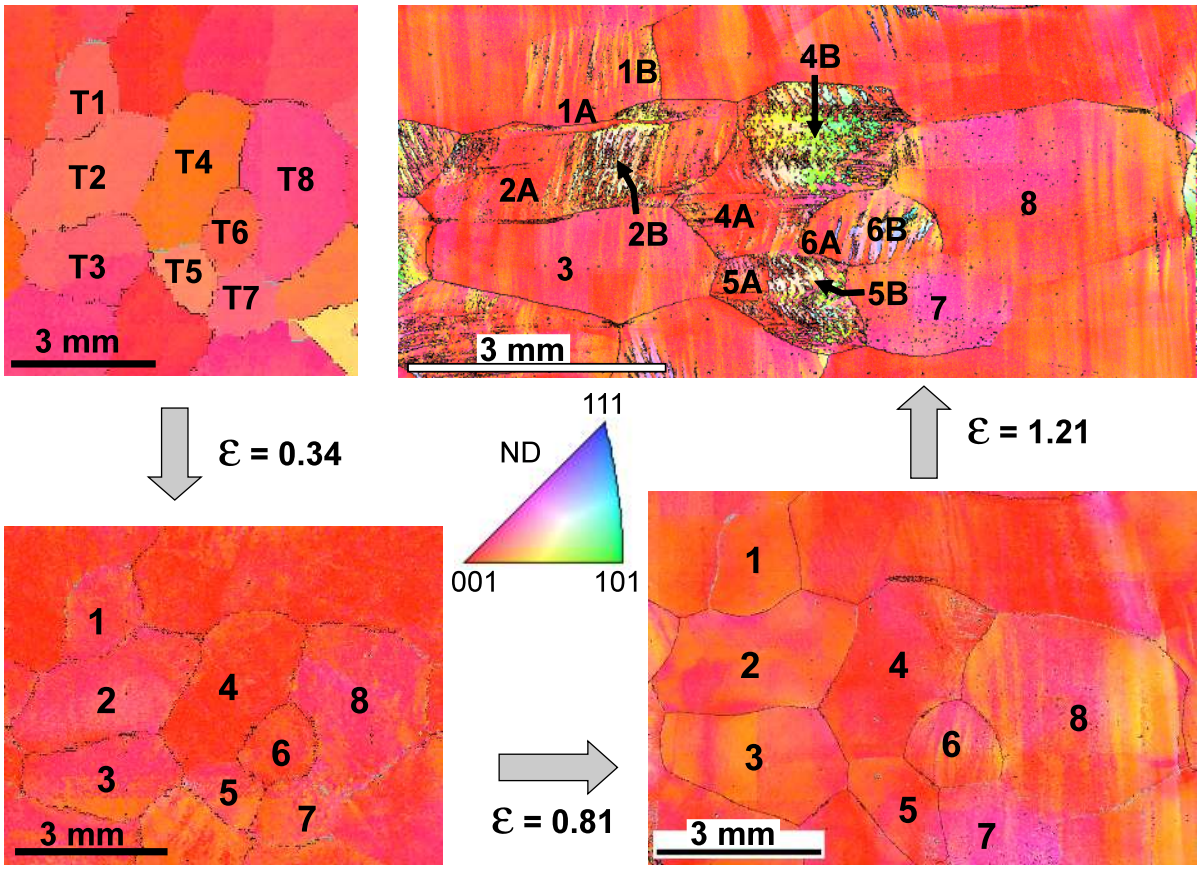

(b)

ε = 1.21				
Grain #	Orientation $(\varphi_1, \Phi, \varphi_2)$	Measured Y_{ind} in the deformed condition, GPa	Estimated Y_{ind} in the annealed condition, GPa	% change in τ_{CRSS}
1A	339, 5.6, 56.2	1.23 ± 0.06	0.85	44.4
1B	246, 15.2, 82	1.24 ± 0.09	0.91	36.6
2A	339, 2, 39.2	1.15 ± 0.07	0.85	35.2
2B	266, 25.9, 81	1.29 ± 0.14	0.99	30.7
3	342, 5.8, 56.5	1.14 ± 0.17	0.86	33.1
4A	324, 1.4, 30	1.11 ± 0.16	0.85	30.9
4B	272, 37.1, 84	1.24 ± 0.07	1.03	20.1
5A	99.4, 6.3, 90	1.07 ± 0.09	0.86	24.6
5B	288, 27.3, 70	1.58 ± 0.13	1	58.0
6A	331, 7.2, 66.5	0.96 ± 0.13	0.87	10.6
6B	122, 58, 71.6	1.95 ± 0.38	1.08	80.6
7	346, 12.2, 57	1.05 ± 0.09	0.89	18.3
8	167, 9.5, 53.1	1.16 ± 0.18	0.87	32.9

Figure 19. (a) OIM scans of the top surface showing the as-cast microstructure of the columnar Fe-3%Si sample, and microstructure after plane strain compression to true strains of 0.34, 0.81 and 1.21. The horizontal direction in these images is the rolling direction. **(b)** Extracted values of indentation yield strength and changes in critical resolved shear stress after the third deformation stage [113].

See also Fig 19c (next page)

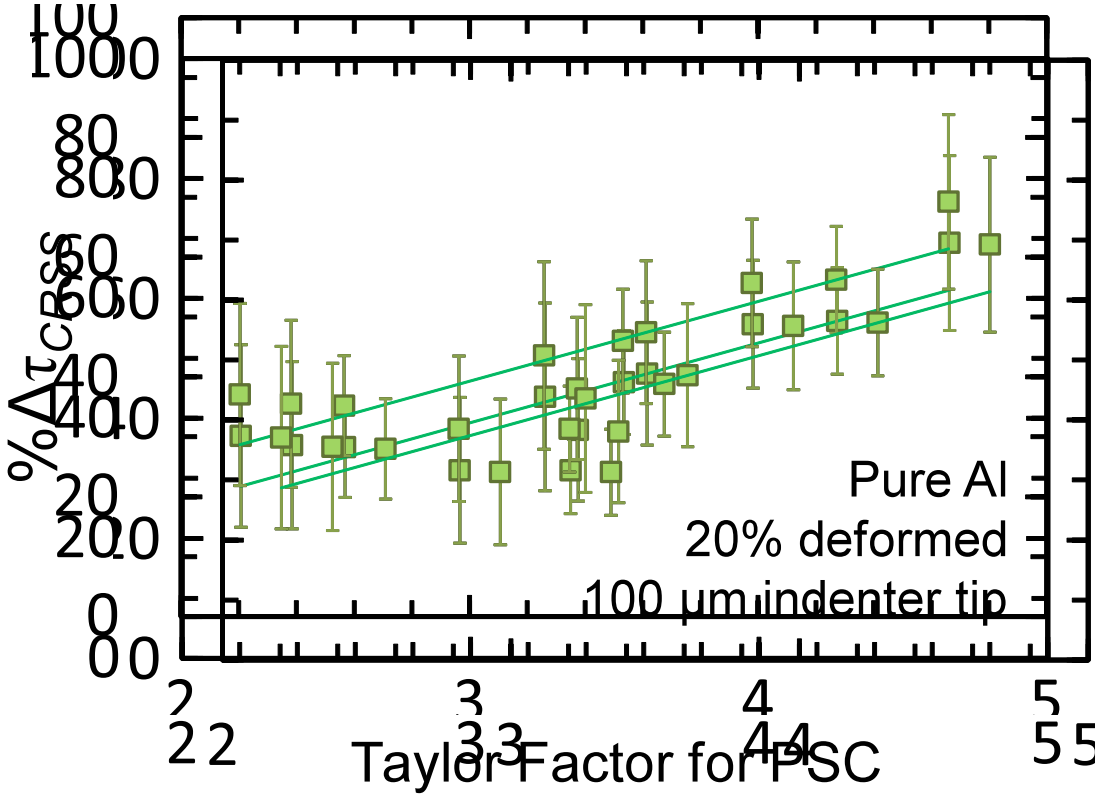

Figure 19. (c) For high purity polycrystalline Al deformed to 20% by plane strain compression (PSC), a positive correlation is observed between the Taylor factor of the individual grain orientations and the percentage increase in local slip resistance ($\%\Delta\tau_{CRSS}$) measured from the indentation yield strength values [108].

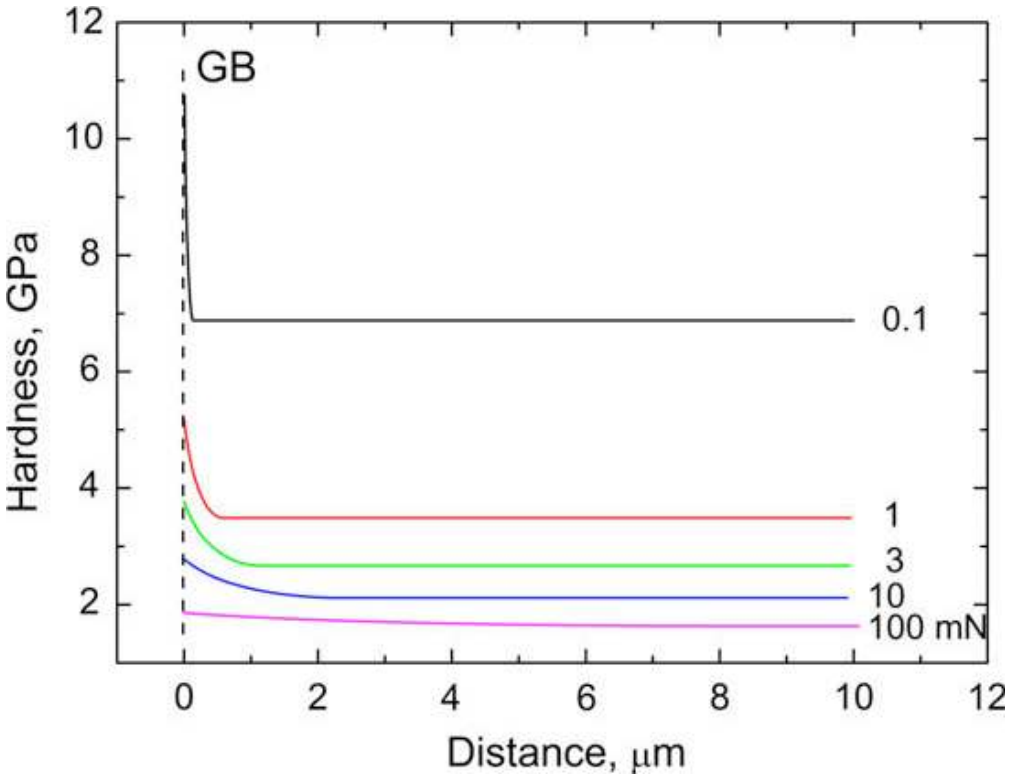

Figure 20. Indentation-induced deformation in Mo showing the dependence of hardness on the distance from grain boundary for different maximum indentation loads. At loads >10 mN the hardened zone near the grain boundary is masked by the additional local plastic deformation caused by indentation itself. Reprinted with permission from [85].

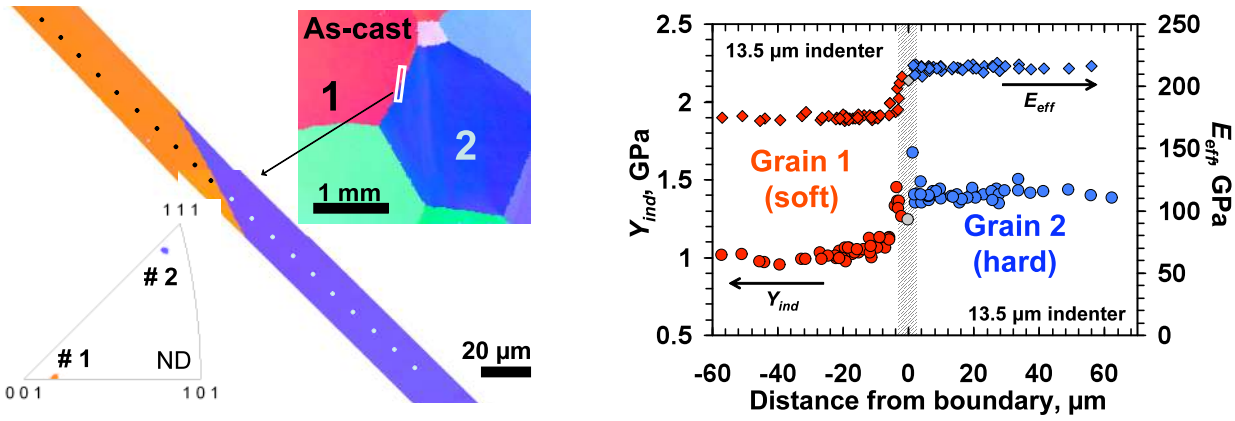

(a)

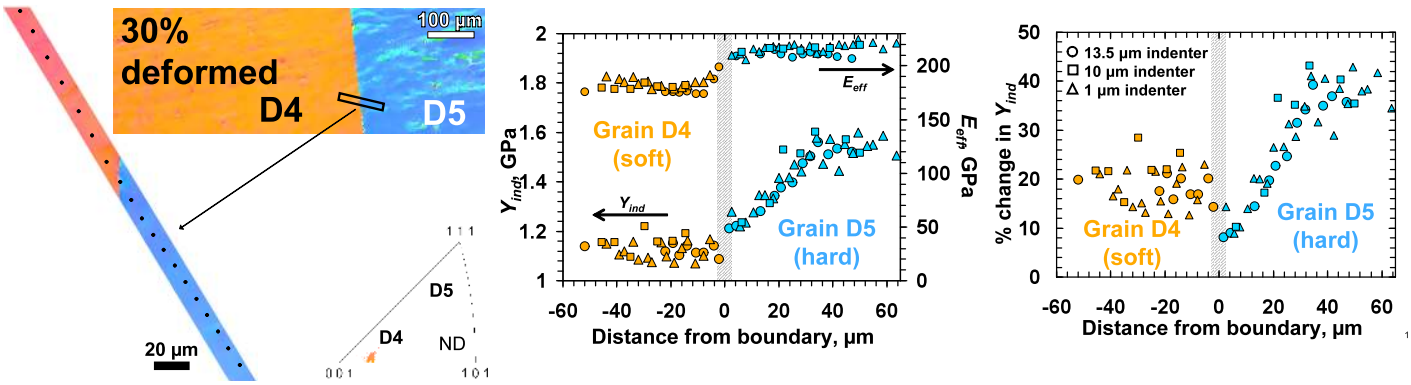

(b)

Figure 21. Measure of E_{eff} and Y_{ind} across a high angle grain boundary between **(a)** Grains 1 and 2 in as-cast Fe-3%Si steel and **(b)** Grains D4 and D5 in 30% deformed Fe-3%Si steel [64].

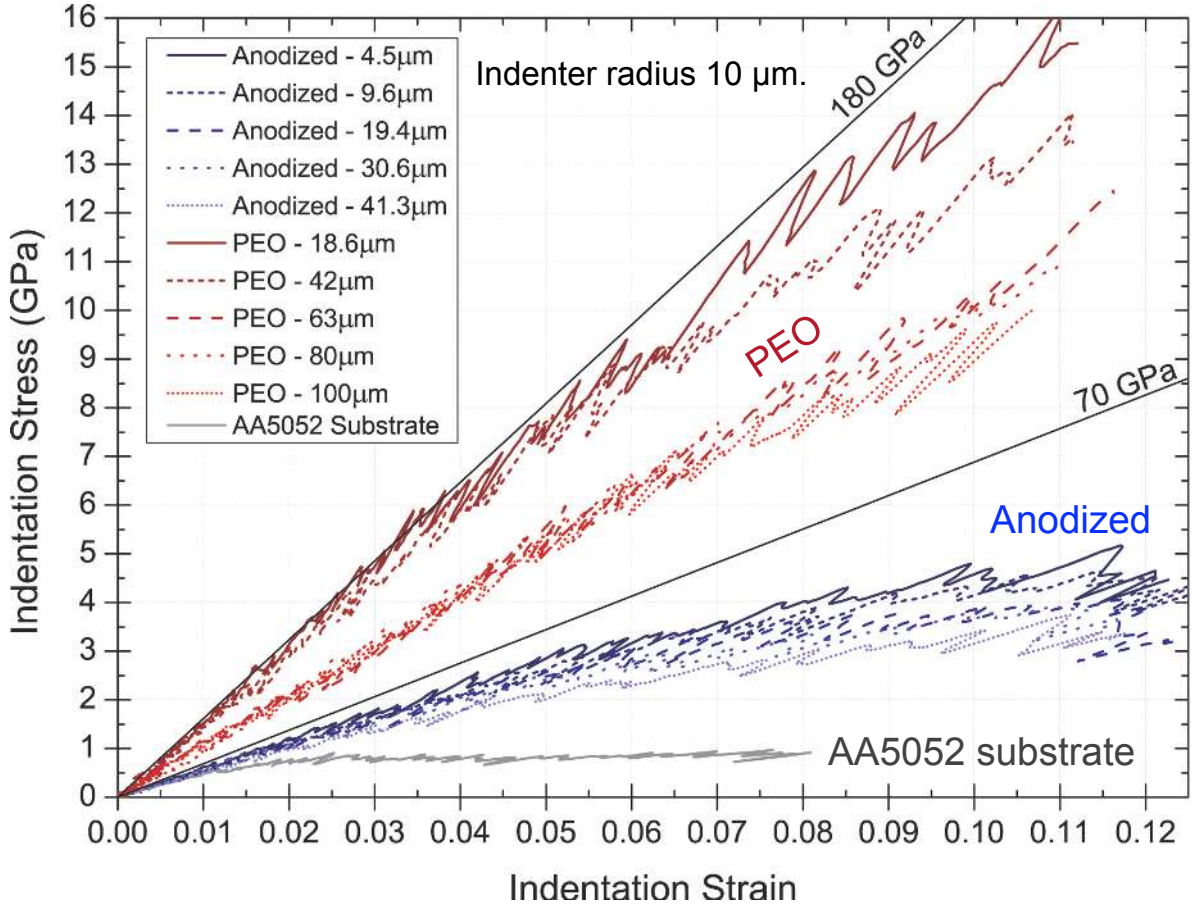

Figure 22. Comparing the indentation stress-strain responses across the cross-sections of two common electrolytic coating methods - hard anodizing and plasma electrolytic oxidation (PEO) – on a 5052 aluminum alloy at various distances from the substrate interface and within the aluminum substrate [127].

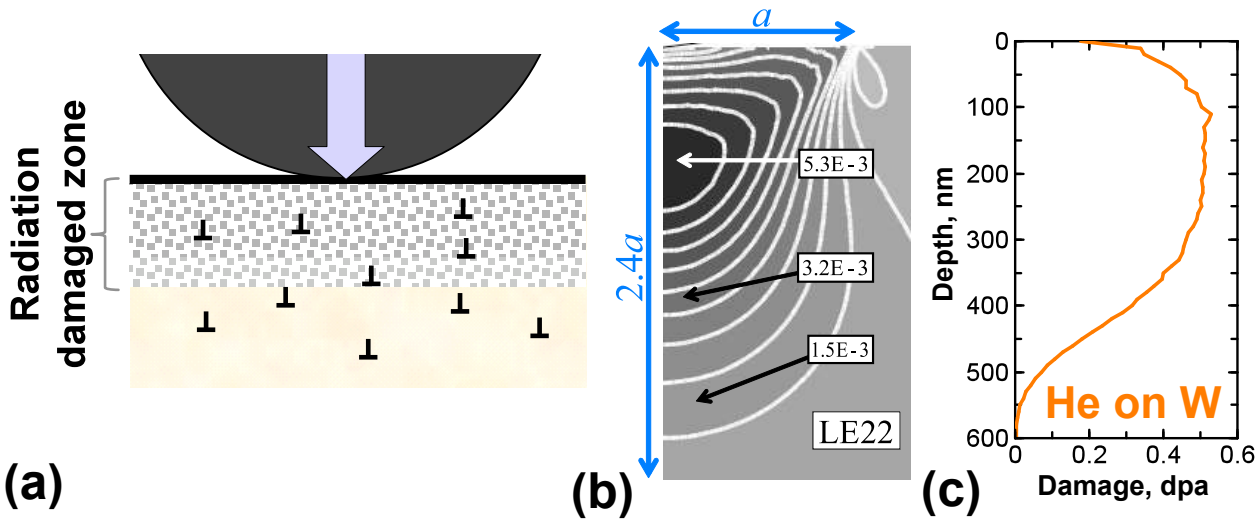

(d)

Indenter radius, R	Indentation depth, h_t	Contact radius, a	Indentation zone ~2.4a
1 µm	~10 nm	60 nm	144 nm
10 µm	~20 nm	250 nm	600 nm
100 µm	~40 nm	1,200 nm	2,880 nm
1000 µm *	>200 nm	12,800 nm	30,720nm

Figure 23. (a) Upon ion-irradiation, the metal surface is modified by a damaged layer, which causes a change in its mechanical response as compared to the bulk of the sample. **(b)** Map of the logarithmic strain component along the indentation direction (LE22) for a spherical indenter in the indentation zone (~2.4a, where a is the contact radius) close to the indentation yield [44]. Both the contact radius a, and hence the volume probed by indentation, can be controlled with a proper choice of indenter radii. This approach is thus ideally suited for measuring any mechanical changes in the material surface layers, such as probing the **(c)** damage caused by He irradiation on a tungsten sample. **(d)** Table showing indentation depth (h_t), contact radius (a) and indentation zone size (~2.4a) at yield for W using 4 different indenter radii.

* For the 1000 µm radius indenter, the response was all elastic up to h~200nm (instrument limit).

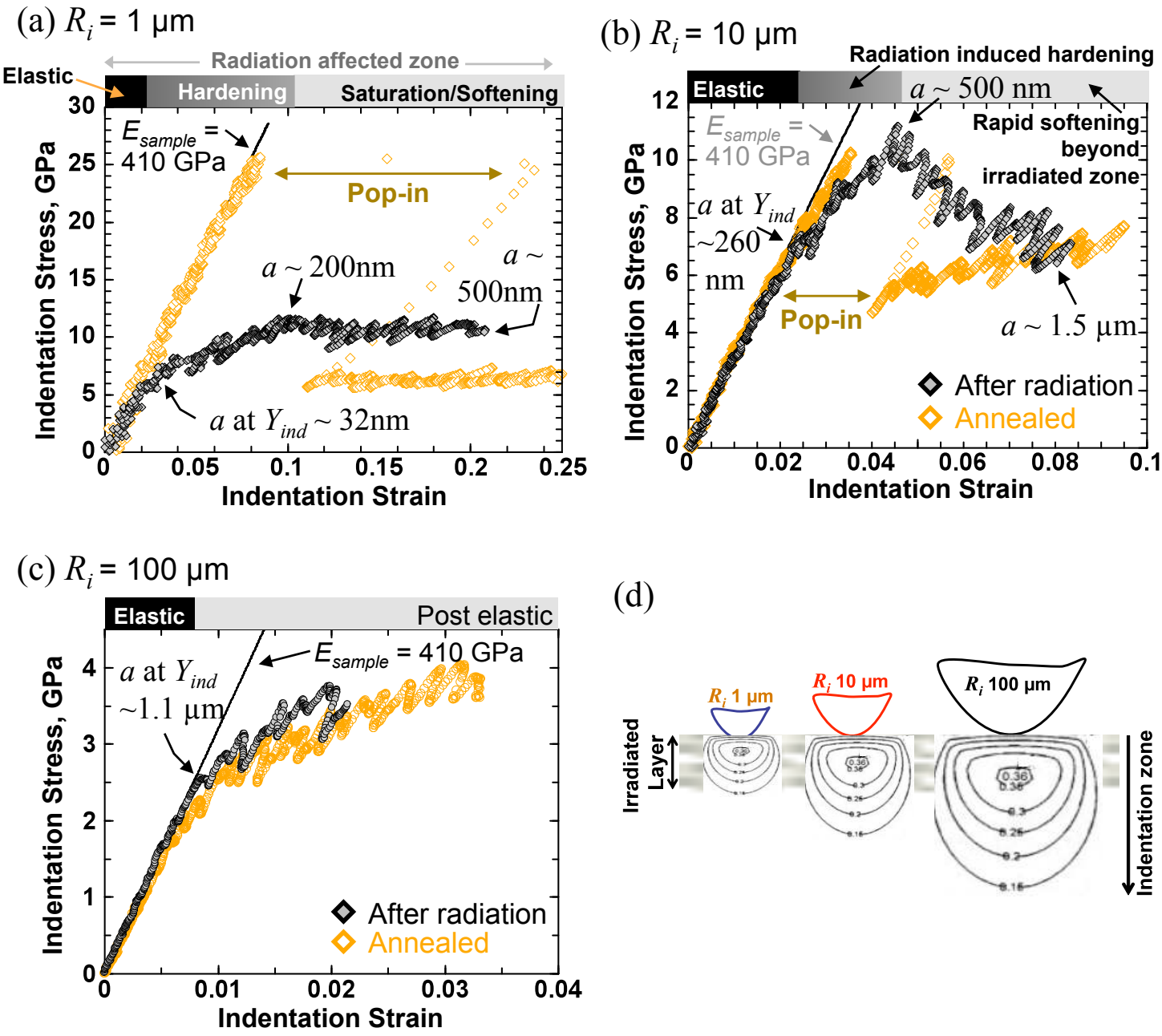

Figure 24. Comparing the indentation stress-strain responses between annealed (orange curve) and irradiated (black curve) W grains of near (001) orientation for three different indenter tip radii **(a)** 1 μm, **(b)** 10 μm and **(c)** 100 μm.
(d) Illustration showing how changes in the indenter size (and the corresponding indentation zone) can be used to systematically probe different length scale effects in radiation damaged samples.

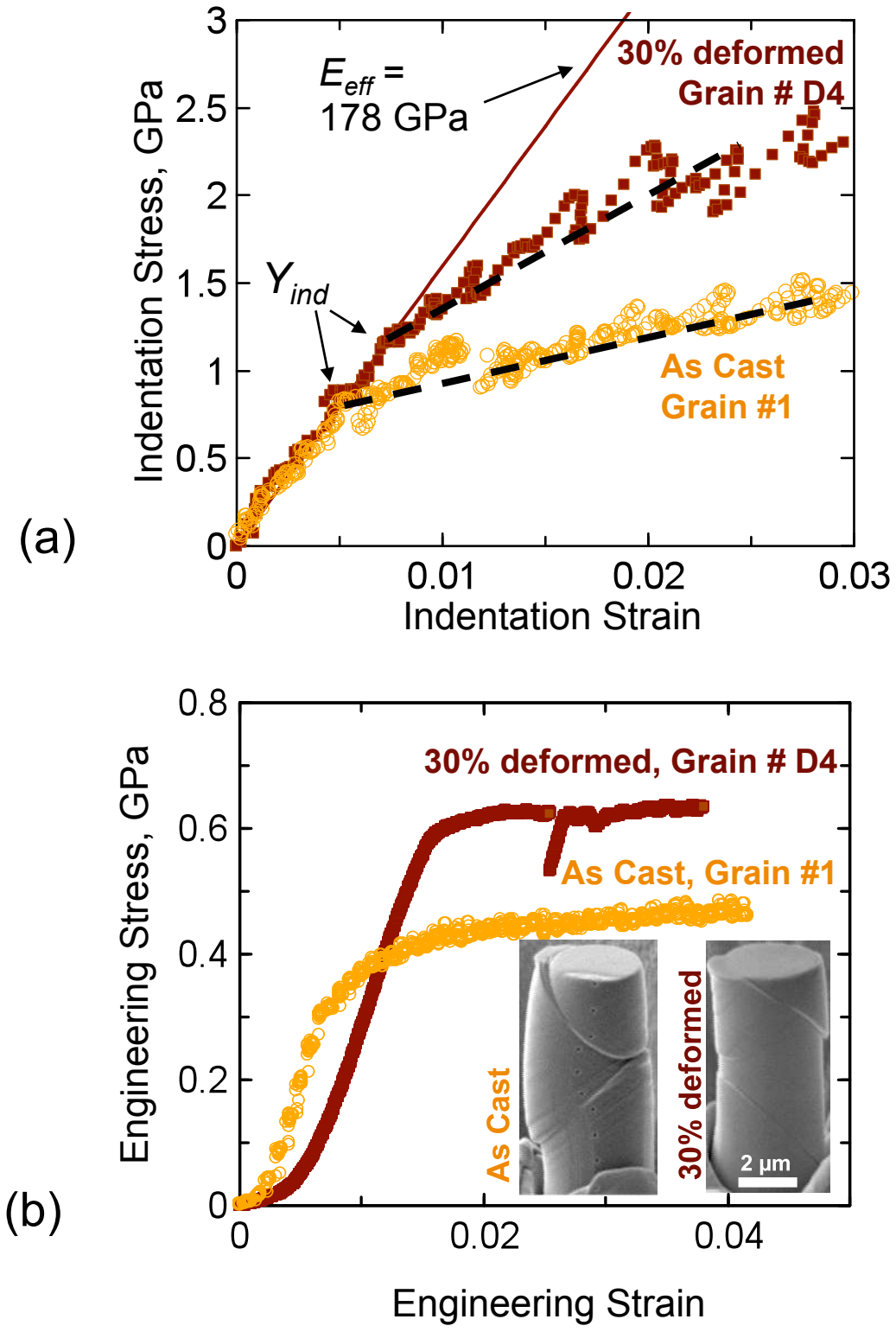

Figure 25. Comparison of (a) indentation vs. (b) compression stress-strain curves between as-cast and 30% deformed Fe-3%Si samples. Both grains #1 and #D4 have a near (100) orientation as shown in Fig. 21. SEM images of the pillars were taken at 70 deg tilt angle after a nominal strain of around 20%.

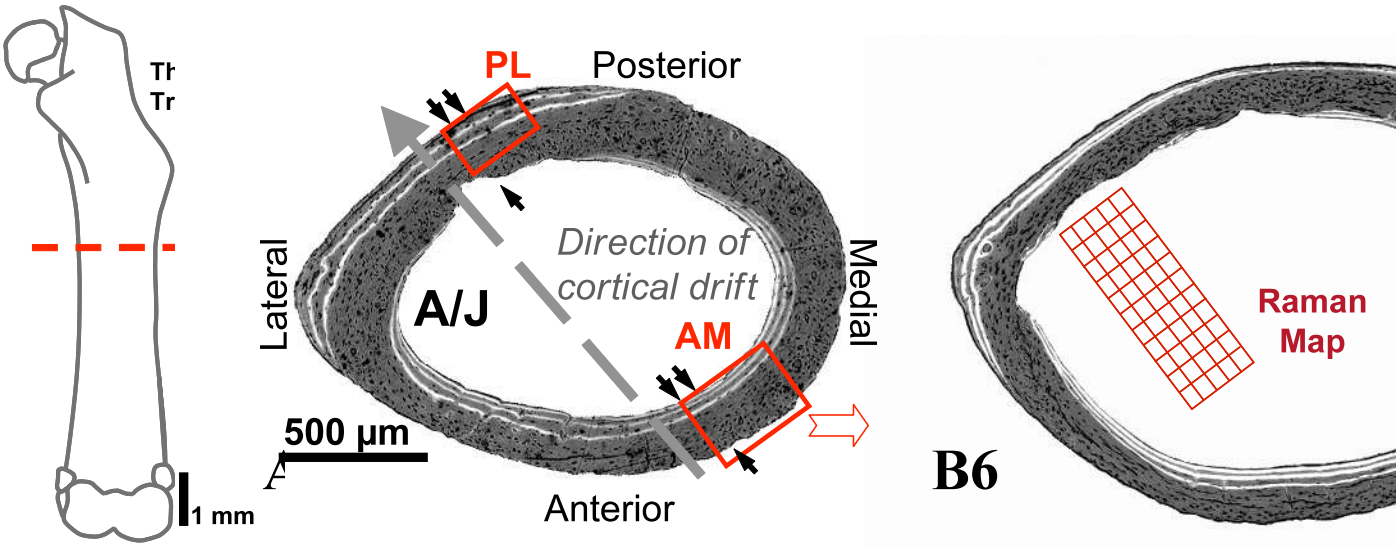

Figure 26. For indentation testing both the ‘dry’ and ‘wet’ mouse femora were sectioned transversely, distal to the third trochanter. During post-natal growth, bone is deposited (double arrows) and resorbed (single arrows) at different sites around these regions of the femoral cortex resulting in a net cortical drift (large arrow). Spherical nanoindents (shown as blue dots in the SEM image) at the antero-medial (AM) cortex thus probe newer bone closer to the endosteal edge (double arrows) while the bone is more mature away from this surface. Three rows of indentations were performed on each sample. For the ‘dry’ bone samples the region surrounding the indents was then mapped by Raman Spectroscopy (shown by the red grid around the indented region) [63].

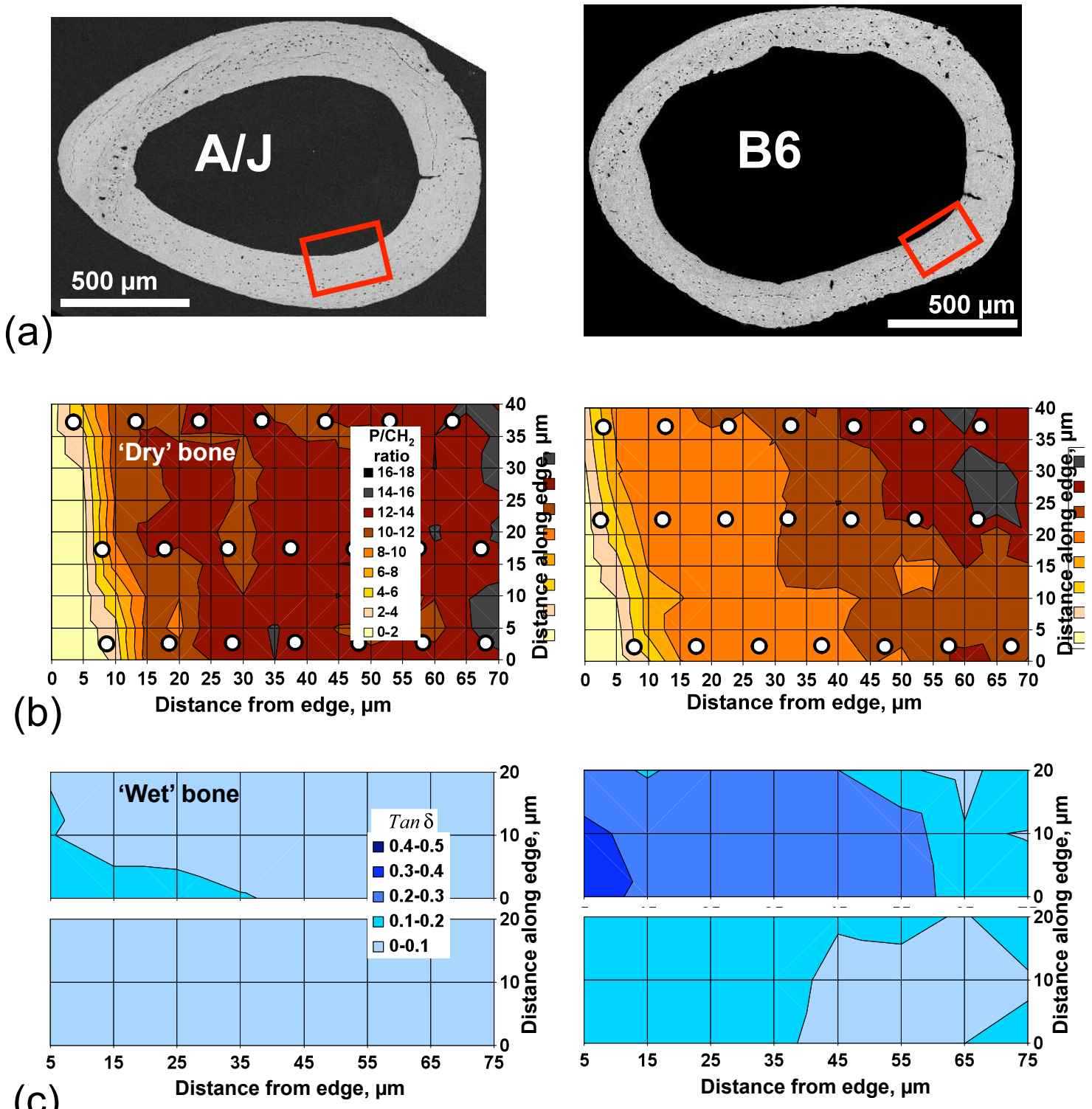

Figure 27. (a) Representative BSEM images of A/J and B6 mouse femora. **(b)** 'Dry' samples: representative 2D surface maps of the mineral-to-matrix ratios (defined as the phosphate to CH_2 wag peak intensity ratio from Raman spectroscopy measurements) in the 'dry' dehydrated/embedded bone samples across a 40 µm x 70 µm region close to the endosteal edge of the AM cortex. The white circles denote the approximate size and location of the indentation tests in relation to the Raman maps [63]. **(c)** 'Wet' samples: 2D surface maps of tan δ values at a representative mid-range frequency of 101 Hz across a 20 × 70 µm region close to the endosteal edge of the AM cortex in two A/J and B6 samples in the 'wet' hydrated condition [169].

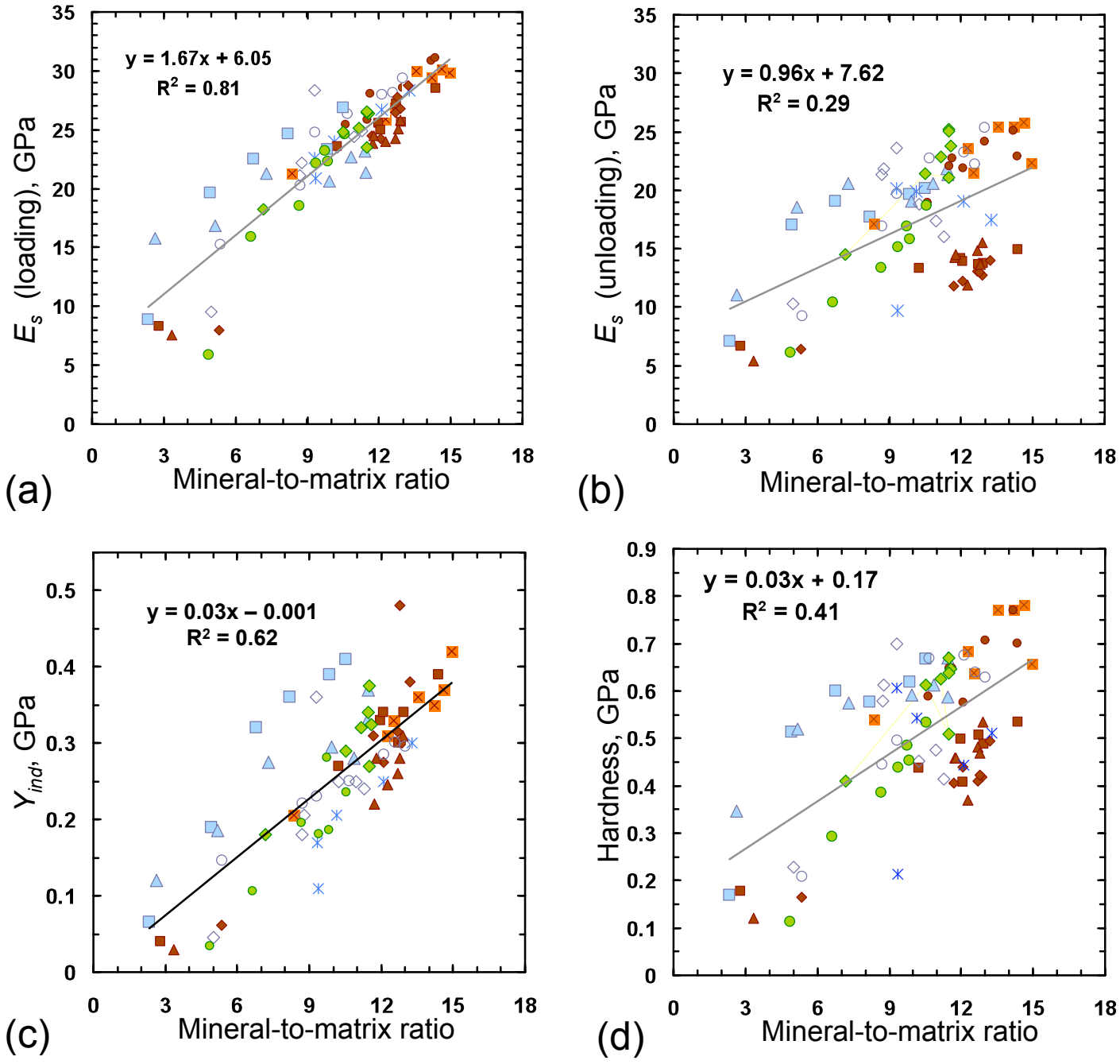

Figure 28. Scatter plots of **(a)** the Young's modulus E_s estimated from the initial loading segment of the indentation stress-strain curves, **(b)** E_s estimated from the unloading portion of the load-displacement data, **(c)** indentation yield strength (Y_{ind}) and **(d)** indentation hardness at max load, all as functions of the mineral-to-matrix ratio measured by Raman spectroscopy across two A/J and three B6 samples [63].

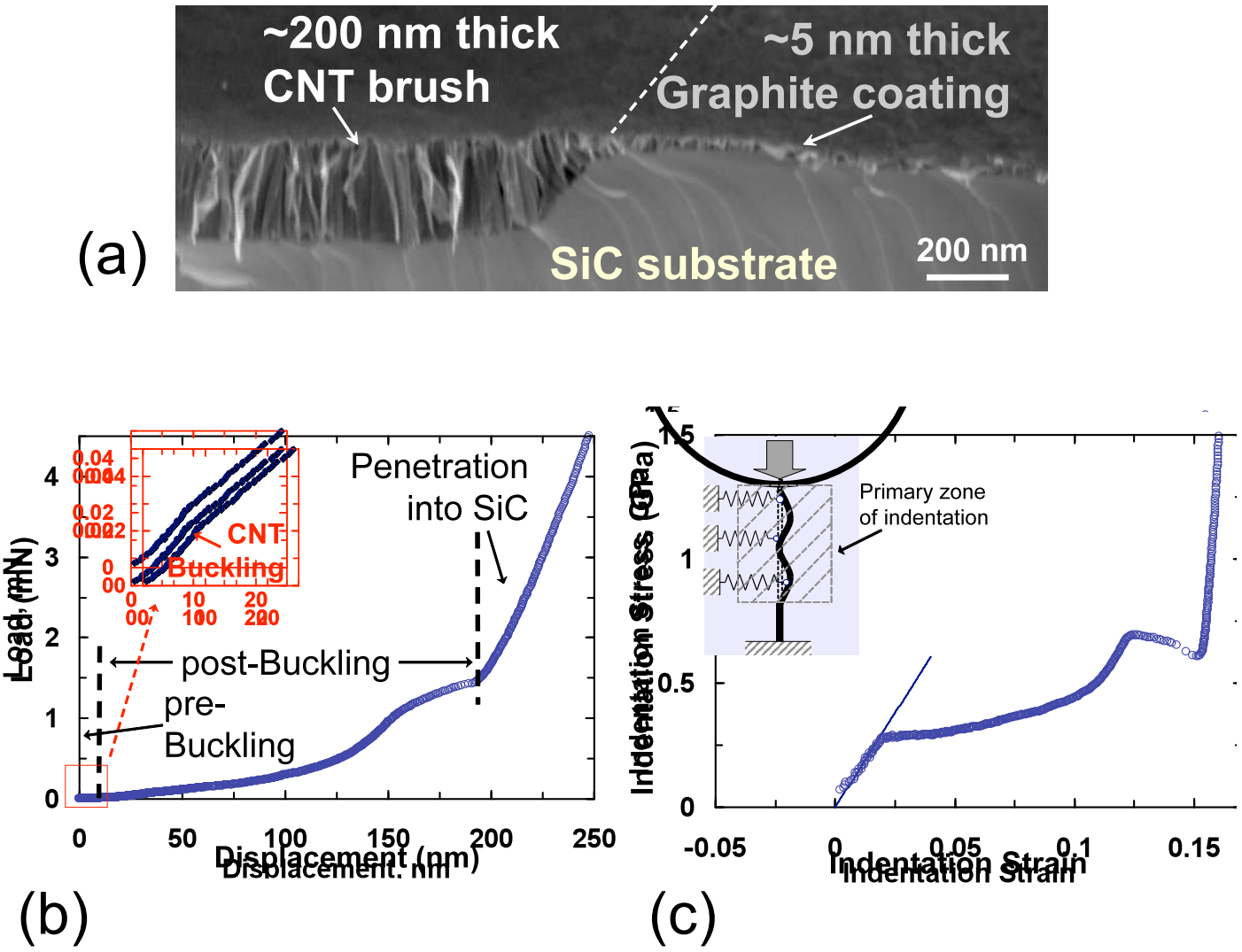

Figure 29. (a) SEM micrograph showing the VACNT brush – graphite interface [191]. **(b)** Indentation load-displacement and **(c)** indentation stress-strain response of a 1 μm spherical indenter on the ~200 nm thick CNT brush showing three distinct stages of VACNT indentation. **(c inset)** Schematic illustration of buckling of the CNTs in a dense CNT brush in the indentation zone.

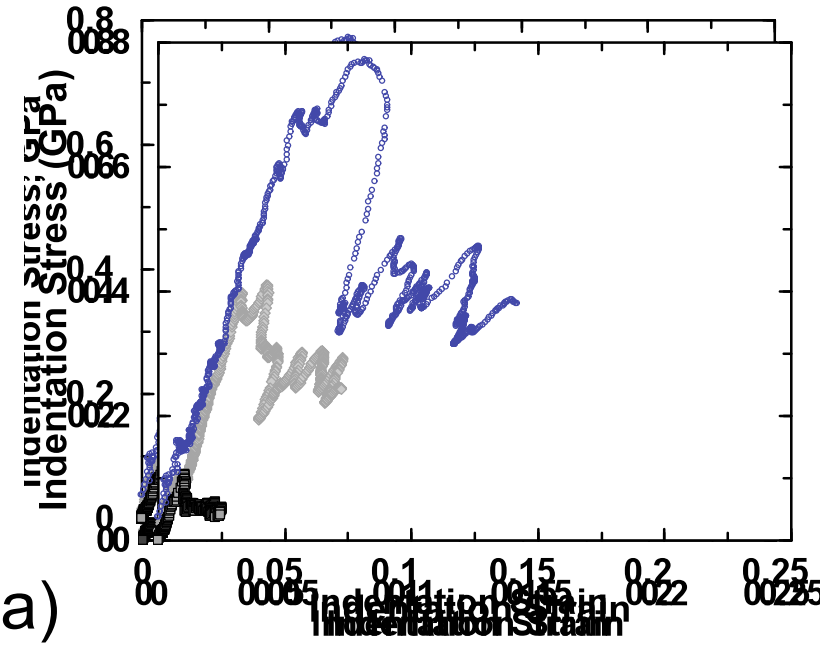

(a)

	1 µm radius indenter	5 µm radius indenter	13.5 µm radius indenter
Indentation buckling stress	0.59±0.41 GPa	0.40±0.11 GPa	0.09±0.02 GPa
Contact radius at buckling (*a*)	0.16 µm	0.36 µm	1.49 µm
Indentation zone size at buckling (≈ 2.4*a*)	0.39 µm	1.01 µm	3.58 µm

(b)

Figure 30. (a) Indentation stress-strain response on 1.3 µm thick VACNT brush as a function of indenter size (radius) showing an initial elastic behavior followed by the buckling instability.
The table in **(b)** shows summarized average and standard deviation (of ≥5 tests) values of indentation buckling stress, contact radius and indentation zone size at buckling for the 3 different indenters used [191].

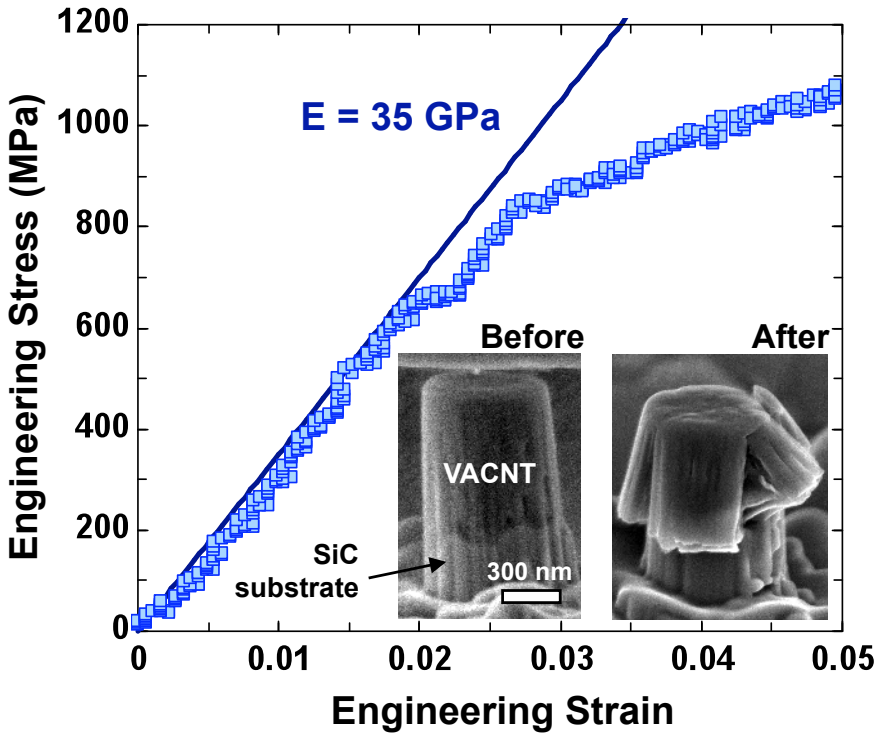

Figure 31. Uniaxial compression of a CDC-VACNT micro-pillar of diameter ~ 600 nm. Both the loading Young's modulus and buckling strength in compression show good agreement with the indentation results showed earlier. The inset images show the VACNT micro-pillar before and after compression.